The Astrophysical Journal, 881:153 (36pp), 2019 August 20 https://doi.org/10.3847/1538-4357/ab3049

Space Telescope and Optical Reverberation Mapping Project. VIII. Time Variability of Emission and Absorption in NGC 5548 Based on Modeling the Ultraviolet Spectrum

G. A. Kriss[1], G. De Rosa[1], J. Ely[1], B. M. Peterson[1,2,3], J. Kaastra[4,5], M. Mehdipour[4], G. J. Ferland[6], M. Dehghanian[6], S. Mathur[2,3], R. Edelson[7], K. T. Korista[8], N. Arav[9], A. J. Barth[10], M. C. Bentz[11], W. N. Brandt[12,13,14], D. M. Crenshaw[11], E. Dalla Bontà[15,16], K. D. Denney[2,3,17], C. Done[18], M. Eracleous[12,13], M. M. Fausnaugh[2,19], E. Gardner[20], M. R. Goad[21], C. J. Grier[2,22], Keith Horne[23], C. S. Kochanek[2,3], I. M. McHardy[24], H. Netzer[25], A. Pancoast[26,107], L. Pei[10], R. W. Pogge[2,3], D. Proga[27], C. Silva[4,28], N. Tejos[29], M. Vestergaard[22,30], S. M. Adams[2,31], M. D. Anderson[11], P. Arévalo[32], T G. Beatty[2,12,33], E. Behar[34], V. N. Bennert[35], S. Bianchi[36], A. Bigley[37], S. Bisogni[2,26,38], R. Boissay-Malaquin[39], G. A. Borman[40], M. C. Bottorff[41], A. A. Breeveld[42], M. Brotherton[43], J. E. Brown[44], J. S. Brown[2,45], E. M. Cackett[46], G. Canalizo[47], M. Cappi[48], M. T. Carini[49], K. I. Clubb[37], J. M. Comerford[50], C. T. Coker[2], E. M. Corsini[15,16], E. Costantini[4], S. Croft[37], K. V. Croxall[2,3,51], A. J. Deason[45,52], A. De Lorenzo-Cáceres[23,53], B. De Marco[54], M. Dietrich[51,108], L. Di Gesu[55], J. Ebrero[56], P. A. Evans[7], A. V. Filippenko[57,58,109], K. Flatland[59,60], E. L. Gates[61], N. Gehrels[62,110], S. Geier[53,63,64], J. M. Gelbord[65,66], L. Gonzalez[59], V. Gorjian[67], D. Grupe[68], A. Gupta[2], P. B. Hall[69], C. B. Henderson[2,67,111], S. Hicks[49], E. Holmbeck[70], T. W.-S. Holoien[2,3,71], T. A. Hutchison[41,72,73], M. Im[74], J. J. Jensen[75], C. A. Johnson[76], M. D. Joner[77], S. Kaspi[25,34], B. C. Kelly[78], P. L. Kelly[79,80,81], J. A. Kennea[12], M. Kim[82], S. C. Kim[83], S. Y. Kim[2,3], A. King[84], S. A. Klimanov[85], Y. Krongold[86], M. W. Lau[45,47], J. C. Lee[83], D. C. Leonard[59], Miao Li[87], P. Lira[88], C. Lochhaas[2], Zhiyuan Ma[41], F. MacInnis[41], M. A. Malkan[70], E. R. Manne-Nicholas[11], G. Matt[36], J. C. Mauerhan[37], R. McGurk[45,71], C. Montuori[89], L. Morelli[15,16,90], A. Mosquera[2,91], D. Mudd[2,10], F. Müller-Sánchez[50,92], S. V. Nazarov[40], R. P. Norris[11], J. A. Nousek[12], M. L. Nguyen[43], P. Ochner[15,16], D. N. Okhmat[40], S. Paltani[93], J. R. Parks[11], C. Pinto[94], A. Pizzella[15,16], R. Poleski[2], G. Ponti[95], J.-U. Pott[96], S. E. Rafter[34,97], H.-W. Rix[96], J. Runnoe[98], D. A. Saylor[11], J. S. Schimoia[2,99], K. Schnülle[96], B. Scott[47], S. G. Sergeev[40], B. J. Shappee[2,100], I. Shivvers[37], M. Siegel[101], G. V. Simonian[2], A. Siviero[15], A. Skielboe[75], G. Somers[2,102], M. Spencer[77], D. Starkey[23,103], D. J. Stevens[2,12,33], H.-I. Sung[83], J. Tayar[2,100,112], K. G. Teems[11], T. Treu[70,113], C. S. Turner[11], P. Uttley[28], J . Van Saders[2,100], L. Vican[70], C. Villforth[104], S. Villanueva Jr.[2], D. J. Walton[94], T. Waters[105], Y. Weiss[34], J.-H. Woo[74], H. Yan[44], H. Yuk[37], W. Zheng[37], W. Zhu[2], and Y. Zu[2,106]

[1] Space Telescope Science Institute, 3700 San Martin Drive, Baltimore, MD 21218, USA
[2] Department of Astronomy, The Ohio State University, 140 West 18th Avenue, Columbus, OH 43210, USA
[3] Center for Cosmology and AstroParticle Physics, The Ohio State University, 191 West Woodruff Avenue, Columbus, OH 43210, USA
[4] SRON Netherlands Institute for Space Research, Sorbonnelaan 2, 3584 CA Utrecht, The Netherlands
[5] Leiden Observatory, Leiden University, P.O. Box 9513, 2300 RA Leiden, The Netherlands
[6] Department of Physics and Astronomy, The University of Kentucky, Lexington, KY 40506, USA
[7] Department of Astronomy, University of Maryland, College Park, MD 20742, USA
[8] Department of Physics, Western Michigan University, 1120 Everett Tower, Kalamazoo, MI 49008, USA
[9] Department of Physics, Virginia Tech, Blacksburg, VA 24061, USA
[10] Department of Physics and Astronomy, 4129 Frederick Reines Hall, University of California, Irvine, CA 92697, USA
[11] Department of Physics and Astronomy, Georgia State University, 25 Park Place, Suite 605, Atlanta, GA 30303, USA
[12] Department of Astronomy and Astrophysics, Eberly College of Science, The Pennsylvania State University, 525 Davey Laboratory, University Park, PA 16802, USA
[13] Institute for Gravitation and the Cosmos, The Pennsylvania State University, University Park, PA 16802, USA
[14] Department of Physics, 104 Davey Lab, The Pennsylvania State University, University Park, PA 16802, USA
[15] Dipartimento di Fisica e Astronomia "G. Galilei," Università di Padova, Vicolo dell'Osservatorio 3, I-35122 Padova, Italy
[16] INAF–Osservatorio Astronomico di Padova, Vicolo dell'Osservatorio 5 I-35122, Padova, Italy
[17] Illumination Works, LLC, 5650 Blazer Parkway, Dublin, OH 43017, USA
[18] Centre for Extragalactic Astronomy, Department of Physics, University of Durham, South Road, Durham DH1 3LE, UK
[19] Department of Physics, Massachusetts Institute of Technology, 77 Massachusetts Avenue, Cambridge, MA 02139-4307, USA
[20] School of Biological Sciences, University of Reading, Whiteknights, Reading, RG6 6AS, UK
[21] Department of Physics and Astronomy, University of Leicester, Leicester, LE1 7RH, UK
[22] Steward Observatory, University of Arizona, 933 North Cherry Avenue, Tucson, AZ 85721, USA
[23] SUPA Physics and Astronomy, University of St. Andrews, Fife, KY16 9SS Scotland, UK
[24] University of Southampton, Highfield, Southampton, SO17 1BJ, UK
[25] School of Physics and Astronomy, Raymond and Beverly Sackler Faculty of Exact Sciences, Tel Aviv University, Tel Aviv 69978, Israel
[26] Harvard-Smithsonian Center for Astrophysics, 60 Garden Street, Cambridge, MA 02138, USA
[27] Department of Physics & Astronomy, University of Nevada, Las Vegas, 4505 South Maryland Parkway, Box 454002, Las Vegas, NV 89154-4002, USA
[28] Astronomical Institute "Anton Pannekoek," University of Amsterdam, Science Park 904, 1098 XH Amsterdam, The Netherlands
[29] Instituto de Física, Pontificia Universidad Católica de Valparaíso, Casilla 4059, Valparaíso, Chile
[30] DARK, Niels Bohr Institute, University of Copenhagen, Lyngbyvej 2, DK-2100 Copenhagen Ø, Denmark
[31] Cahill Center for Astrophysics, California Institute of Technology, Pasadena, CA 91125, USA
[32] Instituto de Física y Astronomía, Facultad de Ciencias, Universidad de Valparaíso, Gran Bretana N 1111, Playa Ancha, Valparaíso, Chile
[33] Center for Exoplanets and Habitable Worlds, The Pennsylvania State University, University Park, PA 16802, USA
[34] Department of Physics, Technion-Israel Institute of Technology, 32000 Haifa, Israel
[35] Physics Department, California Polytechnic State University, San Luis Obispo, CA 93407, USA
[36] Dipartimento di Matematica e Fisica, Università degli Studi Roma Tre, via della Vasca Navale 84, I-00146 Roma, Italy
[37] Department of Astronomy, University of California, Berkeley, CA 94720, USA
[38] Osservatorio Astrofisico di Arcetri, largo E. Fermi 5, I-50125, Firenze, Italy
[39] Kavli Institute for Astrophysics and Space Research, Massachusetts Institute of Technology, 77 Massachusetts Avenue, Cambridge, MA 02139, USA
[40] Crimean Astrophysical Observatory, P/O Nauchny, Crimea 298409, Russia

[41] Fountainwood Observatory, Department of Physics FJS 149, Southwestern University, 1011 East University Avenue, Georgetown, TX 78626, USA
[42] Mullard Space Science Laboratory, University College London, Holmbury St. Mary, Dorking, Surrey RH5 6NT, UK
[43] Department of Physics and Astronomy, University of Wyoming, 1000 East University Avenue, Laramie, WY 82071, USA
[44] Department of Physics and Astronomy, University of Missouri, Columbia, MO 65211, USA
[45] Department of Astronomy and Astrophysics, University of California Santa Cruz, 1156 High Street, Santa Cruz, CA 95064, USA
[46] Department of Physics and Astronomy, Wayne State University, 666 West Hancock Street, Detroit, MI 48201, USA
[47] Department of Astronomy, University of California, Riverside, CA 92521, USA
[48] INAF-IASF Bologna, Via Gobetti 101, I-40129 Bologna, Italy
[49] Department of Physics and Astronomy, Western Kentucky University, 1906 College Heights Boulevard #11077, Bowling Green, KY 42101, USA
[50] Department of Astrophysical and Planetary Sciences, University of Colorado, Boulder, CO 80309, USA
[51] Department of Earth, Environment and Physics, Worcester State University, Worcester, MA 01602, USA
[52] Institute for Computational Cosmology, Department of Physics, University of Durham, South Road, Durham DH1 3LE, UK
[53] Instituto de Astrofísica de Canarias, E-38200 La Laguna, Tenerife, Spain
[54] Nicolaus Copernicus Astronomical Center, Polish Academy of Sciences, Bartycka 18, PL-00-716 Warsaw, Poland
[55] Italian Space Agency (ASI), Via del Politecnico snc I-00133 Rome, Italy
[56] European Space Astronomy Centre, P.O. Box 78, E-28691 Villanueva de la Cañada, Madrid, Spain
[57] Department of Astronomy, University of California, Berkeley, CA 94720-3411, USA
[58] Miller Institute for Basic Research in Science, University of California, Berkeley, CA 94720, USA
[59] Department of Astronomy, San Diego State University, San Diego, CA 92182, USA
[60] Oakwood School, 105 John Wilson Way, Morgan Hill, CA 95037, USA
[61] Lick Observatory, P.O. Box 85, Mt. Hamilton, CA 95140, USA
[62] Astrophysics Science Division, NASA Goddard Space Flight Center, Mail Code 661, Greenbelt, MD 20771, USA
[63] Departamento de Astrofísica, Universidad de La Laguna, E-38206 La Laguna, Tenerife, Spain
[64] Gran Telescopio Canarias (GRANTECAN), E-38205 San Cristóbal de La Laguna, Tenerife, Spain
[65] Spectral Sciences Inc., 4 Fourth Avenue, Burlington, MA 01803, USA
[66] Eureka Scientific Inc., 2452 Delmer Street Suite 100, Oakland, CA 94602, USA
[67] Jet Propulsion Laboratory, California Institute of Technology, 4800 Oak Grove Drive, Pasadena, CA 91109, USA
[68] Space Science Center, Morehead State University, 235 Martindale Drive, Morehead, KY 40351, USA
[69] Department of Physics and Astronomy, York University, Toronto, ON M3J 1P3, Canada
[70] Department of Physics and Astronomy, University of California, Los Angeles, CA 90095, USA
[71] The Observatories of the Carnegie Institution for Science, 813 Santa Barbara Street, Pasadena, CA 91101, USA
[72] Department of Physics and Astronomy, Texas A&M University, College Station, TX 77843-4242 USA
[73] George P. and Cynthia Woods Mitchell Institute for Fundamental Physics and Astronomy, Texas A&M University, College Station, TX 77843-4242, USA
[74] Astronomy Program, Department of Physics & Astronomy, Seoul National University, Seoul, Republic of Korea
[75] Dark Cosmology Centre, Niels Bohr Institute, University of Copenhagen, Juliane Maries Vej 30, DK-2100 Copenhagen Ø, Denmark
[76] Santa Cruz Institute for Particle Physics and Department of Physics, University of California, Santa Cruz, CA 95064, USA
[77] Department of Physics and Astronomy, N283 ESC, Brigham Young University, Provo, UT 84602, USA
[78] Department of Physics, University of California, Santa Barbara, CA 93106, USA
[79] Department of Physics, Stanford University, 382 Via Pueblo Mall, Stanford, CA 94305, USA
[80] Kavli Institute for Particle Astrophysics and Cosmology, Stanford University, Stanford, CA 94305, USA
[81] SLAC National Accelerator Laboratory, 2575 Sand Hill Road, Menlo Park, CA 94025, USA
[82] Department of Astronomy and Atmospheric Sciences, Kyungpook National University, Daegu 702-701, Republic of Korea
[83] Korea Astronomy and Space Science Institute, Daejeon 34055, Republic of Korea
[84] School of Physics, University of Melbourne, Parkville, VIC 3010, Australia
[85] Pulkovo Observatory, 196140 St. Petersburg, Russia
[86] Instituto de Astronomía, Universidad Nacional Autonoma de Mexico, Cuidad de Mexico, Mexico
[87] Department of Astronomy, Columbia University, 550 West 120th Street, New York, NY 10027, USA
[88] Departamento de Astronomia, Universidad de Chile, Camino del Observatorio 1515, Santiago, Chile
[89] DiSAT, Universita dell'Insubria, via Valleggio 11, I-22100, Como, Italy
[90] Instituto de Astronomia y Ciencias Planetarias, Universidad de Atacama, Copiapó, Chile
[91] Physics Department, United States Naval Academy, Annapolis, MD 21403, USA
[92] Department of Physics and Materials Science, The University of Memphis, 3720 Alumni Avenue, Memphis, TN 38152, USA
[93] Department of Astronomy, University of Geneva, 16 Ch. d'Ecogia, 1290 Versoix, Switzerland
[94] Institute of Astronomy, Madingley Road, CB3 0HA Cambridge, UK
[95] INAF–Osservatorio Astronomico di Brera, Via E. Bianchi 46, I-23807 Merate (LC), Italy
[96] Max Planck Institut für Astronomie, Königstuhl 17, D-69117 Heidelberg, Germany
[97] Department of Physics, Faculty of Natural Sciences, University of Haifa, Haifa 31905, Israel
[98] Department of Astronomy, University of Michigan, 1085 South University Avenue, Ann Arbor, MI 48109, USA
[99] Laboratório Interinstitucional de e-Astronomia, Rua General José Cristino, 77 Vasco da Gama, Rio de Janeiro, RJ, Brazil
[100] Institute for Astronomy, 2680 Woodlawn Drive, Honolulu, HI 96822-1839, USA
[101] Las Cumbres Observatory Global Telescope Network, 6740 Cortona Drive, Suite 102, Goleta, CA 93117, USA
[102] Department of Physics and Astronomy, Vanderbilt University, 6301 Stevenson Circle, Nashville, TN 37235, USA
[103] Department of Astronomy, University of Illinois Urbana-Champaign, 1002 West Green Street, Urbana, IL 61801, USA
[104] University of Bath, Department of Physics, Claverton Down, BA2 7AY, Bath, UK

[105] Applied Physics Division, Los Alamos National Laboratory, Los Alamos, NM 87545, USA
[106] Shanghai Jiao Tong University, 800 Dongchuan Road, Shanghai, 200240, People's Republic of China
Received 2019 March 29; revised 2019 June 27; accepted 2019 July 6; published 2019 August 22

Abstract

We model the ultraviolet spectra of the Seyfert 1 galaxy NGC 5548 obtained with the *Hubble Space Telescope* during the 6 month reverberation mapping campaign in 2014. Our model of the emission from NGC 5548 corrects for overlying absorption and deblends the individual emission lines. Using the modeled spectra, we measure the response to continuum variations for the deblended and absorption-corrected individual broad emission lines, the velocity-dependent profiles of Lyα and C IV, and the narrow and broad intrinsic absorption features. We find that the time lags for the corrected emission lines are comparable to those for the original data. The velocity-binned lag profiles of Lyα and C IV have a double-peaked structure indicative of a truncated Keplerian disk. The narrow absorption lines show a delayed response to continuum variations corresponding to recombination in gas with a density of $\sim 10^5$ cm^{-3}. The high-ionization narrow absorption lines decorrelate from continuum variations during the same period as the broad emission lines. Analyzing the response of these absorption lines during this period shows that the ionizing flux is diminished in strength relative to the far-ultraviolet continuum. The broad absorption lines associated with the X-ray obscurer decrease in strength during this same time interval. The appearance of X-ray obscuration in $\sim$2012 corresponds with an increase in the luminosity of NGC 5548 following an extended low state. We suggest that the obscurer is a disk wind triggered by the brightening of NGC 5548 following the decrease in size of the broad-line region during the preceding low-luminosity state.

Key words: galaxies: active – galaxies: individual (NGC 5548) – galaxies: nuclei – galaxies: Seyfert

Supporting material: machine-readable tables

1. Introduction

Quantitatively measuring the geometry, kinematics, and physical conditions in the structures at the centers of active galactic nuclei (AGNs) is essential for understanding how their activity is fueled by inflowing gas and how outflows from the central engine may influence the surrounding host galaxy. Even in the nearest AGN, the broad-line region (BLR) and the accretion disk are nearly impossible to resolve at optical, ultraviolet (UV), or X-ray wavelengths, although the Gravity Collaboration et al. (2018) used near-IR interferometry to detect the spatial extent of the BLR of the quasar 3C 273 at an angular size of $\sim$10 μas. Reverberation mapping (Blandford & McKee 1982; Peterson 1993) provides a powerful technique for resolving features on physical scales 10 times smaller. A resolution of light-days, corresponding to angular scales of microarcseconds, suffices to probe the detailed structure of the BLR and accretion disks of nearby AGNs.

The Seyfert galaxy NGC 5548 has been a prime target of several successful reverberation mapping campaigns, both in the UV from space (Clavel et al. 1991; Korista et al. 1995) and in the optical from the ground (see Peterson et al. 2002, and references therein). These campaigns ascertained that the typical size of the BLR is several light-days and established that it was likely dominated by virial motions, since the size, ionization stratification, and line widths are all consistent with motions in a gravitational field (Peterson & Wandel 1999). These initial campaigns measured only the mean lag and line width for selected emission lines. Spurred by these successes and the promise of higher-quality data, more recent campaigns have explored the possibility of measuring lags in two dimensions with velocity-resolved reverberation mapping across strong emission-line profiles (Horne et al. 2004; Bentz et al. 2010; Grier et al. 2013).

Early efforts at velocity-resolved reverberation mapping from the ground were followed in 2014 by the first attempt to determine high-quality velocity-resolved delay maps for NGC 5548 by the AGN Space Telescope and Optical Reverberation Mapping program (AGN STORM; PI: Peterson; De Rosa et al. 2015). This program monitored NGC 5548 on a nearly daily basis for approximately 6 months using the *Hubble Space Telescope* (*HST*), the *Neil Gehrels Swift Observatory*, and several ground-based facilities, producing a data set of unparalleled quality. The campaign so far has determined mean lags for the usual bright emission lines in both the UV (De Rosa et al. 2015) and the optical (Pei et al. 2017), as well as for the continuum emission from the accretion disk (Edelson et al. 2015; Fausnaugh et al. 2016; Starkey et al. 2017).

While the AGN STORM data have exquisite quality, NGC 5548 exhibited some rather anomalous behavior over the course of the campaign. As described by De Rosa et al. (2015), the first and second halves of the campaign showed different mean lags for the emission lines. Goad et al. (2016) traced this behavior in a more detailed way to a decoupling in the response of the broad-line fluxes from the variations in the far-UV (FUV) continuum, meaning that the line fluxes stopped exhibiting the usual linear correlation with the continuum flux. This decoupling began $\sim$75 days into the campaign and lasted for another $\sim$64 days. We refer to this time period when the

[107] Einstein Fellow.
[108] Deceased, 2018 July 19.
[109] Miller Senior Fellow.
[110] Deceased, 2017 February 6.
[111] NASA Postdoctoral Program Fellow.
[112] Hubble Fellow.
[113] Packard Fellow.

broad emission lines failed to respond to variations in the continuum flux as the BLR "holiday."

Straightforward interpretation of data from a reverberation mapping campaign rests on the following four basic assumptions.

1. The illuminating continuum originates from a centrally located point that is much smaller than the BLR, and it radiates isotropically.
2. The central source and the illuminated gas occupy a small fraction of the volume encompassed by the BLR, and the continuum radiation propagates freely at the speed of light throughout this volume.
3. The observed continuum and its variations are an accurate proxy for the ionizing radiation illuminating the BLR.
4. The light-travel time across the BLR is the most important timescale.

The AGN STORM data have revealed potential issues with all of these assumptions. First, the interband continuum lags of up to a few days (Edelson et al. 2015; Fausnaugh et al. 2016) indicate a continuum region that is not pointlike, and even comparable in size to the shortest emission-line lags exhibited by He II λ1640 (De Rosa et al. 2015; Pei et al. 2017). Second, heavy intrinsic absorption affects the blue wings of the most prominent emission lines: Lyα λ1216, C IV $\lambda\lambda$1548, 1550, N V λ1238, 1242, and Si IV λ1393, 1402. This absorption consists of a broad component (FWHM of $\sim$2500 km s^{-1}) associated with the X-ray obscurer discovered by Kaastra et al. (2014) plus the known narrow UV absorption features in NGC 5548 (Crenshaw et al. 2009). The obscurer and the associated broad UV absorption are variable (Kaastra et al. 2014; Di Gesu et al. 2015), and they appear to shadow the more distant gas producing the narrow UV absorption (Arav et al. 2015), rendering those absorption lines variable as well. Third, the decoupling of the emission-line responses from the continuum variations (Goad et al. 2016) indicates a potential conflict with the third assumption. Fourth, changes in the covering factor of the absorbing gas occur on timescales of days (Di Gesu et al. 2015), comparable to the light-travel time within the BLR.

The absorbing gas outflowing from the central engine of NGC 5548 is also a key element of its nuclear structure. The blueshifted narrow intrinsic UV absorption lines associated with the X-ray warm absorber have been studied in detail for decades. A close association between the UV absorption features and the X-ray warm absorber was first proposed by Mathur et al. (1995). Mathur et al. (1999) resolved the UV absorption into six distinct components ranging in velocity from +250 to −1165 km s^{-1} and with an FWHM ranging from 40 to 300 km s^{-1}. Following their convention, these six components are enumerated, starting at the highest blueshift, as component 1 to component 6. Subsequent observations noted the variability of these features in response to changes in the UV continuum flux (Crenshaw et al. 2003, 2009; Arav et al. 2015), and Arav et al. (2015) used the variability, the density-sensitive absorption lines of C III* and P III*, and photoionization modeling to locate the UV absorbing gas at distances ranging from 3 to >100 pc. The X-ray absorbing gas is similarly complex, both kinematically and in its ionization distribution (Kaastra et al. 2002, 2014; Steenbrugge et al. 2005; Ebrero et al. 2016). Although it has been difficult to definitively link the X-ray absorbing gas to the UV absorbing gas (Mathur et al. 1995; Crenshaw et al. 2003, 2009), the apparently common spatial locations (Krongold et al. 2010) and close kinematic correspondence (Arav et al. 2015) suggest that they are part of the same outflow.

The fast, broad obscuring outflow discovered by Kaastra et al. (2014) is a new component of the nuclear structure of NGC 5548. The initial five observations of the *XMM-Newton* campaign suggested that the obscurer produced both the X-ray absorption and the broad UV absorption, and that it was located in or near the BLR (Kaastra et al. 2014). This location permits it to shadow the more distant absorbing gas producing the narrow UV absorption lines (Arav et al. 2015) and the X-ray warm absorbers (Ebrero et al. 2016). These hypotheses can be studied in greater depth with the extensive data from AGN STORM.

The AGN STORM campaign provides detailed monitoring of the variations of the UV absorption components, both broad and narrow, in response to changes in the UV and X-ray flux. To measure these variations in absorption and mitigate their influence on the measurement and interpretation of the emission lines and continuum of NGC 5548 during our campaign, we have modeled the UV spectra. Our model has the additional virtue that it deblends some of the more closely spaced emission lines, e.g., N V from Lyα and He II from C IV, so that we can produce two-dimensional reverberation maps over a wider range in velocity in each of the overlapping wavelength regions. In the process of removing the absorption, we also measure its strength, giving us an additional probe of continuum behavior along our line of sight. Since the absorption lines respond directly to changes in the ionizing flux, they provide an independent measure of its strength, which we use to reconstruct the true behavior of the ionizing continuum during the period of the BLR holiday.

The modeled spectrum and the measurements we extract from it enable a wealth of studies that we only begin to touch in this paper. In Section 2 we briefly describe the observations and initial data reduction. The spectral model we develop in Section 3 is time-dependent. We first describe the static model derived from the high signal-to-noise ratio (S/N) mean spectrum in Section 3.1. Then, in Section 3.2 we describe how we adapt this to model the whole time series of observations comprising the campaign. In Section 3.3 we describe how we estimate the uncertainties we measure using our time-dependent models. In Section 3.4 we describe various tests we made to assess the quality and reliability of our procedures. With the modeled spectra in hand, we then describe how we make measurements using the models. This includes describing the absorption-corrected spectra in Section 3.5, how we measure fluxes in the deblended emission lines in Section 3.6, and how we measure the absorption lines in Section 3.7. Using these measurements, in Section 4 we perform an initial analysis of our results, including velocity-resolved light curves for the deblended emission lines in Section 4.1 and the physical characteristics we infer for the gas producing the intrinsic narrow and broad absorption lines based on the mean spectrum in Section 4.2. In Section 4.3 we analyze the variability of the intrinsic narrow absorption lines, and in Section 4.4 we analyze the variability of the intrinsic broad absorption features associated with the obscurer. In Section 5 we discuss the implications of our results for the structure and evolution of the BLR in NGC 5548, and in Section 6 we summarize our major results.

2. Observations and Data Reduction

Our observational program is described in detail by De Rosa et al. (2015). Summarizing briefly, we observed NGC 5548 using the Cosmic Origins Spectrograph (COS; Green et al. 2012) on *HST* using daily single-orbit visits from 2014 February 1 through July 27. Out of 179 observations, 171 executed successfully. To cover the full spectral range of the COS medium-resolution gratings, we used multiple central wavelength and FP-POS settings. Each visit used two different settings for gratings G130M and G160M. These settings covered the wavelength range 1153–1796 Å in all visits. Different settings on each day over an eight-visit cycle enabled us to regularly sample a broader spectral range, 1130–1810 Å, over the course of the whole program. This strategy also minimized damage and charge extraction from the COS detectors over the duration of our program. This broader spectral coverage, particularly on the blue-wavelength end, enabled us to sample the P V λ1128 absorption line, an important tracer of high column density absorbing gas (Arav et al. 2015). Our spectra on each visit exceeded a minimum S/N of >20 in the continuum at 1367 Å when measured over 100 km s^{-1} bins.

2.1. Data Reduction

As described by De Rosa et al. (2015), we used the `CalCOS` pipeline v2.21 to process our data, but we made a special effort to enhance the calibration files for our particular observations. We developed special flat-field files, enhanced the wavelength calibration through comparison to prior Space Telescope Imaging Spectrograph (STIS) observations of NGC 5548, and tracked the time-dependent sensitivity of COS to achieve higher S/N and better flux reproducibility. For each day, all four exposures were calibrated, aligned in wavelength, and combined into a single spectrum for each grating for each visit. We binned these spectra by 4 pixels (approximately half a resolution element) to reduce residual pattern-noise features and achieve higher S/N. Ultimately, our wavelength scale achieves an rms precision of <6 km s^{-1}, and our flux reproducibility is better than 1.1% for G130M and better than 1.4% for G160M.

3. The Time-dependent Spectral Model

3.1. Modeling the Mean Spectrum

To produce a spectral model that can be adjusted to each individual observation in the reverberation campaign, we start with the high-quality mean spectrum produced from the whole campaign data set. This reveals individual weak features that we cannot precisely track in individual observations but that we must include to avoid biasing our results for stronger features of interest. The model of the mean spectrum is described in detail by De Rosa et al. (2015), but we also describe it here once again as a key reference for understanding the components that we vary in the fits to the individual spectra in our campaign's time series.

The basic model starts with the one developed for the *XMM-Newton* campaign of Kaastra et al. (2014), where the soft X-ray obscuration and broad UV absorption were first discovered. This model used a power-law continuum and multiple Gaussian components for both the emission and the broad absorption features. The high S/N of the mean spectrum from the reverberation mapping campaign requires the addition of more weak emission features, additional weak broad absorption features associated with all permitted transitions in the spectrum, and more components in the bright emission lines. We emphasize that the model is not intended as a physical characterization of the spectrum but rather as an empirical tool that enables us to deblend emission-line components and correct for absorption by using some simple assumptions about the shape of the spectrum.

Starting with the continuum, we use a power law with $F_\lambda(\lambda) = F_\lambda(1000\ \text{Å})\ (\lambda/1000\ \text{Å})^{-\alpha}$. Although Kraemer et al. (1998) found a modest amount of internal extinction in the narrow-line region (NLR) of NGC 5548, $E(B-V) = 0.07^{+0.09}_{-0.06}$, the continua of Type 1 AGNs in general show little extinction (Hopkins et al. 2004), and none was required in fitting the broadband spectral energy distribution (SED) of NGC 5548 (Mehdipour et al. 2015). Given that our continuum model is simply an empirical characterization of its shape, we assume there is no internal extinction in NGC 5548, and we redden the power law with Galactic foreground extinction of $E(B-V)$ fixed at 0.017 mag (Schlegel et al. 1998; Schlafly & Finkbeiner 2011) using the mean Galactic extinction curve of Cardelli et al. (1989) with $R_V = 3.1$. Weak, blended Fe II emission is expected at $\lambda > 1550$ Å, which we include as modeled by Wills et al. (1985) and broadened with a Gaussian with FWHM = 4000 km s^{-1}. This model component is essentially a smooth, low-level addition to the continuum at long wavelengths, and it has no predicted or observed spectral features associated with it. Also, as revealed in prior monitoring campaigns on NGC 5548, the Fe II varies only weakly (Krolik et al. 1991; Vestergaard & Peterson 2005) on timescales of weeks. During AGN STORM, the optical Fe II emission varied by at most 10% from its mean value (Pei et al. 2017). In the UV model, we therefore keep its intensity fixed, and we normalize its flux using the modeled Fe II emission from the mean *XMM-Newton* Optical Monitor grism spectrum of Mehdipour et al. (2015).

For the emission lines, we use multiple Gaussian components. We do not assign any particular physical significance to most of these individual kinematic components, especially since there is no unique way to decompose these line profiles using such nonorthogonal elements. However, the narrow and intermediate-width components of Lyα, N V, C IV, and He II are discernible as discrete entities in prior observations of NGC 5548 in faint states (Crenshaw et al. 2009). Although narrow Si IV was not present in the 2004 STIS spectrum of Crenshaw et al. (2009), our high-S/N mean spectrum requires it, and we include it in our fit. Similarly, there is a nonvarying intermediate-width component with FWHM $\sim$ 800 km s^{-1} in Lyα, N V, Si IV, C IV, and He II. We call this the intermediate-line region (ILR). In weaker emission lines, such as C III* λ1176, Si III λ1260, Si II + O I λ1304, C II λ1335, N IV] λ1486, O III] λ1663, and N III] λ1750, this intermediate-width component is the only one observed in the spectrum.

Crenshaw et al. (2009) saw little or no evidence for variability of the NLR and ILR components. We allow these to vary freely in determining our best fit to the mean spectrum, but for the bright emission lines (Lyα, N V, Si IV, C IV, and He II), we keep these components fixed when fitting the individual spectra from the campaign. For the weaker, lower-ionization emission lines listed above, however, we allow their flux, central wavelength, and FWHM to vary, since these lines are not heavily blended with other components.

The strongest emission lines (Lyα, N V, Si IV, C IV, and He II) all require up to three additional broad components. These have approximate widths of 3000 (broad, or B), 8000 (medium broad, or MB), and 15,000 (very broad, or VB) km s^{-1}. The N V, Si IV, and C IV emission lines are all doublets. We allow for independent narrow, intermediate, B, and MB components for each doublet transition. In each case, we link their wavelengths at the ratio of their vacuum values, assign them the same FWHM, and assume that their relative fluxes have an optically thick 1:1 ratio. For the VB component, however, which is much broader than the doublet separations, we use only a single Gaussian for each ion.

A final set of empirical emission components in our model accounts for weak bumps on the red and blue wings of C IV and the red wing of Lyα. These bumps have an interesting variability pattern that we discuss later, and they are especially visible in the rms spectrum shown by De Rosa et al. (2015) in their Figures 1 and 2. We use Gaussian components for each of these features.

We do not model the narrow, intrinsic absorption lines in NGC 5548 or the foreground interstellar lines, but we do model the variable intrinsic broad absorption associated with the obscurer discovered by Kaastra et al. (2014). The strongest, most easily modeled broad absorption features are on the blue wings of the Lyα, N V, Si IV, and C IV emission lines. For these, like Kaastra et al. (2014), we use an asymmetric Gaussian with negative flux. To specify the asymmetry, we use a larger dispersion on the blue side of the central wavelength than on the red side. We allow the ratio of blue to red dispersion to vary as a free parameter. This parameterization produces a rounded triangular shape with the deepest point in the trough near the red extreme and a blue wing that extends far out along the blue wing of the emission line. (Kaastra et al. 2014 showed these profiles in their Figure 2.) We emphasize that this absorption profile is strictly an empirical characterization of the observed flux in the spectrum that has no independent physical meaning. Deriving physical information requires making further assumptions about which emission components are covered, producing a transmission profile, and integrating that profile to obtain the actual opacity. We discuss these measurements later in Section 3.7.

In addition to these main troughs, additional small depressions appear further out on the blue wings. We model these with additional symmetric Gaussians in negative flux. As with the emission lines, the absorption in N V, Si IV, and C IV is due to doublets. These are unresolved, and we assume they are optically thick. We model each line in the doublet using the same shape and depth. Finally, all of the UV resonance lines in the spectrum have weak, blueshifted absorption troughs at velocities comparable to the main portion of the troughs observed in Lyα, N V, Si IV, and C IV. These cannot be modeled in the detail that we apply to the strongest absorption troughs, and they are only readily apparent in the mean spectrum. For these troughs, we use symmetric Gaussians in negative flux.

The final component of our model is absorption of all model components by damped Lyα from the Milky Way. We fix the column density at $N(\mathrm{H\,I}) = 1.45 \times 10^{20}\,\mathrm{cm}^{-2}$ (Wakker et al. 2011).

Figure 1 gives a detailed view of the best-fit model overlaid on the data. We illustrate all individual components of the model, the best-fit model overlaid on the data, and the absorption-corrected model (which is the ultimate goal of our efforts). Note that the C IV absorption is not as deep in the mean spectrum from the reverberation campaign as it was during the deepest phase of the obscuration as observed in the *XMM-Newton* campaign (see Figure S1 in Kaastra et al. 2014, which shows the individual components of the region surrounding the C IV emission line). For further illustrations of our model of the mean spectrum, see Figures 1 and 2 of De Rosa et al. (2015), which compare the model to the full G130M and G160M spectra.

All of the model parameters are listed in Table 1. The model consists of a total of 97 individual components, each with two to four parameters. Although the total number of parameters is 383, many of these are fixed or linked to other parameters. Free parameters in the fit total 143. Although this is a large number, the fit is tightly constrained. The fitted regions in the mean spectrum comprise ~12,598 points, each approximately half of a resolution element. Thus, each spectrum has ~6000 spectral elements included in the fit, and that is described by only 143 parameters.

To optimize the parameters of the model and obtain the best fit, we use a combination of minimization algorithms. After determining initial guesses by visual inspection, we start the optimization process using a `simplex` algorithm (Murty 1983). This works well for problems with many parameters that are not initially well tuned. Once the fit is nearly optimized, this algorithm generally loses efficiency in approaching full convergence. At that point (usually after several tens of iterations), we switch to a Levenberg–Marquardt algorithm (as originally coded by Bevington 1969). When close to an optimum fit, this algorithm converges rapidly, but with the large number of parameters in our fit, it can get stuck in false minima. To escape these pitfalls, we then alternate sets of 5–10 iterations using the `simplex` algorithm and the Levenberg–Marquardt algorithm until the fit has fully converged. We define full convergence as $\Delta\chi^2 < 0.01$ and a change in each parameter value of <1% after a set of iterations.

3.2. Modeling the Whole Time Series

As we noted above, our Gaussian decomposition of the emission lines is not unique. Therefore, unless one takes care to preserve the overall character of the spectral shape of the model from visit to visit among the individual observations, best fits and parameters can wander far from the character of our fit to the mean spectrum. One could try to avoid this by tailoring initial guesses for fits to each individual spectrum interactively, but this would introduce a unsatisfying degree of subjectivity into our final results. We therefore employed an approach that used the quantitative characteristics of the spectra to tune each individual fit and guide it to an optimum result. We verified the soundness of this approach through multiple trials and experiments before converging on a process that produced consistent results from spectrum to spectrum without drastic changes in parameters that might signify unphysical solutions.

In our first trials, we noticed that most weak emission and absorption features were often too weak to be effectively constrained in a single observation. We therefore produced a series of grouped spectra that improved the S/N for our measurements of these weak spectral features. As described in De Rosa et al. (2015), the observations were done in a cycle of eight, where central wavelength settings and FP-POS positions were changed on a daily basis. Combining spectra according to these natural groups produces better S/N, reduces pattern noise, and provides the full spectral coverage that extends down to the

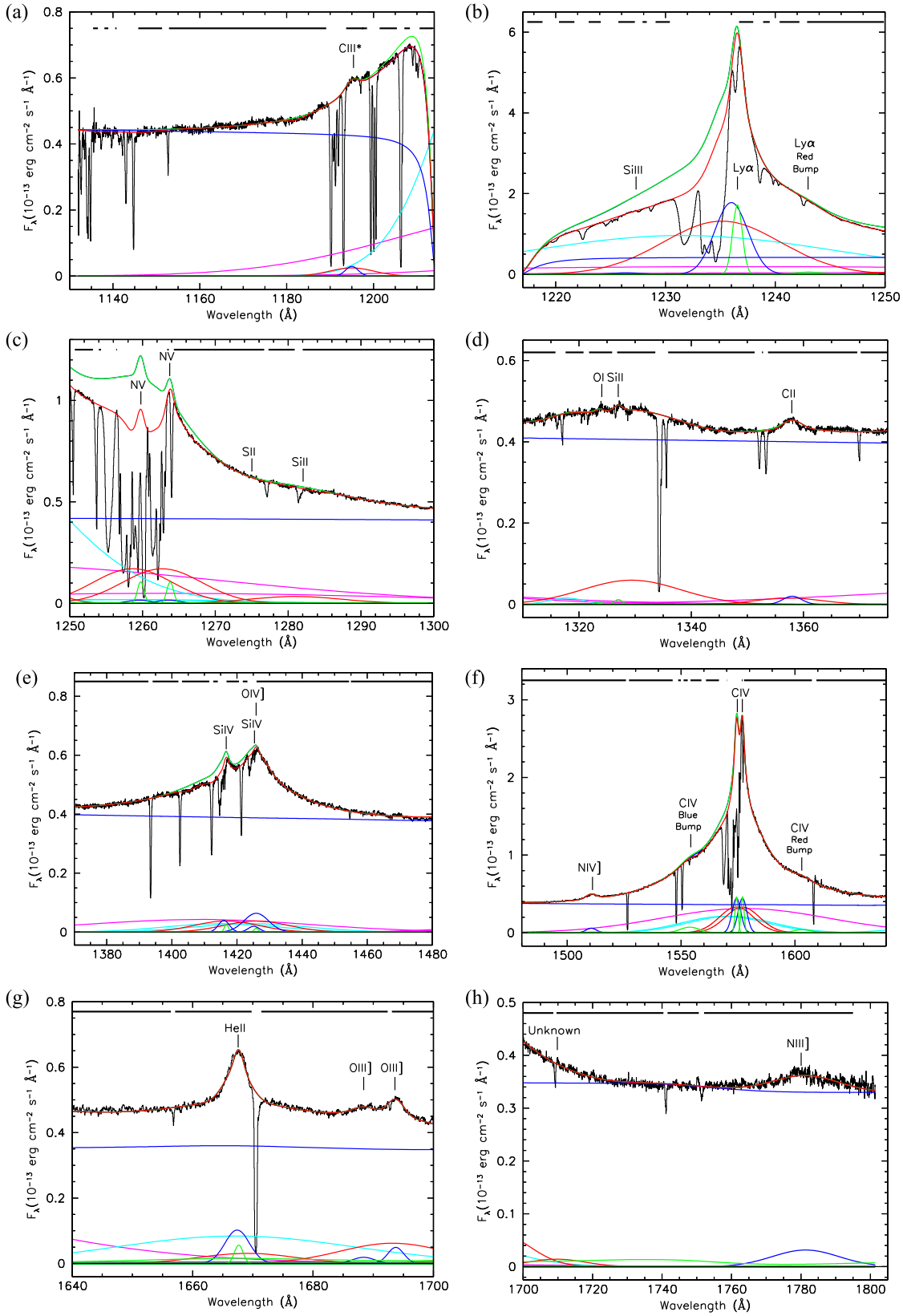

Figure 1. (a) NGC 5548 mean COS spectrum, 1130–1214 Å. The best-fit model for the COS UV spectrum of NGC 5548 is overlaid on the data (black). The total best-fit model is in red. The model corrected for absorption is in green. (Damped Galactic Lyα is not corrected.) The continuous solid blue line in each panel is the continuum component absorbed by damped Galactic Lyα. Emission lines from Table 1 are marked. Narrow emission-line region components are in green, ILR components are in blue, B components are in red, MB components are in cyan, and VB components are in magenta. Thick horizontal bars across the top indicate wavelength intervals used for the fit. Fluxes and wavelengths are in the observed frame. (b) NGC 5548 mean COS spectrum, 1217–1250 Å. (c) NGC 5548 mean COS spectrum, 1250–1300 Å. (d) NGC 5548 mean COS spectrum, 1310-1375 Å. (e) NGC 5548 mean COS spectrum, 1370–1480 Å. (f) NGC 5548 mean COS spectrum, 1480–1640 Å. (g) NGC 5548 mean COS spectrum, 1640–1700 Å. (h) NGC 5548 mean COS spectrum, 1700–1805 Å.

Table 1
Model Parameters for the Mean Spectrum of NGC 5548

Feature	Component[a] Number	λ_{vac} (Å)	λ_{obs} (Å)	Flux[b]	FWHM (km s^{-1})	Asymmetry[c]	Freedom[d] Flags
Power law $F_\lambda(1000)$	1	5.978[e]					0
Power law α	1	0.840					0
$E(B-V)$	2	0.017					−1
R_V	2	3.1					−1
Galactic Lyα	66	1215.67	1215.55	1.45[f]			−1
C III*	3	1175.78	1195.01	1.06	861	1.00	0, 0, 0, −1
C III* B	95	1175.78	1195.01	3.13	3000	1.00	0, 0, 0, −1
Si III	4	1206.50	1226.39	1.44	861	1.00	0, 0, 3, −1
Lyα narrow	5	1215.67	1236.55	19.3	255	1.00	0, 0, 0, −1
Lyα intermediate	6	1215.67	1236.00	67.3	861	1.00	0, 0, 0, −1
Lyα B	7	1215.67	1235.14	176.0	3047	1.00	0, 0, 0, −1
Lyα MB	8	1215.67	1231.59	340.0	8074	1.00	0, 0, 0, −1
Lyα VB	9	1215.67	1237.64	154.0	18347	1.00	0, 0, 0, −1
Lyα red bump	21	1215.67	1243.04	1.73	713	1.00	0, 0, 0, −1
N V narrow	10	1238.82	1259.75	1.22	255	1.00	0, 0, 5, −1
N V narrow	11	1242.80	1263.80	1.22	255	1.00	10, 10, 10, −1
N V intermediate	12	1238.82	1259.53	0.62	861	1.00	6, 0, 6, −1
N V intermediate	13	1242.80	1263.58	0.62	861	1.00	12, 12, 12, −1
N V B	14	1238.82	1258.66	23.3	3047	1.00	7, 0, 7, −1
N V B	15	1242.80	1262.70	23.3	3047	1.00	14, 14, 14, −1
N V MB	16	1238.82	1255.04	6.85	8074	1.00	8, 0, 8, −1
N V MB	17	1242.80	1259.08	6.85	8074	1.00	16, 16, 16, −1
N V VB	18	1240.01	1263.24	40.8	18347	1.00	9, 0, 9, −1
S II	19	1253.81	1273.00	0.09	841	1.00	0, 0, 0, −1
Si II	20	1260.42	1281.00	5.39	3500	1.00	0, 0, 0, −1
O I narrow	48	1302.17	1323.52	0.10	359	1.00	0, 0, 0, −1
Si II narrow	49	1304.37	1327.01	0.20	359	1.00	0, 0, 48, −1
Si II+O I B	50	1303.27	1329.35	13.1	4659	1.00	0, 0, 0, −1
Unknown	47	…	1317.76	1.24	1687	1.00	0, 0, 0, −1
C II intermediate	94	1334.53	1358.00	0.83	861	1.00	0, 0, 34, −1
C II B	51	1334.53	1357.36	2.28	3000	1.00	0, 0, −1, −1
Si IV narrow	96	1393.76	1416.74	0.41	303	1.00	0, 0, 0, −1
Si IV narrow	97	1402.77	1425.90	0.20	303	1.00	96, 96, 96, −1
Si IV intermediate	23	1393.76	1415.97	1.67	842	1.00	0, 0, 0, −1
Si IV intermediate	24	1402.77	1425.13	0.84	842	1.00	23, 23, 23, −1
Si IV B	25	1393.76	1416.74	9.29	4889	1.00	0, 0, 0, −1
Si IV B	26	1402.77	1425.90	9.29	4889	1.00	25, 25, 25, −1
Si IV MB	27	1393.76	1415.28	12.5	8704	1.00	0, 0, 0, −1
Si IV MB	28	1402.77	1424.43	12.5	8704	1.00	27, 27, 27, −1
Si IV VB	29	1398.26	1409.20	37.1	18148	0.92	0, 0, 0, −1
O IV]	52	1400.00	1425.92	6.00	1858	1.00	0, 0, 0, −1
N IV] intermediate	39	1486.00	1510.54	3.30	1050	1.00	0, 0, 0, −1
N IV] B	22	1486.00	1512.13	1.83	3800	1.00	0, 0, −1, −1
C IV narrow	30	1548.20	1574.34	7.86	303	1.00	0, 0, 0, −1
C IV narrow	31	1550.77	1576.96	7.86	303	1.00	32, 32, 32, −1
C IV intermediate	32	1548.20	1574.32	21.4	861	1.00	0, 0, 0, −1
C IV intermediate	33	1550.77	1576.93	21.4	861	1.00	34, 34, 34, −1
C IV B	34	1548.20	1574.28	62.3	3366	1.00	0, 0, 0, −1
C IV B	35	1550.77	1576.90	62.3	3366	1.00	36, 36, 36, −1
C IV MB	36	1548.20	1569.00	98.5	8345	1.00	0, 0, 0, −1
C IV MB	37	1550.77	1571.61	98.5	8345	1.00	0, 0, 0, −1
C IV VB	38	1550.48	1577.99	286.0	16367	1.00	0, 0, 0, −1
C IV blue bump	93	1550.48	1553.79	7.53	1900	1.00	0, 0, 0, −1
C IV red bump	74	1550.48	1603.34	3.95	1708	1.00	0, 0, 0, −1
He II narrow	40	1640.45	1667.66	1.01	303	1.00	0, 0, 30, −1
He II intermediate	41	1640.45	1667.40	5.22	861	1.00	0, 0, 32, −1
He II B	42	1640.45	1669.07	6.18	3366	1.00	0, 0, 34, −1
He II MB	43	1640.45	1667.10	41.5	8345	1.00	0, 0, 36, −1
He II VB	67	1640.45	1667.14	4.93	16367	1.00	0, 0, 38, −1
O III] narrow	92	1660.00	1686.82	0.87	771	1.00	0, 47, 0, −1
O III] narrow	44	1666.00	1693.74	1.64	555	1.00	0, 0, 0, −1
O III] B	45	1663.00	1693.23	13.5	3639	1.00	0, 0, 0, −1
Unknown	68	…	1709.64	2.91	3366	1.00	0, 0, 0, −1

Table 1
(Continued)

Feature	Component[a] Number	λ_{vac} (Å)	λ_{obs} (Å)	Flux[b]	FWHM (km s^{-1})	Asymmetry[c]	Freedom[d] Flags
N III] B	46	1750.00	1781.33	7.56	3801	1.00	0, 0, 0, −1
Fe II	53	…	…	13.91[g]	1861.0	…	−1, 0, 0, −1
C III* broad absorption	54	1175.78	1194.00	−0.01	3796	0.13	0, 0, 55, 55
Lyα broad absorption	55	1215.67	1235.00	−71.62	3796	0.13	0, 0, 0, 0
N V broad absorption	56	1238.82	1258.00	−9.19	3796	0.13	0, 0, 55, 55
N V broad absorption	57	1242.80	1262.04	−9.19	3796	0.13	56, 56, 55, 55
S II broad absorption	58	1253.81	1266.63	−0.94	3796	0.13	0, 0, 55, 55
Si II broad absorption	59	1260.42	1284.47	−0.93	3796	0.13	0, 0, 55, 55
Si II broad absorption	60	1304.37	1322.46	−0.18	3796	0.13	0, 0, 55, 55
C II broad absorption	61	1334.53	1355.00	−0.18	1761	0.26	0, 0, 0, −1
Si IV broad absorption	62	1393.76	1415.20	−1.91	3796	0.13	0, 0, 55, 55
Si IV broad absorption	63	1402.77	1424.36	−1.91	3796	0.13	62, 62, 55, 55
C IV broad absorption	64	1548.20	1572.02	−5.18	2963	0.13	0, 0, 55, 55
C IV broad absorption	65	1550.77	1574.63	−5.18	2963	0.13	64, 64, 55, 55
P V broad absorption	69	1117.98	1136.00	−0.23	3796	0.65	0, 0, 55, 0
P V broad absorption	70	1128.01	1146.19	−1.06	3796	0.65	0, 69, 69, 69
Si II broad absorption	71	1190.20	1212.26	−3.25	3796	0.13	0, 55, 55, 55
Si III broad absorption	72	1206.50	1225.63	−0.94	3796	0.13	0, 55, 55, 55
Si II broad absorption	73	1526.71	1557.83	−1.92	3796	0.13	0, 55, 55, 55
C III broad absorption	75	1175.78	1182.00	−0.31	1000	1.00	0, −1, −1, −1
Lyα broad absorption	76	1215.67	1221.87	−1.80	1000	1.00	−1, 0, −1, −1
N V broad absorption	77	1238.82	1245.14	−1.11	1000	1.00	−1, 0, −1, −1
N V broad absorption	78	1242.80	1249.14	−1.11	1000	1.00	77, −1, −1, −1
S II broad absorption	79	1253.81	1260.20	−7.13	1000	1.00	76, 0, −1, −1
Si II broad absorption	80	1260.42	1266.93	−1.21	1000	1.00	76, 0, −1, −1
Si II broad absorption	81	1304.37	1310.65	0.00	1000	1.00	76, 0, −1, −1
C II broad absorption	82	1334.53	1341.81	−0.02	1000	1.00	76, 0, −1, −1
Si IV broad absorption	83	1393.76	1405.00	−0.41	1000	1.00	76, 0, −1, −1
Si IV broad absorption	84	1402.77	1414.09	−0.41	1000	1.00	83, 83, −1, −1
C IV broad absorption	85	1548.20	1556.09	−0.74	1000	1.00	76, 0, −1, −1
C IV broad absorption	86	1550.77	1558.68	−0.74	1000	1.00	85, 85, −1, −1
P V broad absorption	87	1117.98	1136.00	−0.09	1000	1.00	76, 0, −1, −1
P V broad absorption	88	1128.01	1146.19	−0.01	1000	1.00	76, 87, −1, −1
Si II broad absorption	89	1190.42	1199.38	0.00	1000	1.00	76, 0, −1, −1
Si III broad absorption	90	1206.50	1212.61	0.00	1000	1.00	76, 0, −1, −1
Si II broad absorption	91	1526.71	1541.27	−0.19	1000	1.00	76, 0, −1, −1

Notes.
[a] Component number in the `specfit` model. Each component has multiple parameters as given in the table.
[b] Flux is in 10^{-14} erg cm^{-2} s^{-1}.
[c] Asymmetry is defined as the ratio of the half-width at half-maximum of the red side of an asymmetric Gaussian to the half-width at half-maximum of the blue side.
[d] Key for freedom flags: For each component, flags are given for each parameter—λ_{obs}, flux, FWHM, and asymmetry. Values correspond to the following: −1 (fixed), 0 (free), $N > 0$ (linked to corresponding parameter of component N).
[e] Flux is in 10^{-14} erg cm^{-2} s^{-1} Å^{-1}.
[f] Column density is in 10^{20} cm^{-2}.
[g] The Fe II model is normalized to 1.0×10^{-16} erg cm^{-2} s^{-1} Å^{-1} at 1700 Å.

P V region at the short-wavelength end. In the fits to the time series we discuss below, we use the values for the weak features determined from these grouped spectra as our initial guess for starting parameters when fitting the individual spectra in a group.

Another outcome of our trials, perhaps an obvious one, is that good initial choices for parameters led to quicker convergence and less chance of solutions where parameters strayed into unphysical regions of parameter space. Thus, given our exquisite fit to the mean spectrum, its parameters provide the best guess for spectra that are similar. To strengthen this similarity from fit to fit, we tried two different methods. First, we ordered the spectra by the flux level in the 1367 Å continuum window. We then chose the spectrum near the middle of this distribution with the flux most comparable to the flux in the mean spectrum as the first one to fit. The best fit from this spectrum was then used as the initial guesses for parameters in fitting the next spectra in the series. The series of fits followed two parallel paths moving both higher and lower in flux from this initial middle spectrum. Our second method was to keep the spectra ordered by time and then pick a spectrum close to the midpoint of the campaign with a mean continuum close to that of the mean spectrum. Fits then progressed both forward and backward in time from this middle point.

These experiments validated our intentions to develop an objective process for determining the best fit to each spectrum. Both methods achieved good fits for all spectra, and the parameters from each method were close in value to each other

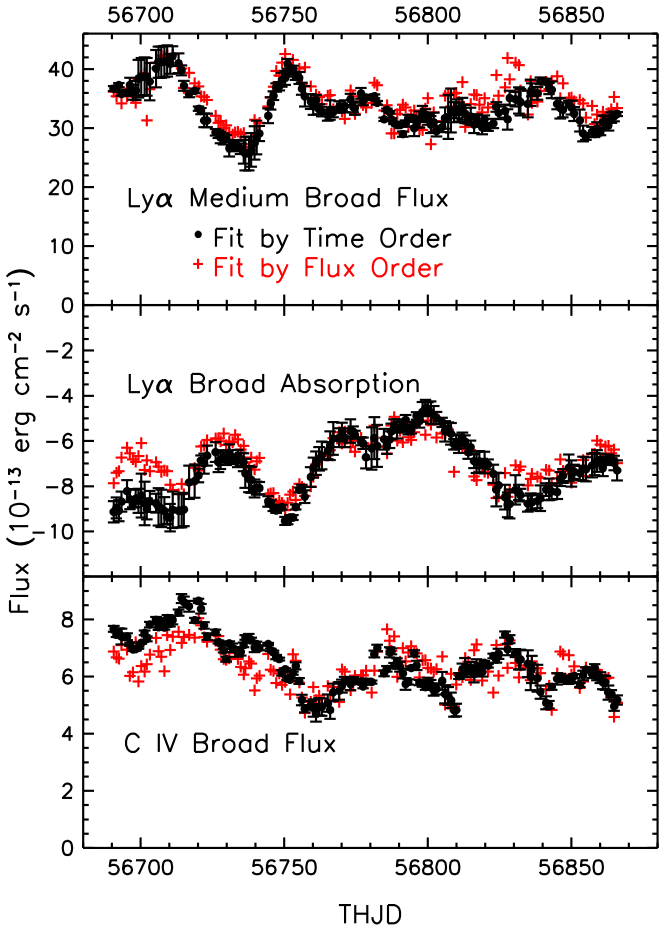

Figure 2. Examples of the evolution of selected parameters comparing values obtained from fits using time-ordered spectra (black points with error bars) to values from fits using flux-ordered spectra (red plus signs). The top panel shows the Lyα MB flux, the middle panel shows the Lyα broad absorption, and the bottom panel shows the C IV broad flux.

(typically within the 1σ uncertainties). Figure 2 compares the values obtained as a function of time for the two different methods for three selected parameters from the model. In Figure 2 and the remainder of the paper, we define times by the Truncated Heliocentric Julian Date (THJD), THJD = HJD−2,400,000.

Despite the good agreement in the quality of the fits for the two different methods, our experiments also showed that the second method, "ordered by time," produced better results than "ordered by flux," in the sense that variations in parameter values were smoother, and, as shown in Figure 3, the best-fit χ^2 was typically slightly less. Despite the significant reduction in χ^2 we achieved for the fits ordered by time, the differences in the fits are not obvious. We note that for each method, χ^2 varies systematically with time during the campaign. The variations loosely correspond to the overall variations in brightness of NGC 5548 (as one can see in later figures showing light curves for the continuum and emission line). Our inference for these systematic variations is that the brighter spectra have higher S/N per pixel, and that subtle residual pattern noise in the flat-field properties of the COS detectors degrades the quality of our fits. Figure 4 compares the best-fit models to the data for two extreme cases, our overall lowest χ^2 solution for visit 38 and our overall highest χ^2 obtained for visit 60. One is hard-pressed to see the differences between the models fit using either

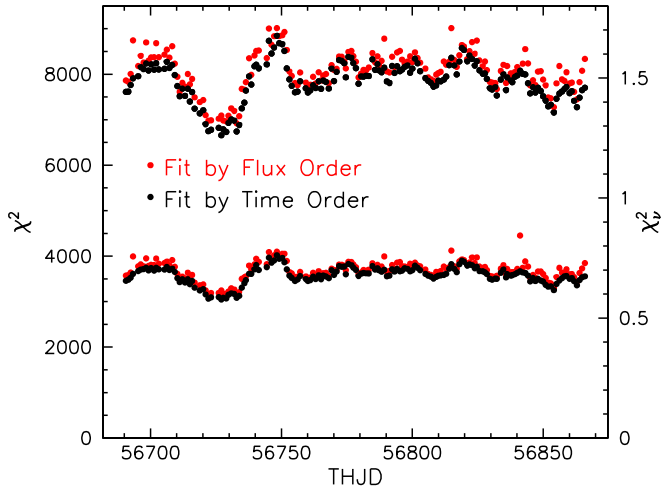

Figure 3. Minimum χ^2 achieved in the fit to each spectrum in the campaign (upper curves and left axis). Black points show the results for our adopted method of fitting the sequence of spectra in time order. Red points show the results for fitting the spectra when ordered by flux. The lower curves and right axis show the reduced χ^2. The reduced χ^2 is considerably less than 1, indicating that our errors are overestimated, likely due to correlated errors, as discussed in Section 3.4.

method, or even why χ^2 is significantly higher for visit 60 compared to visit 38.

Our best inference for why the "ordered by time" sequence produces better results is that the spectrum evolves on timescales of a few days. This is measured in the lags of the emission lines, and, as we will show later in Section 5.2, it is also true for the absorption features. Therefore, although one spectrum might have the same continuum flux as another, if it is separated in time by more than several days, the parameters of major features may differ significantly, making it harder for the minimization algorithm to converge on the best solution.

To fit an individual spectrum, we first determined the best first approximation to the normalization and spectral index of the power-law continuum by fitting only those points identified by De Rosa et al. (2015) as continuum windows. To avoid "contaminating" these windows with broad-line flux, we also set the flux of all of the VB components to zero. In our experiments, we found that if we did not do this, the VB components developed a tendency to grow in width until they formed their own pseudo-continuum across the whole spectrum. In this first pass, only the power-law normalization and index were allowed to vary freely.

After this step, we optimized the strength of the brightest emission lines—Lyα, N V, Si IV, C IV, and He II—and let the fluxes of their B and MB components and the power-law normalization vary freely, while keeping the power-law index fixed and the VB component turned off. Next, we restored the VB fluxes to their original values, and let the fluxes of all broad components of the above lines vary freely, as well as the power-law normalization.

At this point, the fit formed a remarkably good representation of an individual observation, but it was still far from the best fit. In the next steps, we turned our attention to optimizing the fits for each individual bright emission line. In these separate steps, we kept all parameters not related to the specific spectral region fixed, including the continuum parameters, Fe II flux, narrow- and intermediate-line components for all lines, and any weak blended lines.

For the Lyα region, we did separate optimization steps in the following order.

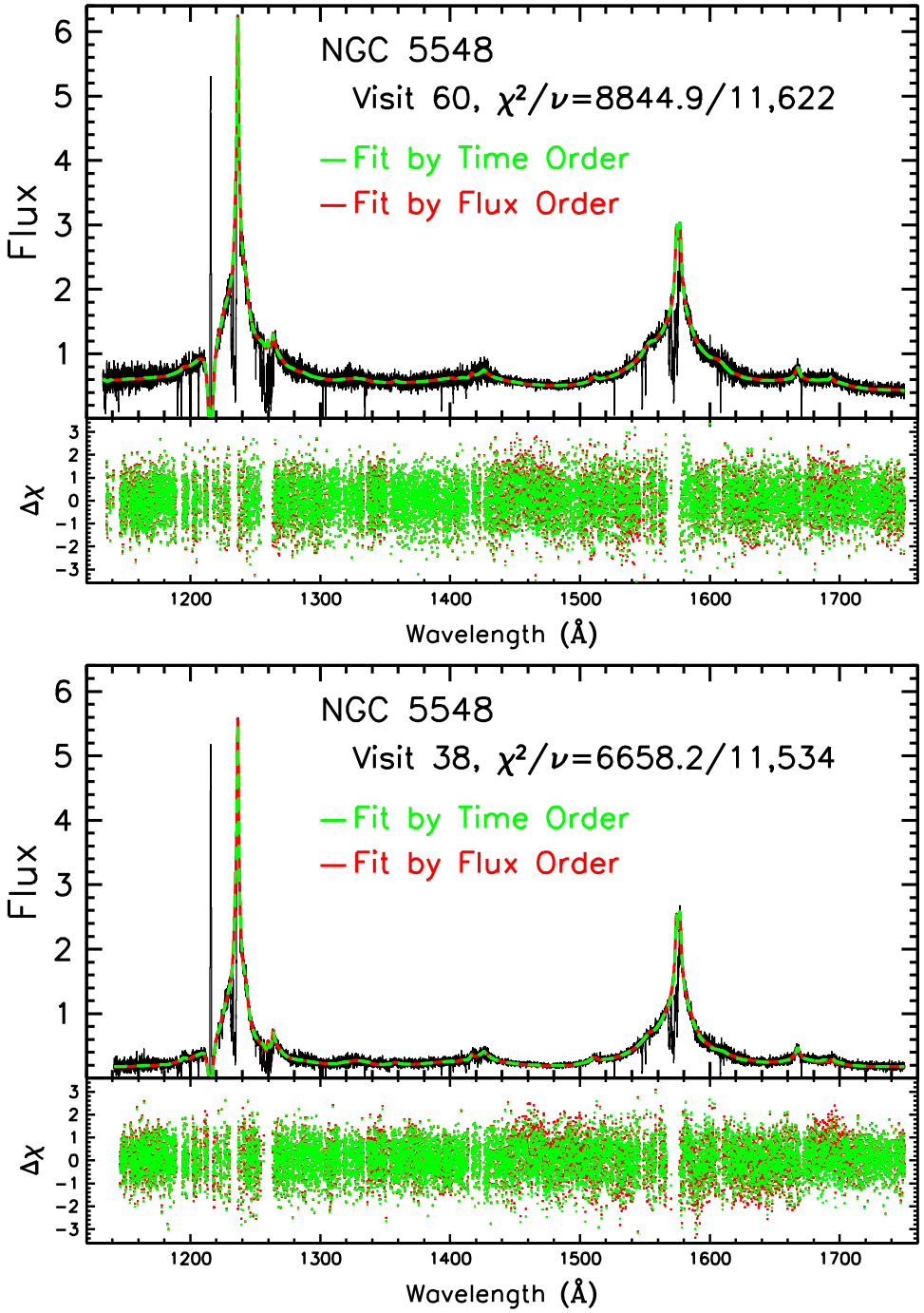

Figure 4. (Top) Best-fit models overplotted on the visit 60 spectrum. This model has the worst χ^2 for the ensemble of fits. The adopted best-fit model curve (from fits done in time order) is in green; the best-fit model for the fits done when ordered by flux is in red. Flux is in the observed frame in units of 10^{-14} erg cm^{-2} s^{-1} Å^{-1}. Residuals to the fits are shown as points ("+") scaled by the 1σ uncertainties, e.g., $\Delta\chi$ = (Data − Model)/Error. (Bottom) Same as top panel for the visit 38 spectrum, which has the best χ^2.

1. Fit Lyα only (B, MB, VB) using only wavelengths 1150–1245 Å. As before, let the fluxes vary freely first, then both the widths and fluxes. Keep all components of N V fixed throughout this.
2. Fit the red wing of N V using only wavelengths 1263–1300 Å. Keep Lyα and all other components fixed. Let the two B components vary freely first, then fix them and let the MB components vary. Finally, fix those and let the VB component vary.
3. Fit the N V absorption on its blue wing, keeping the doublet's fluxes tied at a 1:1 ratio, using only wavelengths 1245–1264 Å.
4. Free the flux and width of the B, MB, and VB components of Lyα.
5. Free the flux and width of the B, MB, and VB components of N V.
6. Free the flux of the Lyα B absorber.
7. Free the flux, width, and asymmetry of the Lyα B absorber.

We next did the Si IV region. All parameters that we varied freely above for the optimization of the Lyα region were fixed, and we then did the following.

1. Free the flux of the B, MB, and VB components of Si IV.
2. Free the flux and width of the B, MB, and VB components of Si IV.
3. Free the flux of the Si IV B absorber. (Since the Si IV absorption is so weak, we linked the width and asymmetry of the Si IV B absorber to that of C IV.)

We fit C IV and He II together, since they are tightly blended. For optimizing this region, we fix all of the previous freely varying parameters, then do the following.

1. Free the flux and width of the B, MB, and VB components of C IV.
2. Free the flux (but not the width) of the B, MB, and VB components of He II.
3. Free the flux of the C IV B absorber.
4. Free the flux, width, and asymmetry of the C IV B absorber.

Once the major emission and absorption components are tuned up, we then allow the weaker emission-line features to adjust. We keep the continuum fixed, as well as all of the parameters associated with Lyα, N V, Si IV, C IV, and He II. The fluxes of all other weak emission features are then allowed to vary.

To complete the optimization, all parameters designated as free to vary in Table 1 are freed, and we iterate the χ^2 minimization process until it converges. The best-fit parameters for this spectrum are then used as the initial guesses for doing the fit to the next spectrum in the series (with the exception that the initial guesses for the weak features are taken from the best fit to the grouped spectrum corresponding to that spectrum). Final values of all components as a function of wavelength for each spectrum are available as a high-level science product in the Mikulski Archive for Space Telescopes (MAST)[114] as the data set identified by 10.17909/t9-ky1s-j932.

3.3. Propagating the Uncertainties

In principle, one can obtain 1σ uncertainties on each of the parameters in our model from the best-fit covariance matrix. However, given the 383 parameters, 143 of which are freely varying, this is computationally impractical. An alternative is to assume that parameter space can be approximated by a parabola near the best-fit minimum in χ^2. Using numerically calculated first and second derivatives, one can then extrapolate from the minimum changes in each parameter to achieve $\Delta\chi^2 = 1$, which corresponds to a 1σ uncertainty for a single interesting parameter (Bevington 1969). Unfortunately, owing to the high dimensionality of our parameter space and its poor sampling in our calculations, this method proved inadequate.

All of the main quantities of interest to be extracted from our models are the fluxes of individual features, either in emission or in absorption. We therefore calculate uncertainties for these quantities using the data and associated uncertainties in each original spectrum and scaling them in proportion to the quantities that we integrate from our models. To explain this quantitatively, first we define these quantities:

$f_{\mathrm{data},i}$ = flux in pixel i of the original spectrum,
$\sigma_{\mathrm{data},i}$ = 1σ uncertainty for pixel i in the original spectrum,

[114] http://archive.stsci.edu

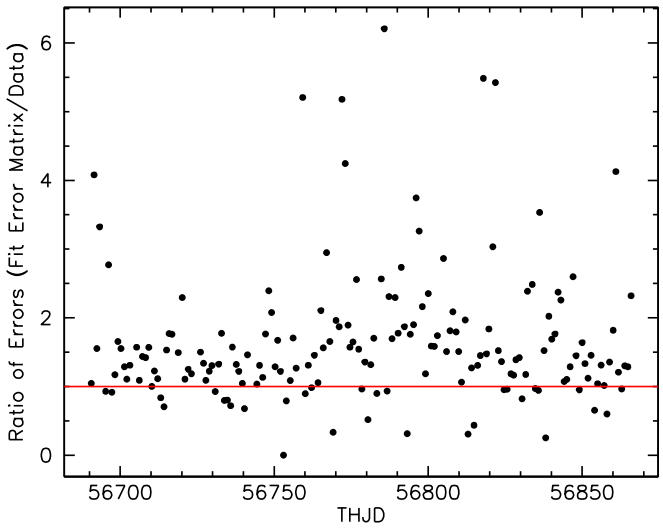

Figure 5. Comparison of uncertainties for the broad Lyα absorption feature in our model. Black points show the ratio of the uncertainty derived from the error matrix of the fit for $\Delta\chi^2 = 1$ divided by the 1σ uncertainty derived as described in Section 3.3. The ratio scatters about unity (red line), with large excursions.

$f_{\mathrm{mod},i}$ = flux in pixel i of the model spectrum,
$\sigma_{\mathrm{mod},i}$ = 1σ uncertainty for pixel i in the model spectrum,
$f_{c,j,i}$ = flux in pixel i of the component j (of 97 total), and
$\sigma_{c,j}$ = 1σ uncertainty for component j.

The flux of the model in pixel i can be decomposed into the sum of the contributions of the individual components:

$$f_{\mathrm{mod},i} = \sum_j f_{c,j,i}. \quad (1)$$

The variance of the model in pixel i is then

$$\sigma^2_{\mathrm{mod},i} = \sum_j \sigma^2_{c,j}. \quad (2)$$

In the limit of very good statistics, the variance predicted by the model should simply be the variance in the data themselves, i.e.,

$$\sigma^2_{\mathrm{mod},i} \sim \sigma^2_{\mathrm{data},i}, \quad (3)$$

so the variance in the total flux of any individual component is then

$$\sigma^2_{c,j} = \sum_i \sigma^2_{\mathrm{data},i} \times f^2_{\mathrm{mod},i} \Big/ \left(\sum_{k\neq j}\right) f^2_{c,k,i}. \quad (4)$$

If the quantity of interest is the sum of multiple components (i.e., the several components of an emission line contributing to the flux in a given velocity bin), then the 1σ uncertainty we derive for that quantity is

$$\sigma_{\mathrm{tot}} = \sqrt{\sum_j \sigma^2_{c,j}}. \quad (5)$$

Figure 5 shows the consequences of this method for calculating the 1σ uncertainties. When calculated directly from the data, as described above, the uncertainties are more uniform. The numerical instabilities in our method of interpolating in the error matrix of the fit give uncertainties that largely cluster around the calculation based on the data but show large excursions, both higher and lower.

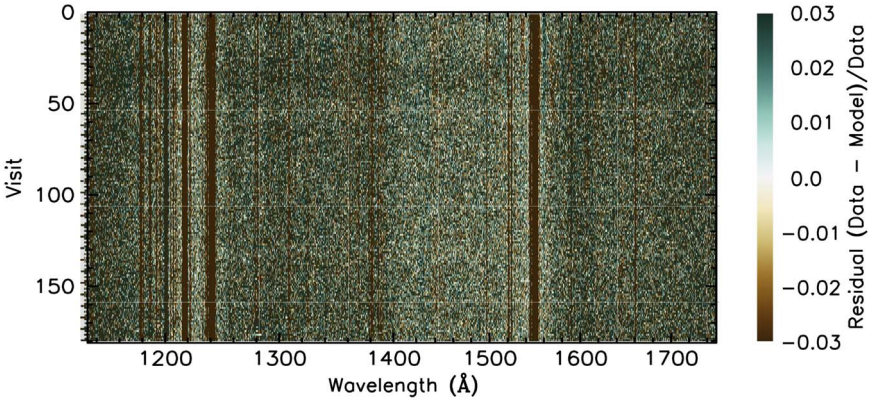

Figure 6. Normalized residuals from the best fit to each spectrum from the campaign. The horizontal axis is in pixels for each spectrum, spanning a wavelength range of 1130–1805 Å. The vertical axis is each individual visit in the campaign.

3.4. Quality Checking the Fits

The resulting best-fit χ^2 for each spectrum is shown as a time series in Figure 3. The number of points in each spectrum varies slightly, since the spectrum is moved to multiple positions on the detector using different central wavelength settings. Because of the differing central wavelength settings, not all spectra cover the same range in wavelength as the mean spectrum; the settings tend to lose several hundred points on the blue and red ends of each spectrum. On average, individual spectra have ∼11,600 points in each fit. With 143 freely varying parameters, given the χ^2 values ranging from ∼6800 to ∼9000 in Figure 3, one can see that our uncertainties are too large. This is most likely because in aligning and merging each spectrum, we have resampled the original pixels, introducing correlated errors in adjacent bins after rebinning. Note also that χ^2 varies systematically with time in the campaign, largely following the light curve of total brightness. A likely explanation for this trend is that it is easier to get a good fit to our complex model when the fluxes are lower and uncertainties are larger.

While the χ^2 shows that we have good fits overall, we visually examined each individual fit to see if there were any points or regions where there were systematic deviations of the model from the data. It was these inspections in our early experiments that led us to develop the fitting strategies we documented above. The final fits show no gross or systematic residuals. This is illustrated visually by the image in Figure 6 that shows the residuals of Data − Model for each fit stacked into a two-dimensional spectrogram. The only significant features visible are the vertical lines at the positions of interstellar and intrinsic narrow absorption lines, which are not part of our model.

Our final set of tests compared light curves of fluxes extracted from our model fits to integrations of the same regions of data used in De Rosa et al. (2015). Again, here we see no systematic deviations, but these figures do illustrate how the continuum regions are slightly contaminated by wings of the broad emission lines. Figure 7 compares light curves for continuum windows integrated from the raw data, as described by De Rosa et al. (2015), to integrations of the same wavelength regions in our models, both for the full model and for just the power-law continuum. The lower half of each panel in the figure shows the differences between the two curves along with uncertainties from the raw data. These uncertainties include the systematic repeatability errors described by De Rosa et al. (2015) that apply to the time-series analysis of fluxes from the campaign. These are $\delta_P = 1.1\%$ for data with $\lambda < 1425$ Å and $\delta_P = 1.4\%$ for $\lambda > 1425$ Å. One can see here that the cleanest continuum window, i.e., the one with the least contamination by surrounding emission lines, is the shortest-wavelength window surrounding 1158 Å. Although this is the cleanest window in terms of total flux, we use the modeled continuum flux at 1367 Å in our subsequent analysis. Since this is deterministically connected to the modeled flux at 1158 Å through the continuum model, there is no difference between using one or the other.

3.5. The Absorption-corrected Spectra

One of our main goals for these fits to the emission model of each spectrum is to correct for the effects of intrinsic broad absorption and also to bridge the regions affected by foreground interstellar absorption lines and the narrow intrinsic absorption features in NGC 5548 itself. To correct for the broad absorption, we simply apply the inverse of these model elements to the data. For each pixel corrected in this way, we apply the same scaling to the associated uncertainty, as well as the data themselves. To correct for the narrow absorption features (both foreground and intrinsic), since these are not modeled, we replace the data in the wavelength regions affected by the absorption with the emission model.

More specifically, we first visually examine the fit to the mean spectrum to identify points that were significantly affected by narrow absorption lines. These intervals and their identifications are listed in Table 2. Next, we define the following quantities:

$f_{\rm orig}$ = flux in the original spectrum,
$f_{\rm mod}$ = flux in the model spectrum (including broad absorption),
$f_{\rm abs}$ = model flux (negative) in the broad absorption lines,
$t_{\rm G}$ = transmission profile of Galactic damped Lyα, and
$f_{\rm cor}$ = flux in the corrected spectrum.

The corrected spectrum is then computed in two steps. First, we replace all pixels in the original spectrum with $f_{\rm cor}$ if they fall within the wavelength intervals defined in Table 2. We then compute $f_{\rm cor} = (f_{\rm orig} - f_{\rm abs})/t_{\rm G}$.

To calculate the 1σ uncertainties, we scale the original uncertainties in each pixel by the ratio of the corrected flux to the original flux:

$$\sigma_{\rm cor} = \sigma_{\rm orig} \times (f_{\rm cor}/f_{\rm orig}). \quad (6)$$

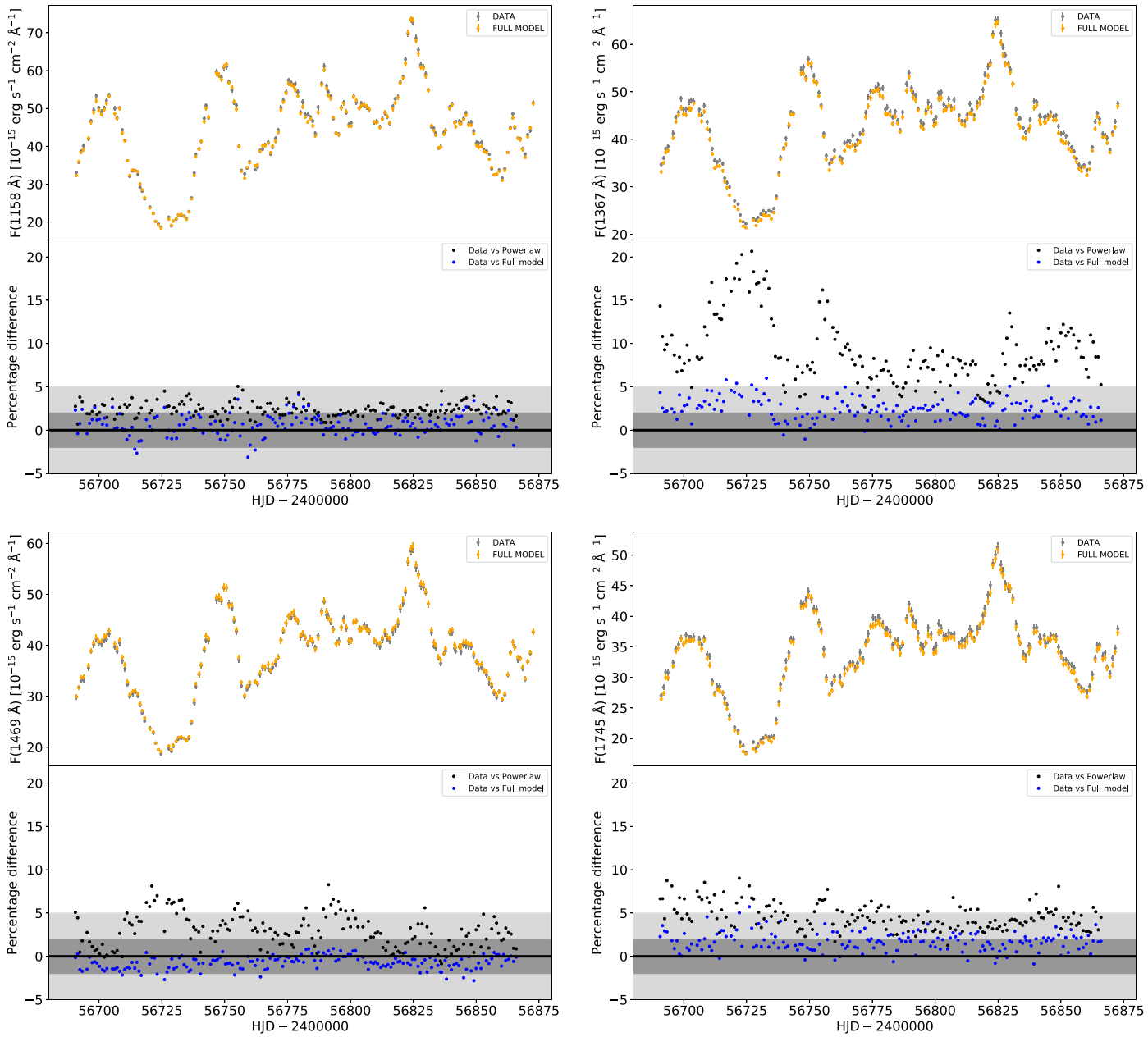

Figure 7. Comparisons of the continuum light curves integrated from the data (green points with error bars) to the fluxes integrated from our best-fit models (gold points with error bars). The top left panel shows the flux at 1158 Å, F(1158 Å), the top right panel F(1367 Å), the bottom left panel F(1469 Å), and the bottom right panel F(1745 Å). The dark gray region in each panel highlights ±2% errors, and the light gray region shows ±5% errors.

3.6. Fluxes in Deblended Emission Lines

With our model fits to the entire series of spectra from the STORM campaign, we can now extract absorption-corrected spectra for all emission lines across their full, deblended velocity profiles. Our models also allow us to separate the variable and nonvariable components of the strong emission lines, as well as deblend adjacent lines. For example, Crenshaw et al. (2009) were able to use the faint state of NGC 5548 in 2004 to separate and measure the narrow- and intermediate-line width components of the Lyα and C IV emission lines. They demonstrated that these components vary only slightly over timescales of years. Using our model, we are able to exclude these nonvarying components of the emission lines from the overall broad-line profile. Likewise, we can separate the contributions of blended lines from the wings of Lyα and C IV and measure lines such as N V as individual species.

For each individual broad emission line, we construct a model profile at each individual pixel i that includes only the contributions of the relevant broad-line components from our model. As described in Section 3.3, the net flux associated with a given emission feature is

$$f_{\mathrm{totem},i} = \sum_j f_{c,j,i}, \tag{7}$$

where the index j runs over all components associated with the desired emission feature. As described in Section 3.3, we calculate the associated 1σ statistical uncertainty as the fraction in quadrature (relative to all model components in that pixel) of

Table 2
Wavelength Intervals for Correcting Narrow Absorption Features in the NGC 5548 Spectra

Feature	λ_o (Å)	z	λ_1 (Å)	λ_2 (Å)
Blue end	1132.00	0.0	1124.00	1136.50
Fe III 1	1122.52	0.017175	1136.99	1137.60
Fe III* 1	1124.87	0.017175	1139.31	1140.01
P V 1	1126.72	0.017175	1140.98	1145.65
P II	1152.82	0.0	1152.28	1153.32
Si II ISM	1190.42	0.0	1189.53	1192.35
Si II ISM	1193.29	0.0	1192.61	1193.84
Unknown	1197.00	0.0	1196.56	1197.23
N I triplet	1200.00	0.0	1198.92	1201.16
S III 1	1190.20	0.017175	1205.50	1207.06
S III, Si I	1190.20	0.017175	1208.55	1210.61
Geocoronal Lyα	1215.67	0.0	1213.0	1219.0
Si II* 1	1197.39	0.017175	1212.95	1213.49
Unknown	1219.00	0.0	1218.79	1220.45
Si III 1	1206.50	0.017175	1221.76	1223.08
Si III 3 5	1206.50	0.017175	1224.20	1225.84
Unknown	1227.00	0.0	1227.34	1227.87
Unknown	1228.50	0.0	1228.46	1229.05
Lyα	1215.67	0.017175	1230.40	1236.85
N V Mg II	1238.82	0.0	1237.88	1240.50
N V ISM	1242.80	0.0	1242.23	1242.95
S II ISM	1250.58	0.0	1249.58	1250.81
S II ISM	1253.81	0.0	1253.21	1254.10
N Vb 1	1238.82	0.017175	1254.21	1256.37
N Vb 2	1238.82	0.017175	1256.50	1263.42
N Vr 5	1242.80	0.017175	1262.63	1263.56
N Vr 6	1242.80	0.017175	1263.62	1264.34
Si II 1	1260.42	0.017175	1276.64	1277.50
Si II* 1	1264.74	0.017175	1281.03	1282.20
O I ISM	1302.10	0.0	1300.71	1302.48
Si II ISM	1304.37	0.0	1303.13	1304.65
Si III* 1	1296.73	0.017175	1313.50	1314.06
Si III* 1	1298.96	0.017175	1315.66	1316.56
Ni II ISM	1317.22	0.0	1316.56	1317.30
Si III* 1	1303.32	0.017175	1320.15	1320.80
Si II 1	1304.37	0.017175	1321.10	1322.00
Si II* 1	1309.28	0.017175	1326.18	1327.14
Unknown	1326.53	0.0	1326.31	1326.83
C I ISM	1328.82	0.0	1328.22	1329.50
C II ISM	1334.53	0.0	1333.04	1336.18
C II 1	1334.53	0.017175	1351.56	1352.75
C II* 1	1335.71	0.017175	1352.75	1353.90
P III* 1	1344.33	0.017175	1361.31	1362.61
Ni II ISM	1370.13	0.0	1369.57	1370.39
Si IVb ISM	1393.76	0.0	1392.77	1394.17
Si IVr ISM	1402.77	0.0	1401.75	1403.20
Si IVb 1	1393.76	0.017175	1411.59	1412.80
Si IVb 3	1393.76	0.017175	1413.94	1417.11
Si IVr 1	1402.77	0.017175	1420.77	1422.14
Si IVr 3	1402.77	0.017175	1423.36	1426.35
Ni II ISM	1454.84	0.0	1454.31	1455.10
Si II ISM	1526.71	0.0	1525.80	1527.10
Si II 1	1526.71	0.017175	1546.53	1547.21
C IVb ISM	1548.19	0.0	1547.21	1548.76
C IVr ISM	1550.77	0.0	1549.71	1551.16
Si II* 1	1533.45	0.017175	1553.26	1554.18
C IVb 1	1548.19	0.017175	1567.02	1576.60
C IVr 6	1550.77	0.017175	1576.84	1577.51
Fe II ISM	1608.45	0.0	1607.54	1612.08
C I ISM	1656.93	0.0	1656.34	1657.13
Al II ISM	1670.79	0.0	1669.77	1671.74
Al II 1	1670.79	0.017175	1692.42	1693.15
Ni II ISM	1709.60	0.0	1708.38	1709.62
Ni II ISM	1741.55	0.0	1740.69	1741.72
Ni II ISM	1751.91	0.0	1750.84	1752.45

the 1σ uncertainty on the data in that pixel,

$$\sigma_{\mathrm{totem},i} = \sigma_i \sqrt{\frac{\sum_j f_{c,j,i}^2}{\sum_k f_{c,k,i}^2}}, \quad (8)$$

where the index j runs over all components contributing to the desired emission feature, and the index k runs over all components of the model contributing to the flux in pixel i. As described in detail by De Rosa et al. (2015), systematic repeatability errors affect the data when considering a time-series analysis of these quantities. We therefore add in quadrature the same errors in precision, namely, $\delta_P = 1.1\%$ for data from grating G130M ($\lambda < 1425$ Å) and $\delta_P = 1.4\%$ for data from grating G160M ($\lambda > 1425$ Å). These errors in reproducibility actually dominate the uncertainties for all quantities at $\lambda < 1180$ and $\lambda > 1425$ Å.

Figure 8 compares light curves for the modeled continuum flux at 1367 Å to the deblended broad emission lines of Lyα, N V, Si IV, C IV, and He II. Portions of these light curves are tabulated in Table 3, with full tabulations of these quantities and the other continuum windows (1158, 1430, and 1740 Å) available online. The light curves in Figure 8 closely resemble those derived from the original data shown in Figure 3 of De Rosa et al. (2015). In general, Lyα, Si IV, and C IV are brighter due to the corrections for absorption, the additional flux from the wings of the VB emission components, and the elimination of contaminating emission-line flux from the original continuum windows. For He II, the flux levels are roughly the same; additional flux from the VB component of the emission line and a less contaminated continuum are offset by subtraction of blended emission from C IV. Overall, the error bars are smaller, since the modeled flux for any given component is determined by many more pixels than the limited wavelength range used in the original integrations. The light curve for N V is a new addition enabled by the deblending from Lyα in our model. In some respects, N V differs in character from the other emission lines, especially during the first 75 days of the campaign prior to the BLR holiday. However, starting with the BLR holiday, its behavior is very similar to that of C IV and He II. We will quantify these similarities and differences in Section 4.1 when we discuss the emission-line lags.

3.7. Measuring the Absorption Lines

The intrinsic narrow absorption lines comprise six discrete velocity components. We adopt the nomenclature of Mathur et al. (1999), numbering each component in order starting at the highest blueshifted velocity. To illustrate this kinematic structure, Figure 9 shows normalized absorption profiles for the most prominent intrinsic absorption lines as a function of velocity relative to the systemic velocity of the host galaxy

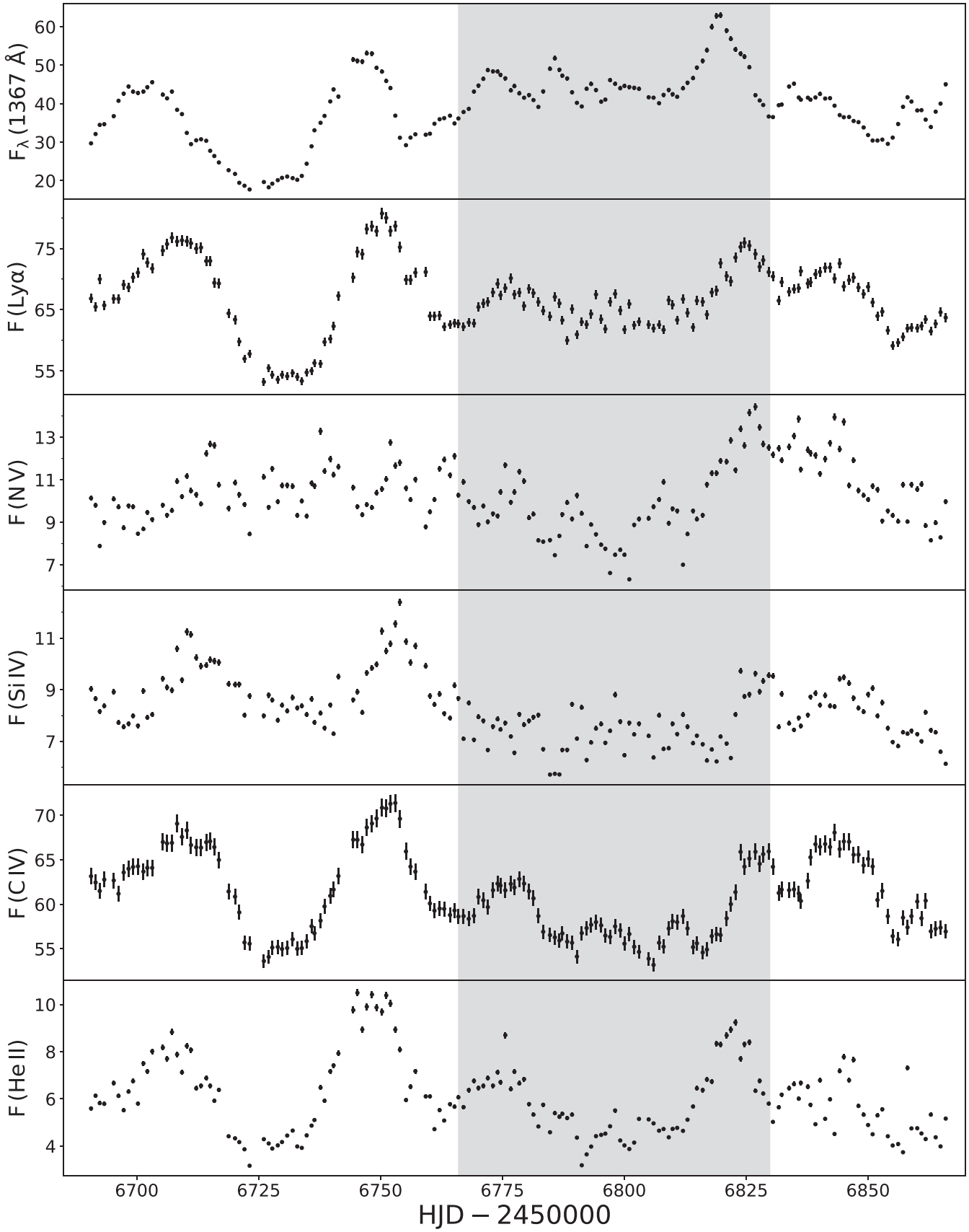

Figure 8. Light curve for the modeled continuum flux at 1367 Å (top panel) in units of 10^{-15} erg cm^{-2} s^{-1} Å^{-1} vs. HJD − 2,450,000. Subsequent panels show light curves for the integrated fluxes of the absorption-corrected deblended emission lines (as labeled) in units of 10^{-13} erg cm^{-2} s^{-1}. The shaded region shows the time interval of the BLR holiday.

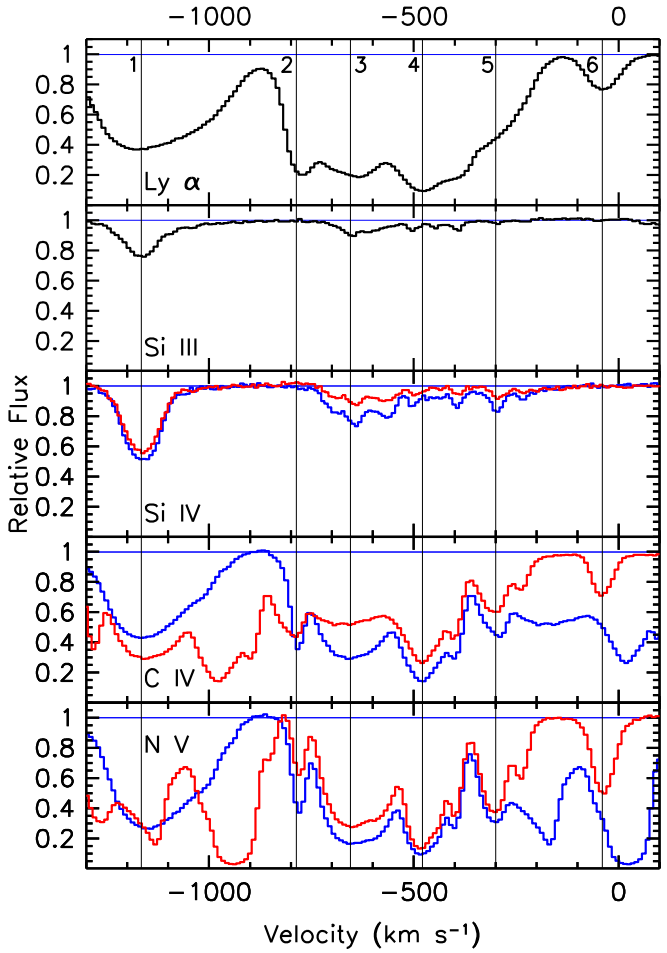

Figure 9. Intrinsic narrow absorption features in NGC 5548. Normalized relative fluxes are plotted as a function of velocity relative to the systemic redshift of $z = 0.017175$. The first panel shows Lyα, the second panel Si III λ1206, the third panel Si IV λ1393 (blue) and Si IV λ1402 (red), the fourth panel C IV λ1548 (blue) and C IV λ1550 (red), and the fifth panel N V λ1238 (blue) and N V λ1242 (red). Thin vertical lines indicate the velocities of the six intrinsic absorbers.

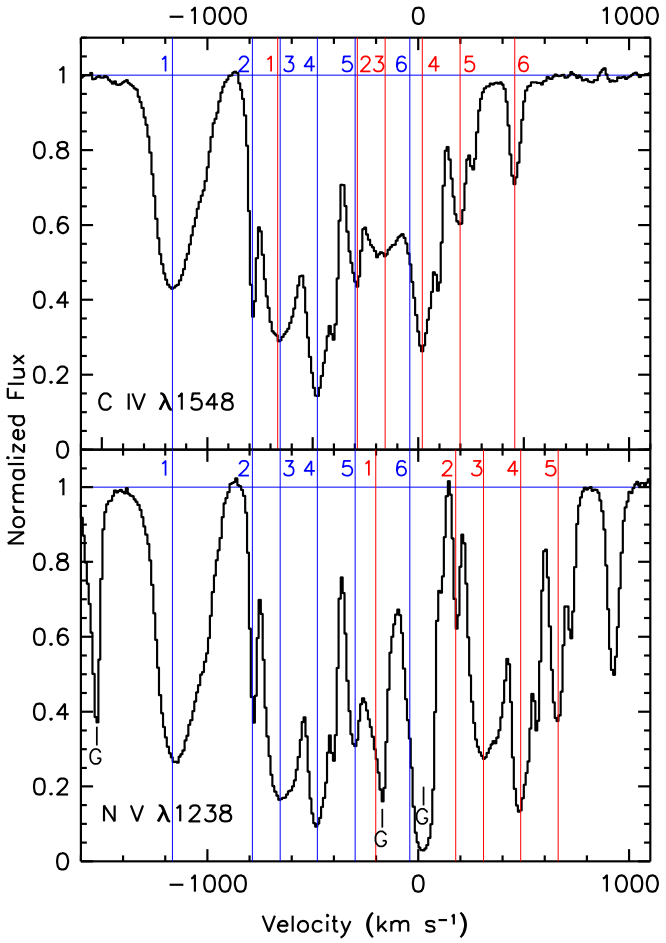

Figure 10. Illustration of blending in the absorption lines of the C IV and N V doublets in NGC 5548. Normalized relative fluxes are plotted as a function of velocity relative to the systemic redshift of $z = 0.017175$. The top panel shows C IV λ1548, and the bottom panel shows N V λ1238. Vertical blue lines indicate the velocities of the blue components of the doublets for the six intrinsic absorbers. Vertical red lines show the locations of the corresponding red components. Foreground Galactic interstellar absorption lines are marked with a "G."

NGC 5548. For this, we adopt the H I 21 cm redshift of $z = 0.017175$ (de Vaucouleurs et al. 1991).

Measuring the strengths of the intrinsic narrow absorption lines is straightforward. Using the complete model of each spectrum (including the broad absorption components, since they help define the local continuum surrounding the narrow intrinsic absorption lines), we measure the equivalent widths (EWs) by integrating across each absorption-line profile in the normalized spectrum. These integrations are performed as discrete sums over pixels lying within the wavelength regions defined for each feature in Table 4:

$$\mathrm{EW} = \sum_i (f_{\mathrm{orig},i} - f_{\mathrm{mod},i})/f_{\mathrm{mod},i} \times \Delta\lambda. \quad (9)$$

The 1σ uncertainty for EW is obtained by simply propagating the uncertainty associated with each data point in the original spectrum used in the sum:

$$\sigma_{\mathrm{EW}} = \sqrt{\sum_i (\sigma^2_{\mathrm{orig},i}/{f_{\mathrm{orig},i}}^2) \times \Delta\lambda^2}. \quad (10)$$

We use caution in performing these integrations to avoid features blended with Galactic absorption lines or other transitions. For example, the close velocity spacings of the C IV and N V doublets (498 and 964 km s^{-1}, respectively) cause components 1, 2, 3, and 5 in C IV to overlap and components 1 and 5 in N V to overlap, as shown in Figure 10. The red transition of component 1 in the N V doublet is blended with Galactic S II λ1259, and the blue transition of component 6 is blended with Si II λ1260. Therefore, Table 4 gives measurements only for clean, unblended features.

The EW of each broad absorption feature is calculated from the normalized modeled spectrum,

$$f_{\mathrm{norm},i} = f_{\mathrm{mod},i}/(f_{\mathrm{mod},i} - f_{\mathrm{abs},i}), \quad (11)$$

as

$$\mathrm{EW} = \sum_i (1 - f_{\mathrm{norm},i}) \times (\lambda_{i+1} - \lambda_i), \quad (12)$$

where λ_i is the wavelength of pixel i. Since our spectra are linearized, $\Delta\lambda = \lambda_{i+1} - \lambda_i$ is actually a constant. The

Table 3
Modeled Continuum and Deblended Emission-line Light Curves for NGC 5548

HJD[a]	F_λ(1367 Å)[b]	F(Lyα)[c]	F(N V)[c]	F(Si IV)[c]	F(C IV)[c]	F(He II)[c]
56,690.6120	29.71 ± 0.34	66.83 ± 0.76	10.14 ± 0.12	9.03 ± 0.10	63.16 ± 0.90	5.60 ± 0.08
56,691.5416	32.13 ± 0.36	65.48 ± 0.73	9.80 ± 0.11	8.66 ± 0.10	62.46 ± 0.88	6.13 ± 0.09
56,692.3940	34.50 ± 0.39	69.99 ± 0.78	7.89 ± 0.09	8.16 ± 0.09	61.50 ± 0.87	5.82 ± 0.08
56,693.3237	34.69 ± 0.39	65.72 ± 0.73	9.00 ± 0.11	8.37 ± 0.09	62.78 ± 0.88	5.79 ± 0.08
56,695.2701	36.78 ± 0.41	66.80 ± 0.74	10.09 ± 0.11	8.92 ± 0.10	62.69 ± 0.89	6.67 ± 0.10
56,696.2459	40.76 ± 0.46	66.78 ± 0.74	9.72 ± 0.11	7.73 ± 0.09	61.19 ± 0.87	6.12 ± 0.09
56,697.3080	42.63 ± 0.48	69.09 ± 0.77	8.74 ± 0.11	7.56 ± 0.08	63.59 ± 0.89	5.52 ± 0.08
56,698.3041	44.49 ± 0.50	68.66 ± 0.76	9.78 ± 0.11	7.69 ± 0.09	64.00 ± 0.90	6.30 ± 0.09
56,699.2338	43.14 ± 0.48	70.28 ± 0.78	9.73 ± 0.11	7.99 ± 0.09	64.20 ± 0.91	6.75 ± 0.10
56,700.2299	42.82 ± 0.48	71.07 ± 0.79	8.47 ± 0.10	7.61 ± 0.09	64.28 ± 0.91	5.80 ± 0.08

Notes. Modeled light curves are in the observed frame. Flux uncertainties include both statistical and systematic errors.
[a] Midpoint of the observation (HJD − 2,400,000).
[b] Units of 10^{-15} erg s^{-1} cm^{-2} Å^{-1}.
[c] Units of 10^{-13} erg s^{-1} cm^{-2}.

(This table is available in its entirety in machine-readable form.)

Table 4
Properties of Narrow Intrinsic Absorption Lines in NGC 5548

Feature	λ_0[a] (Å)	λ_1[b] (Å)	λ_2[c] (Å)	EW[d] (km s^{-1})	v[e] (Å)	c_f[f]	log N_{ion}[g] (cm^{-2})
P Vb 1	1117.98	1132.30	1133.05	−0.167 ± 0.015	−1207	1.00	$13.57^{+0.42}_{-0.20}$
Fe III 1	1122.52	1136.99	1137.60	−0.037 ± 0.004	−1205	1.00	$13.63^{+0.30}_{-0.27}$
Fe III* 1	1124.87	1139.31	1140.01	−0.031 ± 0.004	−1199	1.00	$13.73^{+0.20}_{-0.38}$
P Vr 1[h]	1126.72	1142.49	1143.33	−0.200 ± 0.004	−828	1.00	$13.57^{+0.42}_{-0.20}$
C III* 1	1175.26	1190.54	1190.98	−0.122 ± 0.002	−1195	0.65	$13.86^{+0.17}_{-0.24}$
C III* 1	1175.71	1190.98	1191.59	−0.183 ± 0.002	−1189	0.65	$14.23^{+0.29}_{-0.28}$
C III* 1	1176.37	1191.59	1192.35	−0.130 ± 0.002	−1190	0.65	$14.49^{+0.17}_{-0.24}$
S III 1[i]	1190.20	1205.50	1207.06	−0.571 ± 0.003	−1093	0.65	$14.37^{+0.10}_{-0.38}$
Si II 1	1193.29	1208.55	1209.38	−0.023 ± 0.002	−1196	0.34	$12.99^{+0.25}_{-0.49}$
S III* 1	1194.06	1209.53	1210.05	−0.030 ± 0.002	−1187	0.34	$14.37^{+0.32}_{-0.27}$
Si II* 1	1194.50	1210.05	1210.61	−0.034 ± 0.002	−1194	0.34	$13.25^{+0.25}_{-0.25}$
Si II* 1	1197.39	1212.95	1213.49	−0.026 ± 0.003	−1166	0.34	$13.00^{+0.25}_{-1.0}$
Si III 1	1206.50	1221.76	1223.08	−0.124 ± 0.003	−1176	0.30	$13.45^{+0.06}_{-0.62}$
Si III 3	1206.50	1224.20	1225.07	−0.048 ± 0.002	−638	0.30	$12.91^{+0.09}_{-0.61}$
Si III 5	1206.50	1225.07	1225.84	−0.028 ± 0.002	−454	0.30	$12.67^{+0.15}_{-0.61}$
Lyα 1	1215.67	0.017175	1232.98	−0.845 ± 0.002	−1156	0.70	>14.60
Lyα 2	1215.67	0.017175	1233.54	−0.301 ± 0.001	−785	0.90	>14.07
Lyα 3	1215.67	0.017175	1234.21	−0.515 ± 0.001	−659	0.90	>14.37
Lyα 4	1215.67	0.017175	1235.19	−0.791 ± 0.001	−470	0.95	>14.56
Lyα 5	1215.67	0.017175	1236.10	−0.182 ± 0.002	−299	0.70	>13.97
Lyα 6	1215.67	0.017175	1236.73	−0.105 ± 0.002	−22	0.70	$13.00^{+0.3}_{-1.0}$
N Vb 1	1238.82	1254.21	1256.46	−0.776 ± 0.003	−1147	0.80	>14.94
N Vb 2	1238.82	1256.46	1256.95	−0.115 ± 0.001	−791	0.70	>14.14
N Vb 3	1238.82	1256.95	1257.82	−0.637 ± 0.001	−648	0.90	>14.87
N Vb 4	1238.82	1257.82	1258.57	−0.555 ± 0.001	−478	0.95	>14.78
N Vr 2	1242.80	1260.70	1260.98	−0.051 ± 0.001	−789	0.70	>13.93
N Vr 3	1242.80	1260.98	1261.88	−0.536 ± 0.001	−645	0.90	>14.98
N Vr 4	1242.80	1261.88	1262.63	−0.482 ± 0.001	−475	0.95	>14.96
N Vr 5	1242.80	1262.63	1263.56	−0.230 ± 0.002	−302	0.70	>14.74
N Vr 6	1242.80	1263.67	1264.34	−0.095 ± 0.002	−35	0.70	>14.25
Si II 1	1260.42	1276.54	1277.50	−0.046 ± 0.003	−1193	0.28	$13.07^{+0.17}_{-0.57}$
Si II* 1	1264.74	1280.93	1282.20	−0.062 ± 0.003	−1166	0.28	$13.08^{+0.45}_{-0.58}$
Si III* 1	1296.73	1313.40	1314.60	−0.001 ± 0.004	−1600	0.90	$13.00^{+0.3}_{-1.0}$
Si III* 1	1298.96	1315.66	1316.56	−0.026 ± 0.003	−1185	0.90	$13.00^{+0.30}_{-1.0}$
Si III* 1	1303.32	1320.15	1320.80	−0.008 ± 0.003	−1195	0.90	$12.70^{+0.30}_{-0.7}$
Si II 1	1304.37	1321.10	1322.00	−0.015 ± 0.003	−1175	0.92	$13.09^{+0.15}_{-0.59}$
Si II* 1	1309.28	1326.18	1327.14	−0.020 ± 0.003	−1179	0.92	$13.09^{+0.15}_{-0.59}$
C II 1	1334.53	1351.56	1352.75	−0.078 ± 0.003	−1185	1.00	$13.61^{+0.38}_{-0.11}$

Table 4
(Continued)

Feature	λ_0[a] (Å)	λ_1[b] (Å)	λ_2[c] (Å)	EW[d] (km s^{-1})	v[e] (Å)	c_f[f]	log N_{ion}[g] (cm^{-2})
C II* 1	1335.71	1352.75	1353.90	−0.100 ± 0.003	−1194	1.00	$13.61^{+0.38}_{-0.11}$
P III* 1	1344.33	1361.31	1362.61	−0.009 ± 0.004	−1270	1.00	$13.20^{+0.76}_{-0.21}$
Si IVb 1	1393.76	1411.59	1412.93	−0.260 ± 0.003	−1181	0.50	$14.11^{+0.11}_{-0.06}$
Si IVb 3	1393.76	1413.78	1415.20	−0.178 ± 0.003	−644	1.00	$13.32^{+0.05}_{-0.05}$
Si IVb 4	1393.76	1415.20	1416.04	−0.071 ± 0.003	−455	1.00	$12.90^{+0.10}_{-0.09}$
Si IVb 5	1393.76	1416.04	1416.47	−0.040 ± 0.002	−305	1.00	$12.66^{+0.07}_{-0.07}$
Si IVb 6	1393.76	1416.47	1416.89	−0.021 ± 0.002	−228	1.00	$12.37^{+0.11}_{-0.15}$
Si IVr 1	1402.77	1420.68	1422.05	−0.210 ± 0.003	−1179	0.50	$14.18^{+0.04}_{-0.13}$
Si IVr 3	1402.77	1423.22	1424.39	−0.069 ± 0.003	−631	1.00	$13.18^{+0.11}_{-0.12}$
Si IVr 4	1402.77	1424.39	1425.24	−0.021 ± 0.003	−451	1.00	$12.67^{+0.20}_{-0.38}$
Si IVr 5	1402.77	1425.24	1425.67	−0.016 ± 0.002	−295	1.00	$12.54^{+0.15}_{-0.21}$
Si IVr 6	1402.77	1425.67	1426.09	−0.011 ± 0.002	−216	1.00	$12.38^{+0.20}_{-0.25}$
Si II 1	1526.71	1546.53	1547.21	−0.023 ± 0.003	−1190	0.70	$13.08^{+0.16}_{-0.58}$
Si II* 1	1533.45	1553.26	1554.18	−0.039 ± 0.003	−1193	0.70	$13.30^{+0.14}_{-0.16}$
C IVb 1	1548.19	1567.55	1570.26	−0.724 ± 0.004	−1162	0.70	>14.62
C IVb 2	1548.19	1570.26	1570.84	−0.169 ± 0.002	−793	0.70	>14.05
C IVb 4	1548.19	1571.87	1572.91	−0.704 ± 0.001	−478	0.95	>14.54
C IVr 4	1550.77	1574.40	1575.51	−0.551 ± 0.002	−478	0.95	>14.62
C IVr 5	1550.77	1575.51	1576.73	−0.131 ± 0.003	−322	0.50	>14.32
C IVr 6	1550.77	1576.84	1577.51	−0.005 ± 0.003	0	0.50	$12.50^{+0.5}_{-0.5}$

Notes.
[a] Rest wavelength.
[b] Starting wavelength for EW integration.
[c] Ending wavelength for EW integration.
[d] The EW of the absorption feature.
[e] Velocity of the feature relative to the systemic redshift of the host galaxy, $z = 0.017175$.
[f] Covering factor of the absorption feature.
[g] Column density of the absorption feature.
[h] Blended with Galactic Fe II λ1143.
[i] Blended with Galactic Si III λ1206.

corresponding 1σ uncertainty is

$$\sigma_{\rm EW} = (f_{\rm totabs}/{\rm EW}) \times \sigma_{\rm totabs}, \quad (13)$$

where $f_{\rm totabs}$ and $\sigma_{\rm totabs}$ are defined below.

The broad UV absorption troughs associated with the obscurer in NGC 5548 are shown in Figure 2 of Kaastra et al. (2014). These broad troughs are asymmetric, and they extend from near zero velocity in the systemic frame of the host galaxy to ∼−5500 km s^{-1}. The time-varying strengths of the intrinsic broad absorption lines in NGC 5548 that are associated with the obscurer are part of the models we have fit to all of the spectra. These all have one main component, but there are also weaker components on the high-velocity blue wing of the absorption profile. These individual weak components are often not well constrained by the model fits. We therefore calculate the total absorption, $f_{\rm totabs}$, for the sum of all components associated with a given spectral transition. The total flux is then

$$f_{\rm totabs} = \sum_j f_{c,j}, \quad (14)$$

where the index j runs over all components associated with the desired line, and the associated uncertainty is calculated as the quadrature sum of the 1σ uncertainties of each component j:

$$\sigma_{\rm totabs} = \sqrt{\sum_j \sigma^2_{c,j}}. \quad (15)$$

Table 5 shows sample portions of the light curves for the broad absorption in C IV and the intrinsic narrow absorption associated with C II λ1334. Full light curves for all features listed in Table 4 are published in the online version of this paper. Figure 11 shows sample light curves for the EWs of the narrow absorption features associated with component 1 for C II λ1334, Si III λ1206, and Si IV λ1393, plus component 3 for Si IV λ1393, all compared to the UV continuum flux at 1367 Å. Light curves for the broad absorption in C IV, N V, Lyα, and Si IV are shown in Figure 12.

4. Analyzing Results from the Models

4.1. Velocity-resolved Light Curves for Deblended Emission Lines

Our absorption-corrected, deblended emission-line profiles described in Section 3.6 allow us to remove the uncertainties in emission-line lags that may have been introduced by the

Table 5
Light Curves for Absorption Lines in NGC 5548

THJD[a] (day)	EW(Lyα broad) (Å)	EW(C IV broad) (Å)	EW(C II λ1334, 1) (Å)	EW(C IV λ1548, 1) (Å)
56,690.6120	3.978 ± 0.089	1.620 ± 0.055	−0.140 ± 0.035	−0.794 ± 0.016
56,691.5416	3.725 ± 0.087	1.460 ± 0.055	−0.105 ± 0.034	−0.757 ± 0.016
56,692.3940	3.744 ± 0.067	1.388 ± 0.053	−0.065 ± 0.033	−0.670 ± 0.016
56,693.3237	3.545 ± 0.068	1.397 ± 0.055	−0.101 ± 0.033	−0.760 ± 0.016
56,695.2701	3.490 ± 0.099	1.550 ± 0.054	−0.082 ± 0.031	−0.735 ± 0.015
56,696.2459	3.186 ± 0.061	1.153 ± 0.052	−0.027 ± 0.031	−0.680 ± 0.016
56,697.3080	3.559 ± 0.060	1.646 ± 0.053	−0.022 ± 0.030	−0.604 ± 0.016
56,698.3041	3.340 ± 0.058	1.179 ± 0.050	−0.014 ± 0.029	−0.624 ± 0.015
56,699.2338	3.369 ± 0.058	1.291 ± 0.050	−0.076 ± 0.029	−0.619 ± 0.015
56,700.2299	3.261 ± 0.058	1.061 ± 0.049	−0.039 ± 0.030	−0.701 ± 0.015

Note. Tabulated EWs are in the observed frame. Enumerations following the line designations in the column headings refer to the narrow absorption-line components as numbered in Figure 9.
[a] Midpoint of each observation (HJD − 2,400,000).
(This table is available in its entirety in machine-readable form.)

variable intrinsic absorption in NGC 5548, as well as to separate the behaviors of adjacent blended lines. In addition, for the brightest two lines, Lyα and C IV, we can determine velocity-binned lags for each line uncontaminated by absorption or blended contributions from other lines.

Following De Rosa et al. (2015), we measured the emission-line lags for the species tabulated in Table 3 by cross-correlating the time series with the continuum light curve using the interpolated cross-correlation function (ICCF) as implemented by Peterson et al. (2004). The procedure and resulting associated uncertainties are described in detail by De Rosa et al. (2015). Briefly, the technique uses a Monte Carlo method of "flux randomization and random subset selection" to generate a large set of realizations of the light curves. For each realization, we determine the cross-correlation function, its maximum correlation coefficient $r_{\rm max}$, and associated peak lag $\tau_{\rm peak}$. We also use the region surrounding the peak with $r(\tau) > 0.8$ to calculate the centroid of the cross-correlation function, $\tau_{\rm cent}$. A few thousand realizations of each cross-correlation function then gives distribution functions for $\tau_{\rm peak}$ and $\tau_{\rm cent}$ from which we measure the median values to give the lags for each emission line as presented in Table 6. The associated uncertainties represent the 68% confidence intervals of each Monte Carlo distribution.

While De Rosa et al. (2015) arbitrarily split the data set in two midway through the campaign, we now know that a more logical breaking point for examining any changes is at day 75 in the campaign, which is the beginning of the period when the broad emission-line fluxes become decorrelated from the continuum variations (Goad et al. 2016), also known as the BLR holiday. We therefore quote lags not only for the full campaign but also for the first 75 days, the preholiday period, when the emission-line and continuum fluxes correlated normally; for the holiday period, days 76–129; and for the postholiday period at the end of the campaign. Comparing the lags in Table 6 to De Rosa et al. (2015), we see that Lyα is slightly shorter, Si IV is longer, and C IV and He II are about the same. Within the error bars, the lags for the UV model data set are consistent with the prior results using the original data.

Comparing results for the different time intervals within the campaign reveals an interesting evolution in the emission-line lags. As expected, during the preholiday period, when the emission-line fluxes correlate well with the continuum

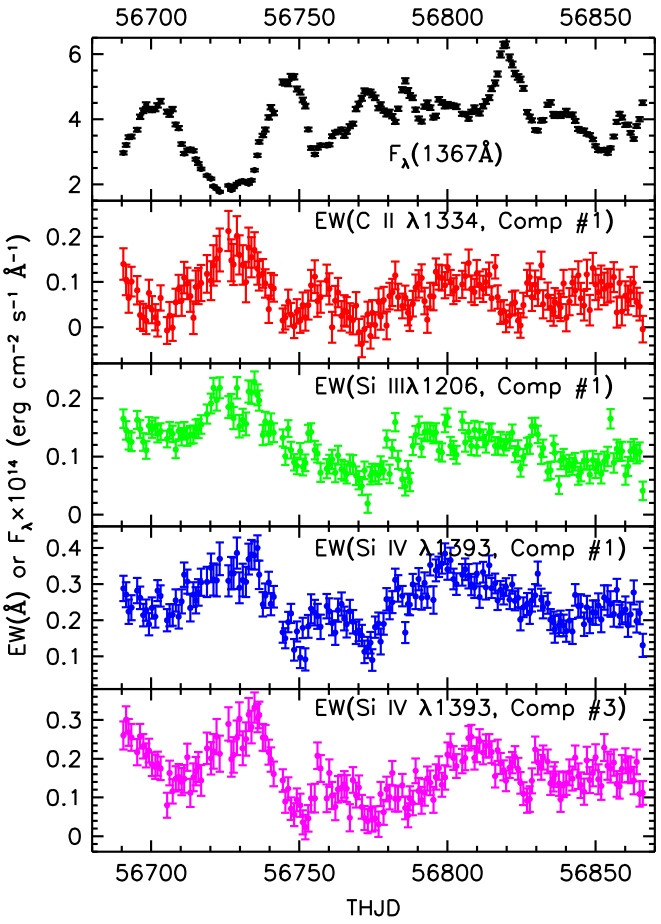

Figure 11. (First panel) Light curve for the UV continuum at 1367 Å in units of 10^{-14} erg cm^{-2} s^{-1} Å^{-1}. Lower panels show the absolute value of the EW in Å vs. time for selected absorption lines. (Second panel) C II λ1334, narrow absorption component 1. (Third panel) Si III λ1206, narrow absorption component 1. (Fourth panel) Si IV λ1393, narrow absorption component 1. (Fifth panel) Si IV λ1393, narrow absorption component 3.

fluctuations, correlation coefficients are high, exceeding $r = 0.9$ for Lyα, C IV, and He II. For N V, however, the correlation is so poor that we cannot determine a lag in the

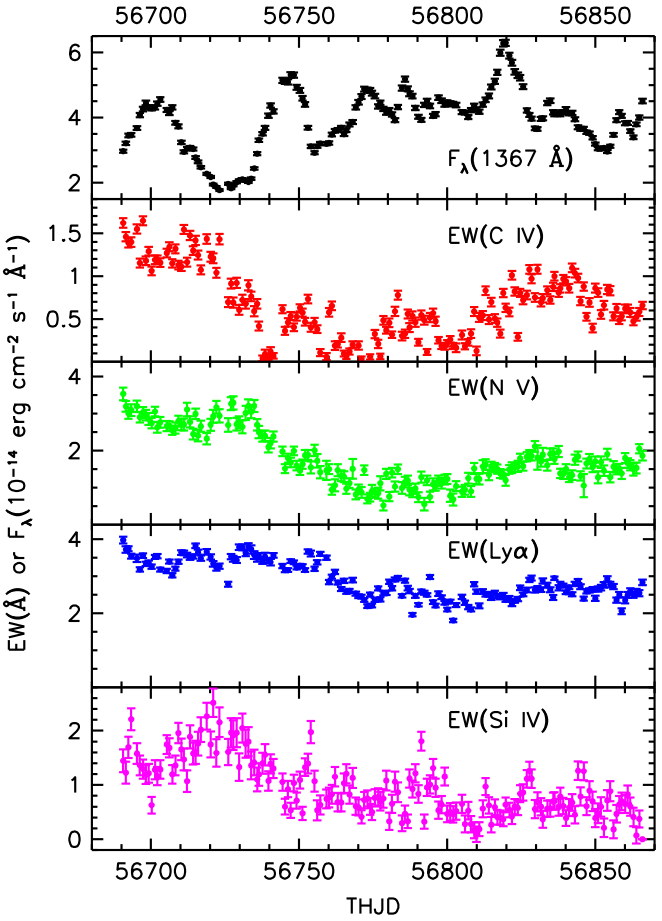

Figure 12. (First panel) Light curve for the UV continuum at 1367 Å in units of 10^{-14} erg cm^{-2} s^{-1} Å^{-1}. (Second panel) Absolute value of the EW in Å vs. time for the broad C IV absorption feature. (Third panel) Same as second panel, but for N V. (Fourth panel) Same as second panel, but for Lyα. (Fifth panel) Same as second panel, but for Si IV.

preholiday period, as expected from the lack of any strong features in this region of the light curve in Figure 8. During the holiday period, correlation coefficients are lower, but they are still very good, with $r > 0.65$ for all lines. Lags for all lines during the holiday are about the same as for the preholiday period, except for C IV. The C IV lag during the holiday is significantly longer than for the preholiday period by almost 3 days. In the postholiday period, correlation coefficients are again very good, and C IV shows significantly longer lags compared to the preholiday period. Other lines hint at such a difference, but not significantly. These changing lags with time explain why the correlation coefficients for the overall campaign are low despite the much longer data set. Together with changes in the velocity-resolved lags discussed below, this may indicate that significant changes in the structure (or at least our viewpoint), the illumination, or both of the BLR are occurring on the timescale of our campaign. Given that the orbital timescale at a radius of 1 lt-day in NGC 5548 is 115 days, such changes seem plausible.

To ensure that this apparent increase in the emission-line lags over the course of the campaign is not an artifact of our modeling of the data, we reanalyzed the original data of De Rosa et al. (2015) by splitting it into the same time intervals. The results are given in the bottom half of Table 6. The lags for the whole campaign replicate the original results of De Rosa et al. (2015), and we see the same lengthening of lags toward the end of the campaign with similar values to those found using the modeled data.

Also interesting are the velocity-binned results for Lyα and C IV. Absorption in NGC 5548 largely obscured the inner few thousand km s^{-1} of the blue side of the profile of each emission line, and N V or He II emission contaminated the far red wings. Following De Rosa et al. (2015), we use bins of 500 km s^{-1} spanning each profile. Figure 13 compares the mean spectrum for the modeled broad component of Lyα, its corresponding rms spectrum, and, finally, the velocity-binned profile to the original data from De Rosa et al. (2015). All data are for the full campaign. Our modeled profile provides full velocity coverage across the Lyα emission line. The most noticeable characteristic of the lag profile is its distinct "M" shape, with a local minimum in the lag near zero velocity and maxima on the red and blue sides at $\pm$2500 km s^{-1}. A prominent feature in the rms spectrum is the "red bump" on the Lyα emission-line profile at $+$1500 km s^{-1}, which loosely corresponds to the local peak in the velocity-dependent lag profile on the red wing of Lyα.

Figure 14 shows the corresponding set of results for the C IV emission line. For C IV, there are emission bumps on both the red and blue wings of the profile in the rms spectrum. These bumps are at higher velocity than the red bump in Lyα, at roughly $\pm$5000 km s^{-1}, and they appear to correspond to local minima in the lag profile, as opposed to the maxima seen in Lyα. As with Lyα, C IV shows a slight hint of an "M" shape to its profile, with a shorter lag near the center and local peaks at $\pm$2500 km s^{-1}. However, the contrast is not as distinctive as in Lyα. The central dip in C IV has a confidence level of only $\sim$90%.

Examining the velocity-binned profiles for the separate, distinct time intervals of the campaign reveals even more complex behavior. Figure 15 compares the rms spectra and velocity-dependent lags for C IV and Lyα from the full campaign to the first 75 days (the preholiday period), the period of the BLR holiday, and the postholiday period concluding the campaign. The emission bumps on the red and blue wings of C IV and the red wing of Lyα are most prominent early in the campaign and diminish in flux (or disappear, in the case of C IV red) by the end of the campaign. We show light curves for these features in Figure 16. The red emission bump in C IV also has associated features in the lag profiles that evolve from a local minimum on the red side of the bump during the preholiday period to a local maximum in the lag on the blue side of the bump. These more detailed changes in the emissivity and lag profiles again suggest that we are seeing changes in the structure of the BLR over the course of the campaign. This may be due to the presence of some outflowing components, as discussed in Section 5, but this is speculative and more easily investigated with two-dimensional reverberation maps and models.

4.2. Physical Characteristics of the Narrow and Broad Absorbers Based on the Mean Spectrum

The very high S/N of the mean spectrum makes accurate measures of weak features possible. These are particularly useful since they are often unsaturated and can therefore provide better diagnostic information on physical conditions in the absorbing gas. The last four columns of Table 4 give the EW, the velocity relative to the systemic velocity of the host

Table 6
Emission-line Lags from the Modeled NGC 5548 Spectra

Emission Line	Lyα	N V	Si IV	C IV	He II
Whole Campaign–Modeled Data					
τ_{cent}[a]	5.1 ± 0.3	7 ± 8	8.1 ± 0.7	5.8 ± 0.5	2.2 ± 0.3
τ_{peak}[b]	5.1 ± 0.6	6 ± 7	8.1 ± 1.0	5.7 ± 0.6	1.9 ± 0.4
r_{peak}[c]	0.71 ± 0.03	0.17 ± 0.06	0.16 ± 0.04	0.39 ± 0.04	0.56 ± 0.03
Pre-BLR Holiday, THJD = 56,691–56,765					
τ_{cent}[a]	4.8 ± 0.3	···	8.0 ± 0.5	4.4 ± 0.3	2.4 ± 0.4
τ_{peak}[b]	4.8 ± 0.4	···	8.1 ± 0.6	4.5 ± 0.5	2.2 ± 0.4
r_{peak}[c]	0.94 ± 0.01	···	0.7 ± 0.04	0.91 ± 0.02	0.91 ± 0.02
BLR Holiday, THJD = 56,766–56,829					
τ_{cent}[a]	5 ± 1	4.5 ± 0.4	7.3 ± 1	7.1 ± 0.6	2.1 ± 0.4
τ_{peak}[b]	5 ± 1	4.4 ± 0.6	7.3 ± 1	7.3 ± 0.7	2.1 ± 0.5
r_{peak}[c]	0.74 ± 0.06	0.79 ± 0.04	0.66 ± 0.06	0.73 ± 0.07	0.75 ± 0.05
Post-BLR Holiday, THJD = 56,830–56,866					
τ_{cent}[a]	6 ± 1	5 ± 3	10 ± 2	8 ± 1	7 ± 5
τ_{peak}[b]	7 ± 1	2^{+1}_{-4}	10 ± 3	8.5 ± 2.2	10^{+1}_{-8}
r_{peak}[c]	0.85 ± 0.04	0.72 ± 0.06	0.77 ± 0.19	0.80 ± 0.13	0.63 ± 0.09
Whole Campaign–Original Data					
τ_{cent}[a]	6.2 ± 0.3	···	5.3 ± 0.7	5.3 ± 0.5	2.5 ± 0.3
τ_{peak}[b]	6.1 ± 0.4	···	5.4 ± 1.1	5.2 ± 0.7	2.4 ± 0.6
r_{peak}[c]	0.77 ± 0.02	···	0.46 ± 0.06	0.36 ± 0.04	0.65 ± 0.03
Pre-BLR Holiday, THJD = 56,691–56,765					
τ_{cent}[a]	5.8 ± 0.3	···	5.2 ± 0.8	4.3 ± 0.3	2.4 ± 0.4
τ_{peak}[b]	5.9 ± 0.4	···	5 ± 1	4.4 ± 0.5	$1.4^{+0.9}_{-0.1}$
r_{peak}[c]	0.94 ± 0.01	···	0.7 ± 0.04	0.93 ± 0.02	0.90 ± 0.02
BLR Holiday, THJD = 56,766–56,829					
τ_{cent}[a]	5.2 ± 0.6	···	6 ± 2	6.9 ± 0.9	3.3 ± 0.6
τ_{peak}[b]	$5^{+1}_{-0.4}$	···	6 ± 2	7 ± 1	3.3 ± 0.8
r_{peak}[c]	0.84 ± 0.04	···	0.52 ± 0.09	0.64 ± 0.09	0.74 ± 0.06
Post-BLR Holiday, THJD = 56,830–56,866					
τ_{cent}[a]	7 ± 1	···	7 ± 1	8 ± 1	3 ± 1
τ_{peak}[b]	8 ± 2	···	7 ± 2	8 ± 2	3 ± 1
r_{peak}[c]	0.83 ± 0.08	···	0.75 ± 0.11	0.82 ± 0.12	0.81 ± 0.05

Notes. Delays measured in days in the rest frame of NGC 5548.
[a] Centroid of the ICCF lag distribution for $r > 0.8r_{peak}$.
[b] Peak lag.
[c] Peak correlation coefficient.

galaxy, the covering factor, and the inferred column density for the narrow absorption lines in the mean spectrum. For Galactic interstellar medium (ISM) features, the inferred column densities are at best lower limits, since the lines are saturated and the profiles have not been corrected for the COS line-spread function. For absorption lines intrinsic to NGC 5548, the line widths are broad enough (FWHM typically >80 km s^{-1}) that the COS line-spread function has little effect. To measure column densities, we integrate the apparent optical depth across the absorption-line profile between the wavelength limits given in Table 4, assuming a uniform covering factor, as given in the next-to-last column of the table (see Appendix A of Arav et al. 2015, for a description of the technique). For doublets and absorption lines with multiple transitions (e.g., P V or Si II), we can determine the covering factor such that integration of each line profile gives consistent column densities. For other absorption lines, particularly the deep, heavily blended features associated with Lyα, N V, and C IV, we use a covering factor determined by the deepest point of the absorption-line profile and assume the line is saturated. Like Arav et al. (2015), this gives a lower limit on the column density.

Examining the covering factors in Table 4 is instructive. Lines far from the centers of the bright emission lines (e.g., P V, Si II λ1302, C II λ1335) have covering factors near unity, indicating that the absorbing gas fully covers, or nearly fully covers, the continuum emission region. These absorption lines are also multiplets, so their covering factors are well

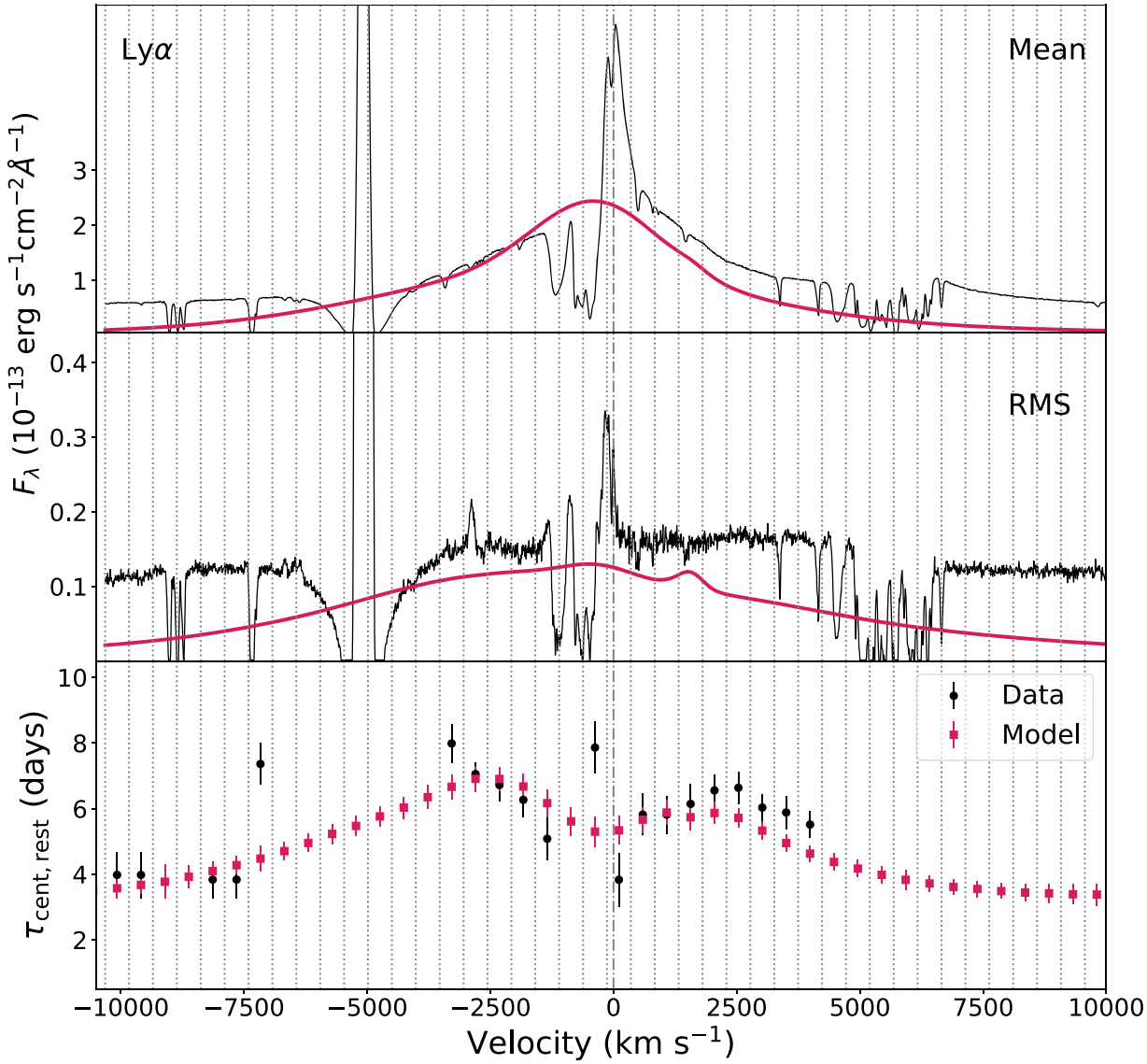

Figure 13. (Top panel) Comparison of the mean spectrum in the Lyα region of NGC 5548 (black data curve) to the best-fit model spectrum corrected for absorption with the continuum-subtracted and narrow and intermediate emission-line components removed (smooth red curve). (Middle panel) Same as top panel, but for the rms spectrum. (Bottom panel) We compare velocity-binned centroids from the ICCF across the Lyα profile obtained using the original data (black dots) to the absorption-corrected model with narrow and intermediate emission-line components removed (red squares). Lags are in the rest frame of NGC 5548.

determined. Other absorption lines embedded in the profiles of bright emission lines, such as C III* λ1176, Si II λ1193, and Si II λ1260, have well-determined covering factors that are significantly less than unity and vary depending on their distance from the center of the emission line. The sense of this variation is such that covering factors are lower for lines in the brighter portions of the emission-line profile. From this we conclude that, at least for component 1, the absorbing gas nearly fully covers the continuum-emitting region but only covers less than half of the BLR.

The column densities in Table 4 for the STORM campaign mean that the spectra are factors of several lower than those observed by Arav et al. (2015) during the *XMM-Newton* campaign. This is consistent with the higher brightness of NGC 5548 during the STORM campaign —$\langle F_{\lambda 1367}\rangle = 4.30 \times 10^{-14}$ erg cm^{-2} s^{-1} Å^{-1} versus $\langle F_{\lambda 1367}\rangle = 3.11 \times 10^{-14}$ erg cm^{-2} s^{-1} Å^{-1}. Simple scaling of the continuum would imply an increase in the ionization parameter of $\Delta \log U$ of 0.14. Although this seems small, it is sufficient to account for the observed differences, since the weak, low-ionization species in component 1 are formed in a thin hydrogen ionization front, and their column densities are highly nonlinear with changes in ionizing flux.

We tabulate the properties of the broad absorption features separately, since these are most likely associated with the soft X-ray obscurer discovered by Kaastra et al. (2014). To obtain the EW, mean transmission-weighted velocity, transmission-weighted velocity dispersion, and column density of each broad absorption trough, we use the normalized mean spectrum of NGC 5548. For each trough, we use the highest blueshifted velocity at which the trough drops by more than 1σ below the normalized spectrum. All troughs are integrated up to zero velocity. Since these broad troughs are well resolved, we use the apparent optical depth method of Savage & Sembach (1991) to calculate the column densities of each trough. The deepest absorption troughs in N V, Si IV, and C IV appear to be saturated, since they have similar depths at the velocities of the

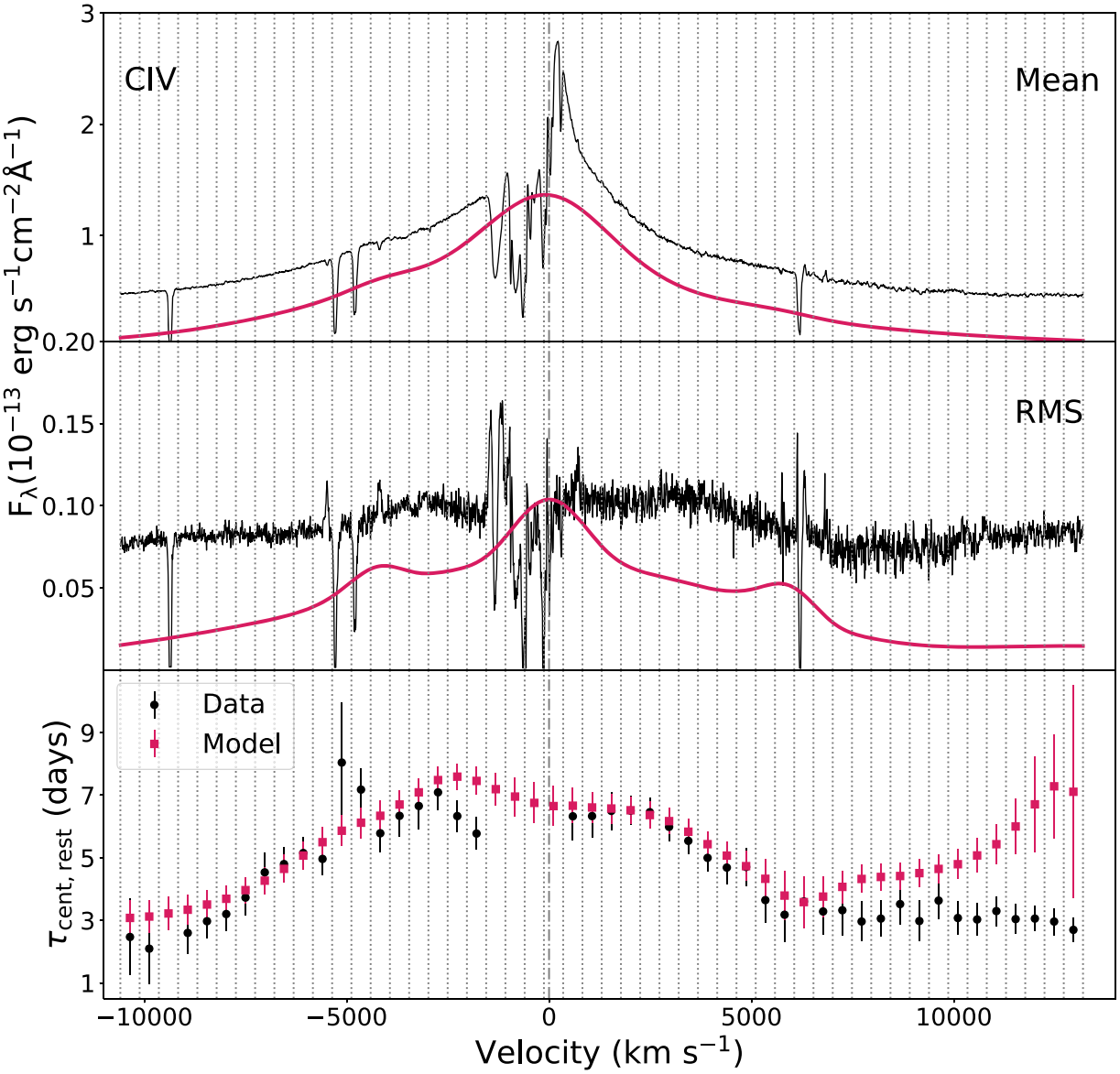

Figure 14. Same as Figure 13, but for C IV.

red and blue members of their respective doublets. Since Lyα is of similar depth, we also assume it is saturated. We therefore measure a covering factor C_f at the deepest point of the trough and use this in our apparent optical depth calculation (Arav et al. 2002). This column density is only a lower limit to the actual column density. The shallower absorption troughs are significantly less deep. If they were saturated and had similar covering factors, they would likely have similar depths to those of the stronger ions. We therefore assume that they lie on the linear portion of the curve of growth and use their apparent optical depths to obtain a direct measure of the column density assuming covering factors of unity. Table 7 summarizes the broad absorption trough properties in detail.

We can now use these measures of ionic column densities in the UV, together with the X-ray opacity measurements from the *XMM-Newton* spectra of Kaastra et al. (2014), to determine the ionization state of the obscurer more accurately. Because of the low X-ray flux resulting from the heavy X-ray absorption, the *XMM-Newton* spectra have no detectable spectral features that we can use to determine the ionization properties of the obscurer. However, the X-ray spectrum does provide a good measure of the total column density. As in the study of the obscurer in NGC 3783 (Kriss et al. 2019), we examine joint photoionization models that use the UV ionic column densities along with the total column density determined from the X-ray observations to more precisely determine the physical properties of the obscurer. Since the obscuring gas is illuminated by the bare active nucleus in NGC 5548, we use the unobscured SED shown in Figure 2 of Arav et al. (2015) for our photoionization models. Using Cloudy v17.00 (Ferland et al. 2017), we run a grid of models covering a range of −1.5 to 2.0 in ionization parameter log ξ and total column densities from log $N_H = 21.0$ to 23.5.[115] Figure 17

[115] The ionization parameter is defined as $\xi = L_{ion}/(n\,r^2)$, where L_{ion} (erg s^{-1}) is the ionizing luminosity obtained by integrating from 1 to 1000 Ryd, n is the density (cm^{-3}), and r (cm) is the distance of the obscurer from the AGN. We will also use the ionization parameter defined by $U = Q_H/(4\pi r^2 n_H c)$, where Q_H is the rate of incident ionizing photons above the Lyman limit, r is the distance to the absorbing gas from the nucleus, n_H is the total hydrogen number density, and c is the speed of light. For the SED of Arav et al. (2015), the conversion from ξ to U is log U=log ξ − 1.6.

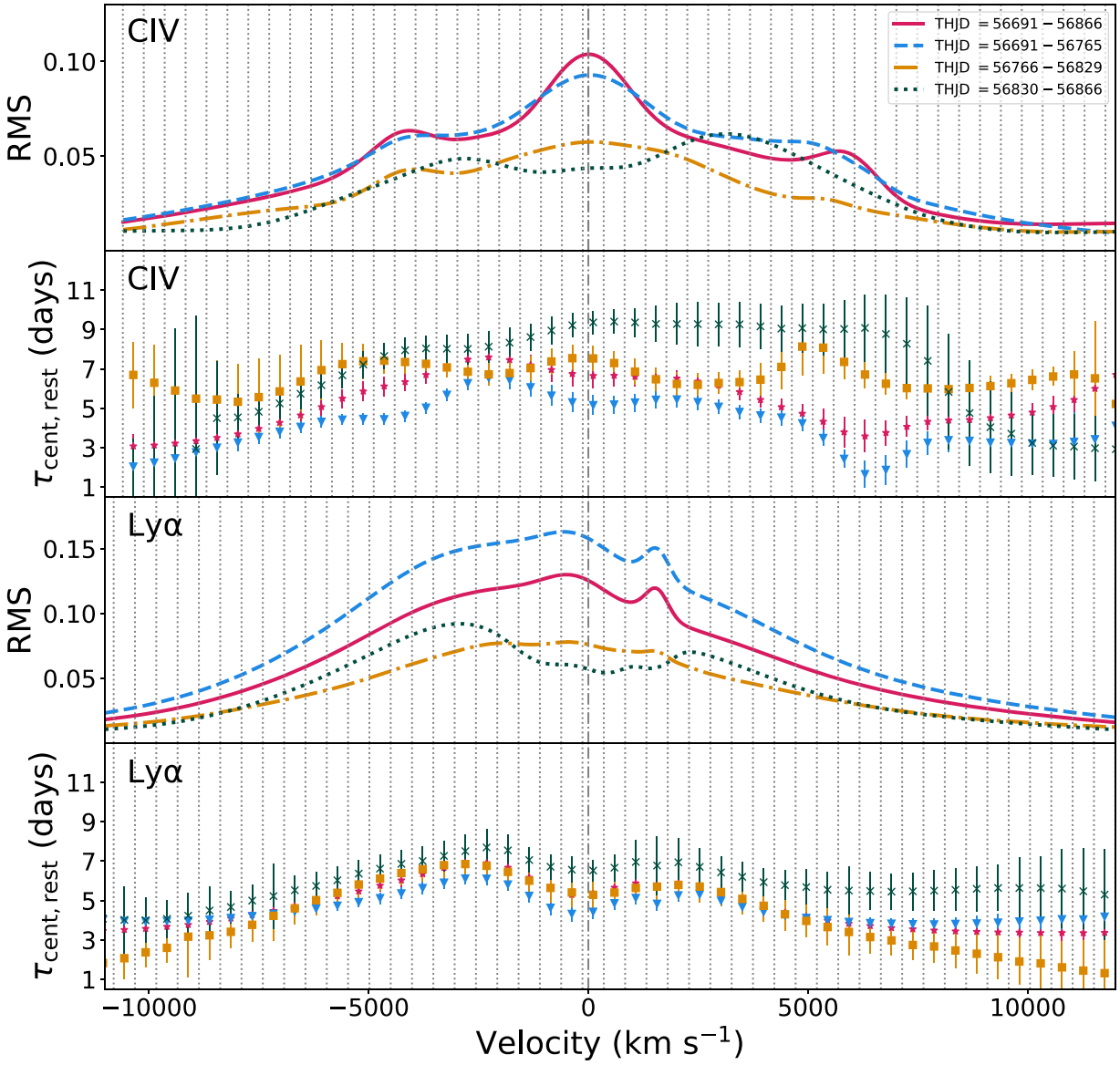

Figure 15. (First panel) Comparison of the rms spectra in the C IV emission-line region of NGC 5548 for four different time intervals. All curves refer to the modeled UV spectrum as corrected for absorption with the continuum-subtracted and narrow and intermediate emission-line components removed. The solid red curve is for the full campaign, THJD = 56,691–56,866. The dashed blue curve is for the first 75 days of the campaign, the preholiday period, THJD = 56,691–56,765. The dashed–dotted gold curve is for the period of the BLR holiday, THJD = 56,766–56,829. The dotted green curve is for the postholiday period, THJD = 56,830–56,866. (Second panel) We compare velocity-binned centroids from the ICCF across the absorption-corrected model for C IV with narrow and intermediate emission-line components removed. Lags are in the rest frame of NGC 5548. Red triangles show results for the full campaign, THJD = 56,691–56,860. Blue triangles are for the first 75 days of the campaign, the preholiday period, THJD = 56,691–56,765. Gold squares are for the period of the BLR holiday, THJD = 56,765–56,829. Green crosses are for the postholiday period, THJD = 56,830–56,866. (Third panel) Same as the first panel, but for the Lyα emission line. (Fourth panel) Same as the second panel, but for the Lyα emission line.

shows the allowed space of the photoionization solutions, which are at the two points where the X-ray column densities of the two obscurer components intersect the measured column densities of C II, C III*, Si II, and P V in the grid of photoionization models. Note that no single solution fits all measured ions, but some of this incommensurability could be due to the unknown covering fraction of the weak, low-ionization species. In addition, all of these low-ionization species are produced in very narrow ionization fronts, so there are likely systematic errors in the photoionization modeling (see Mehdipour et al. 2016a) that are larger than the statistical uncertainties we show in the figure. Kaastra et al. (2014) used only the *XMM-Newton* X-ray spectra to determine the ionization parameter and column density of the obscurer. Since there are no spectral features to constrain the X-ray models, a broad range of ionization parameters produces acceptable fits. As shown by Mehdipour et al. (2017), Kriss et al. (2019), and Longinotti et al. (2019), including the UV absorption as an additional constraint indicates that the obscuring gas likely has higher ionization, even in the observations of the original *XMM-Newton* campaign. From our new analysis that includes the broad UV absorption as part of the solution, we see that the obscurer is much more highly ionized than originally thought. Component 1, with log $N_{\rm H}$ cm^{-2} = 22.08, actually has an ionization parameter in the range log ξ_1 = 0.8–0.95, and component 2 is even more highly ionized at log ξ_2 = 1.5–1.6. These differ sufficiently from

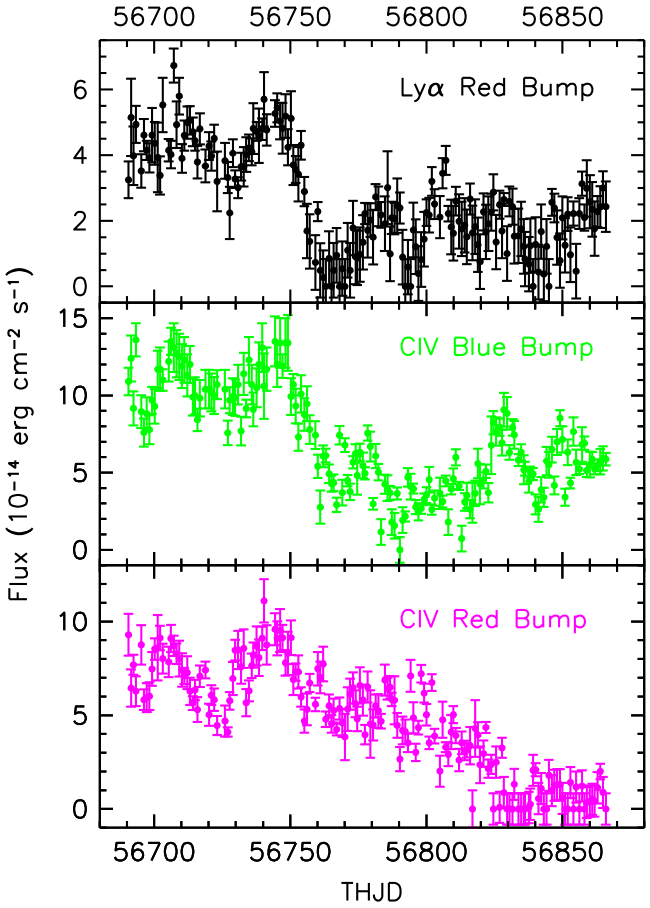

Figure 16. (Top panel) Light curve (black points with 1σ error bars) for the flux in the emission bump on the red wing of Lyα at $\sim$+1500 km s^{-1}. (Middle panel) Same but for the emission bump on the blue wing of C IV at $\sim$−4300 km s^{-1} (green). (Bottom panel) Same, but for the emission bump on the red wing of C IV at $\sim$+5700 km s^{-1} (magenta). Fluxes are in units of of 10^{-14} erg cm^{-2} s^{-1}.

the original fits of Kaastra et al. (2014; $\log \xi_1 = -0.8$ and $\log \xi_2 = -4.5$) that another look at the X-ray spectral analysis is warranted.

4.3. Variability of the Narrow Absorption Features

The narrow intrinsic absorption features in NGC 5548 lie at distances of $\sim$3 to hundreds of pc (Arav et al. 2015). They vary on timescales of days (as seen above in Figure 11) to years (Arav et al. 2015) and appear to be associated with the X-ray warm absorber in NGC 5548 (Mathur et al. 1995; Crenshaw et al. 2009; Kaastra et al. 2014; Arav et al. 2015). Using density-sensitive transitions in the metastable excited states of C III and Si III, Arav et al. (2015) determined the density of the gas producing the absorption features associated with component 1 as $\log n\ \mathrm{cm}^{-3} = 5.8 \pm 0.3$, placing it at a distance of 3.5 ± 1.0 pc, consistent with the density and the 1–3 pc location of the emission-line gas in the NLR (Peterson et al. 2013). Using the time variability of these absorption features, we can independently measure the density by measuring the recombination time in the gas. Krongold et al. (2007) used the variability of the aggregate soft X-ray absorption as it responded to continuum flux changes in NGC 4051 to estimate recombination times, but here we have the opportunity to make such measurements with distinct, resolved absorption lines in the UV.

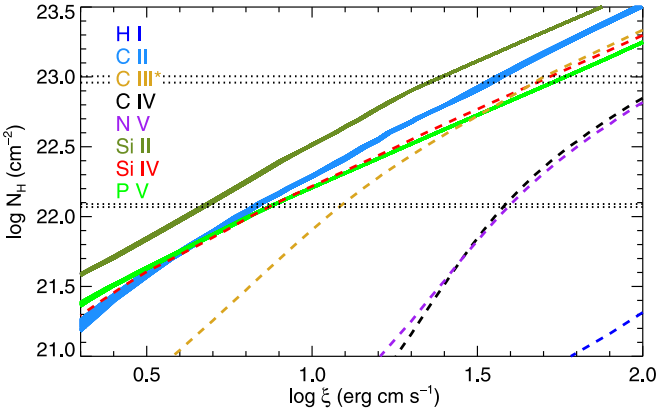

Figure 17. Photoionization model constraints on the obscurer in NGC 5548. Dotted black lines give the range of total column density for the two components of the obscurer (Kaastra et al. 2014). Thick colored bands show the column densities with associated 1σ uncertainties for the weak, low-ionization troughs in the mean UV spectrum of NGC 5548. Nominally, photoionization solutions should lie along these lines. For the strong, saturated features, we use dashed colored lines for the lower limits on their column densities. Allowed photoionization solutions lie above these lines.

For gas in photoionization equilibrium, the population density n_i in a state i depends on the balance between the ionizing photon flux causing ionizations to more highly ionized states and recombinations from those states. Following Krolik & Kriss (1995), this can be expressed as

$$dn_i/dt = -(F_{\mathrm{ion},i}\sigma_{\mathrm{ion},i} + n_e\alpha_{\mathrm{rec},i-1})n_i + n_e n_{i+1}\alpha_{\mathrm{rec},i} + F_{\mathrm{ion},i-1}\sigma_{\mathrm{ion},i-1}n_{i-1}. \quad (16)$$

For the ions we are measuring, generally, $n_{i-1} \ll n_i \ll n_{i+1}$, so we can simplify to

$$dn_i/dt = -F_{\mathrm{ion},i}\sigma_{\mathrm{ion},i}n_i + n_e n_{i+1}\alpha_{\mathrm{rec},i}. \quad (17)$$

In general, as long as there is a copious increase in the ionizing flux, the $-F_{\mathrm{ion},i}\sigma_{\mathrm{ion},i}n_i$ term dominates, and ions n_i are destroyed instantly. Conversely, when the flux decreases abruptly, $n_e n_{i+1}\alpha_{\mathrm{rec},i}$ dominates, and n_i reappears more slowly, on the recombination timescale

$$\tau_{\mathrm{rec}} = (n_i/n_{i+1})/(n_e\alpha_{\mathrm{rec},i}). \quad (18)$$

Figure 18 beautifully illustrates this simple behavior. We can see the absolute magnitude of the EW of the C II λ1334 absorption features decrease in absolute value immediately when the continuum flux increases. Conversely, when the continuum flux decreases, there is a noticeable delay in the C II response as it takes a measurable amount of time for recombinations to repopulate the C II ionization state.

Our high data quality and good sampling enable us to measure recombination delays directly from our light curves. To obtain an objective, empirical measure of the recombination time, we cross-correlated the continuum light curve with the absorption-line light curves (using the ICCF of Peterson et al. 2004) but restricted our cross-correlation to time intervals when the continuum flux had reached a peak and then fell to a minimum. We obtained good cross-correlations only for a select number of absorption lines in components 1 and 3. We tabulate the measured recombination times in Table 8. To convert these times into densities, we use Cloudy 17.00 (Ferland et al. 2017) to obtain the recombination rates for each of the ions in Table 8, assuming a fiducial density of $\log n = 4.8$ cm^{-3}. The

Table 7
Properties of the Broad Absorption Troughs in the NGC 5548 Mean Spectrum

Line	λ_0[a] (Å)	v_1[b] (km s^{-1})	v_2[c] (km s^{-1})	v_o[d] (km s^{-1})	σ_v[e] (km s^{-1})	EW[f] (Å)	log($N_{\rm ion}$)[g] (cm^{-2})	C_f[h]
P V	1122.99	−1388	0	−751	726	0.07 ± 0.04	13.11 ± 0.03	1.0
C III*	1175.8	−5323	0	−1250	1054	0.06 ± 0.01	12.72 ± 0.07	1.0
Lyα	1215.67	−6344	0	−1931	1160	2.95 ± 0.02	>14.80	0.25
N V	1240.51	−4907	0	−1697	1054	1.70 ± 0.02	>14.81	0.17
Si II	1260.42	−7894	0	−4592	986	0.09 ± 0.01	12.80 ± 0.05	1.0
C II	1334.53	−2067	0	−953	439	0.04 ± 0.01	12.96 ± 0.09	1.0
Si IV	1398.27	−4913	0	−1878	1005	0.84 ± 0.02	>13.83	0.06
C IV	1549.48	−4627	0	−1893	1091	0.63 ± 0.01	>14.02	0.07

Notes.
[a] Rest wavelength. For doublets, the quoted wavelength is the average.
[b] Starting velocity of the absorption trough.
[c] Ending velocity of the absorption trough.
[d] Transmission-weighted velocity centroid of the absorption trough.
[e] Transmission-weighted velocity dispersion of the absorption trough.
[f] The EW of the absorption trough.
[g] Inferred ionic column density assuming the trough is saturated.
[h] Covering factor at the deepest point in the absorption trough.

Table 8
Recombination Timescales and Densities in NGC 5548 Absorption Components

Feature	$\tau_{\rm rec}$ (days)	log n_e (cm^{-3})
C II λ1334 1	2.84 ± 0.69	5.92 ± 0.4
Si III λ1206 1	8.12 ± 0.95	4.99 ± 0.1
Si IV λ1393 1	3.81 ± 0.71	5.70 ± 0.3
Si III λ1206 3	5.83 ± 0.77	5.13 ± 0.1
Si IV λ1393 3	5.54 ± 0.71	5.53 ± 0.1

best-fit photoionization solutions from Arav et al. (2015) give log $U = -1.5$ and log $N_{\rm H} = 21.5$ cm^{-2} for component 1 and log $U = -1.3$ and log $N_{\rm H} = 21.2$ cm^{-2} for component 3. We scale up the ionization parameters by the ratio of the continuum fluxes at 1367 Å for the mean spectrum from the *XMM-Newton* campaign (3.11×10^{-14} erg cm^{-2} s^{-1} Å^{-1}) to the value from the mean spectrum of the STORM campaign (4.30×10^{-14} erg cm^{-2} s^{-1} Å^{-1}). The `print ionization rates` command in Cloudy then gives total recombination rates for the relevant ionic states, and we scale the fiducial density of log $n = 4.8$ cm^{-3} by the ratio of the inferred recombination time from Cloudy to our measurements in Table 8 to obtain the tabulated inferred densities.

These density measurements are reassuring both for their internal consistency and for their agreement with the independent determination of log $n_e = 4.8 \pm 0.3$ obtained by Arav et al. (2015) using density-sensitive absorption-line ratios. Despite our simplifying assumptions, it is gratifying that the atomic physics of this gas produces such consistent results. C. Silva et al. (2019, in preparation) discussed the limitations of our simplifying assumptions in more detail and produced a more rigorous time-dependent photoionization model of the various light curves that verify these empirical results with greater precision.

This classic ionization response describes the light curves of the low-ionization transitions visible in component 1. However,

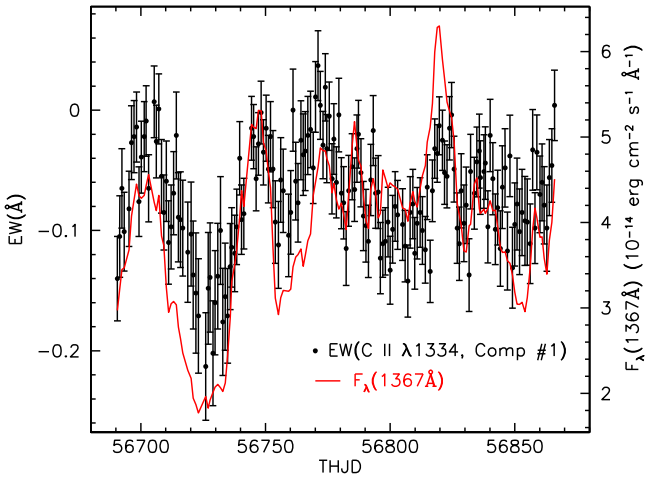

Figure 18. The UV continuum light curve at 1367 Å (red line) overlaid on the variations in EWs for the absorption in C II λ1334 (black points) associated with the intrinsic narrow absorption component 1 in NGC 5548.

this idealized behavior only holds true for approximately the first third of the campaign. At later times, the absorption lines do not follow the continuum so closely, during either the ionization or recombination phases. The correlation plot comparing EW(C II) to the UV continuum flux F_λ(1367 Å) in Figure 19 shows a good linear correlation (linear correlation coefficient $r = 0.82$) for the first 75 days of the campaign, or THJD < 56,766, but much more scatter at later times ($r = 0.39$).

A partial explanation for the inconsistent correlation of the absorption-line strength with the observed UV continuum is that the observed continuum is only one determinant of the actual ionizing flux beyond the Lyman limit. Historically, the extreme UV (EUV) continuum varies with greater amplitude than the FUV (Marshall et al. 1997). We also know that the soft X-ray continuum is obscured by optically thick gas that only partially covers the continuum source (Kaastra et al. 2014). This opaque partial coverage also shadows the ionizing UV, as

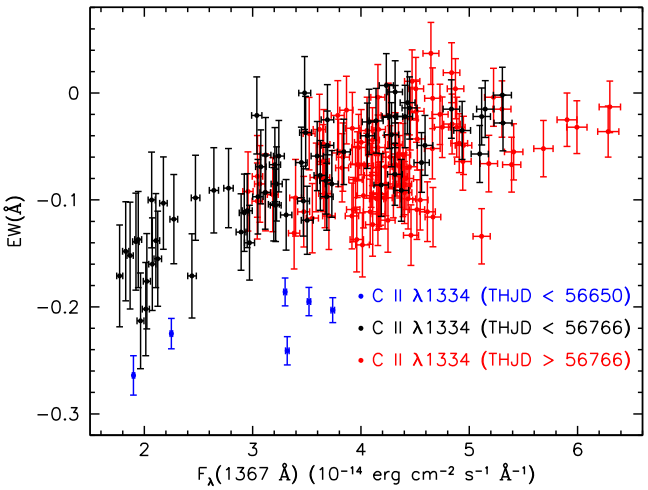

Figure 19. Correlation of the EW of the absorption line C II λ1334 associated with the intrinsic narrow absorption component 1 in NGC 5548 with the UV continuum flux at 1367 Å. Blue points are for the six observations of the *XMM-Newton* campaign, all prior to THJD = 56,650; black points are for dates in the STORM campaign earlier than THJD = 56,766; and red points are for later times.

shown by the photoionization analysis of the UV absorption lines (Arav et al. 2015). The obscuration is also variable, with the variability predominantly explained by variations in the covering fraction (Di Gesu et al. 2015; Cappi et al. 2016; Mehdipour et al. 2016b). If the covering fraction of the obscurer is varying, then one would expect variations in the ionizing flux that are independent of the strength of the observed UV continuum. To test this hypothesis, we did a joint correlation analysis of the variations in EW(C II) with the UV continuum and the hardness ratio (HR) as measured with *Swift*. The HR is defined as HR = (HX − SX)/(HX + SX), where SX is the soft X-ray count rate in the 0.3–0.8 keV band, and HX is the count rate in the hard X-ray band, 0.8–10.0 keV (Edelson et al. 2015). The HR is almost a direct measure of the covering fraction of the obscurer (Mehdipour et al. 2016b). A linear fit of the EW(C II) to the UV continuum flux, F_λ(1367 Å), yields the red line shown in Figure 20, with $\chi^2 = 224.2$ for 171 points and 2 degrees of freedom. This is a good correlation, but the fit is not a statistically acceptable predictor of the strength of the EW(C II). If we include the HR as an additional independent variable, the goodness of fit improves dramatically to $\chi^2 = 156.1$, which is statistically acceptable. This strongly bolsters the interpretation that the ionizing continuum for C II is determined by both the observed intensity of the UV continuum and the fraction of the ionizing continuum that is covered by the X-ray obscurer.

The bottom panel of Figure 20 shows how including HR as a predictor of the EW(C II) improves the fit. The red line is the prediction based solely on the UV continuum flux. The observed EWs have a large scatter about this line, as seen by the black points. When the HR for each observation is taken into account, the predicted EWs then vary from the simple linear fit in a manner consistent with variations in the covering fraction. For a given UV flux, high HRs, indicative of high covering fractions, mean that more of the ionizing continuum is obscured, so predicted EWs are greater in magnitude (more negative). For low HRs, covering fractions are lower, more ionizing flux leaks past the obscurer, and EWs decrease in magnitude as more C II is ionized.

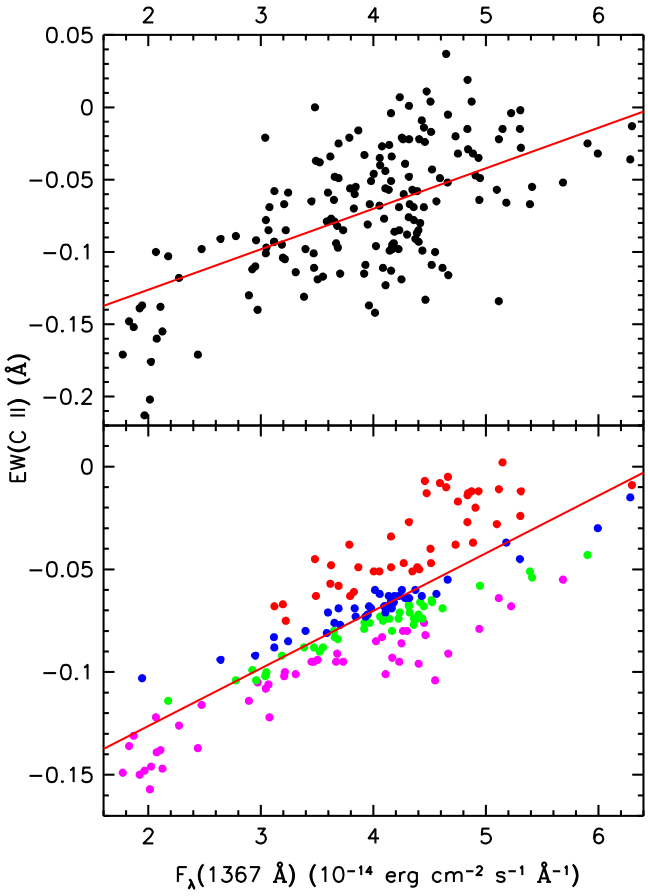

Figure 20. Fits to the correlation of the EW of the absorption line C II λ1334 associated with the intrinsic narrow absorption component 1 in NGC 5548 with the UV continuum flux at 1367 Å. The top panel shows EW(C II) (black points) for the entire STORM campaign. The solid red line shows the best-fit linear correlation of EW(C II) with the UV continuum flux, F_λ(1367 Å). (Bottom panel) Colored points show predicted EWs at a given UV flux for a joint correlation with the *Swift* HR. Red points have HR < 0.768, blue points have 0.768 ⩽ HR < 0.81, green points have 0.81 ⩽ HR < 0.845, and magenta points have HR ⩾ 0.845.

An alternative possibility is that the shape of the ionizing continuum is varying, and that the soft X-ray flux might be a good measure of this when combined with the UV continuum flux. We therefore tested a joint correlation of the EW(C II) with the UV continuum flux and the soft X-ray count rate, SX. This also gives an improved fit, $\chi^2 = 180.7$, which is statistically acceptable but not as good as the fit using HR. The improvement can readily be explained as a consequence of SX being determined partially by intrinsic flux variations but mostly by variations in the covering fraction of the obscurer, as argued by Mehdipour et al. (2016b).

The lack of a direct, exclusive correlation with the observed UV continuum flux is even more striking for all of the high-ionization absorption lines, Si IV, C IV, and N V. Figure 21 illustrates these effects in the blue component of C IV λ1548 associated with the absorbing gas in component 1. This transition has the highest blueshift of any narrow intrinsic absorption feature for C IV, and therefore it is not blended with any other components. In Figure 21, one can see that it tracks the UV continuum variations very closely up to THJD = 56,766 during both increases in flux and decreases in flux. For the first 75 days of the STORM campaign, before the BLR holiday, C IV has a linear correlation coefficient of

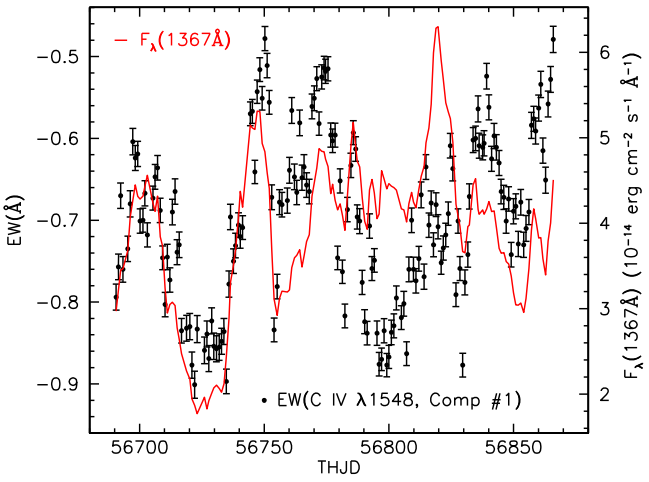

Figure 21. UV continuum light curve at 1367 Å (red line) overlaid on the variations in EW for the absorption in C IV λ1548 (black points) associated with the intrinsic narrow absorption component 1 in NGC 5548.

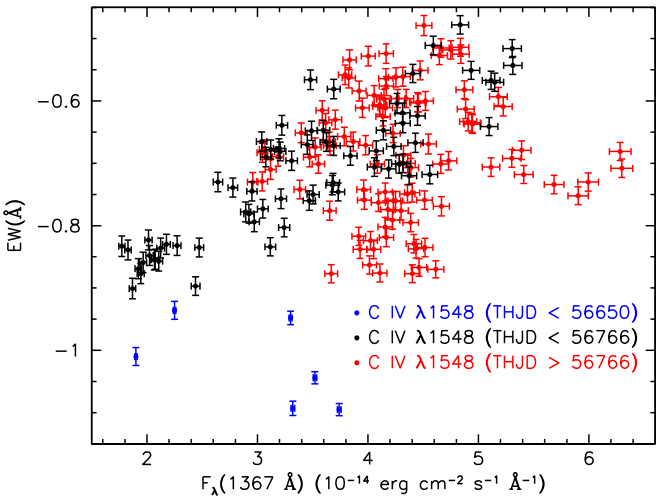

Figure 22. Correlation of the EW of the absorption line C IV λ1548 associated with the intrinsic narrow absorption component 1 in NGC 5548 with the UV continuum flux at 1367 Å. Blue points are for the six observations of the *XMM-Newton* campaign, all prior to THJD = 56,650; black points are for dates in the STORM campaign earlier than THJD = 56,766; and red points are for later times.

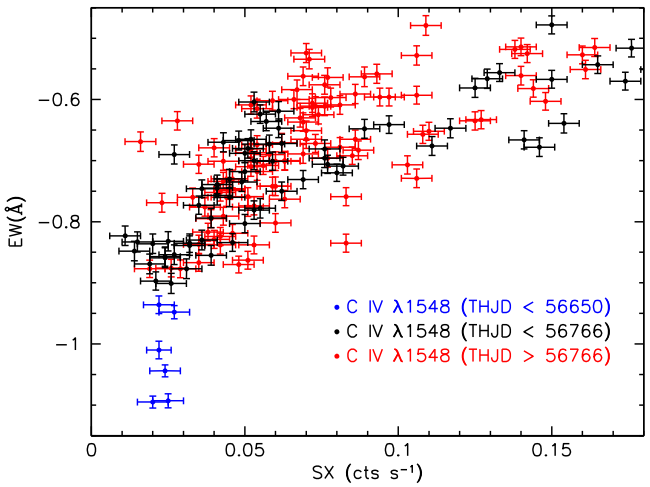

Figure 23. Correlation of the EW of the absorption line C IV λ1548 associated with the intrinsic narrow absorption component 1 in NGC 5548 with the *Swift* SX. Blue points are for the six observations of the *XMM-Newton* campaign, all prior to THJD = 56,650; black points are for dates in the STORM campaign earlier than THJD = 56,766; and red points are for later times.

$r = 0.86$. For the remainder of the campaign, however, the correlation drops significantly, with $r = 0.06$. In contrast to C II, C IV does not show any recombination delay when continuum flux levels fall, even during the first 75 days of the campaign; the absorption increases in strength almost immediately when the flux levels rise (for THJD < 56,766). The other high-ionization ions, Si IV and N V, also show this instantaneous response. At later times, however, C IV becomes almost completely decorrelated. The correlation plot comparing the EW(C IV) to the UV continuum flux F_λ(1367 Å) in Figure 22 shows a tight correlation with the UV continuum during the first 75 days, just like for C II, but a large degree of scatter at later times. During the period of the BLR holiday, after THJD = 56,776, there is no coherent correlation between EW(C IV) and the UV continuum flux. The particularly discordant points in the upper right corner of Figure 22 correspond to the FUV continuum flux peak near the end of the holiday period at THJD = 56,820.

As for C II, we investigated whether other variables might also have a strong correlation with the ionizing flux that is controlling the population of C IV ions. In Figure 23, we compare EW(C IV) to the soft X-ray flux as measured by *Swift* (Edelson et al. 2015). Although not perfect, the correlation improves significantly, suggesting that the soft X-ray flux plays a more dominant role in controlling the C IV ionic population than the FUV continuum.

Again, we investigated whether a multivariate correlation would be better than either continuum measure on its own. First, as expected, a simple linear fit of EW(C IV) versus F_λ(1367 Å) is statistically unacceptable with $\chi^2 = 6271$ for 171 points and two free parameters. We then included the HR in the correlation, leading to a dramatic improvement, but the fit is still poor with $\chi^2 = 4314$. Finally, in contrast to C II, using the soft X-ray flux in tandem with F_λ(1367 Å) gives the best result, $\chi^2 = 3608$. This is still statistically unacceptable, but it does show the stronger influence that the soft X-ray continuum is having on the C IV ionization than the FUV continuum. As a final trial, assuming that the HR might serve as an additional measure of the covering fraction of the obscurer, we carried out a trivariate analysis using SX, F_λ(1367 Å), and HR. This provided no additional improvement in χ^2, with $\Delta\chi^2 < 1$. Figure 24 shows the correlation of the EW(C IV) with F_λ(1367 Å) and how including SX as an additional independent variable improves the fit. Much of the scatter about the linear fit is explained by variations in the soft X-ray flux. The low EW points in the upper right corner of the top panel of Figure 24 coincide with some of the lowest soft X-ray fluxes observed, as shown in the bimodal fit presented in the bottom panel. The fact that it is the soft X-ray flux directly rather than just a covering factor effect (as for C II) may be telling us that the EUV and soft X-ray continuum shape is also varying, since it is this portion of the continuum that is responsible for ionizing C IV. This is not the whole story, however. As shown in Figure 24, there is a large set of points (shown in green) where variations in the EW(C IV) are not explained by either UV or soft X-ray continuum variations. These green points encompass times from THJD = 56,776 to

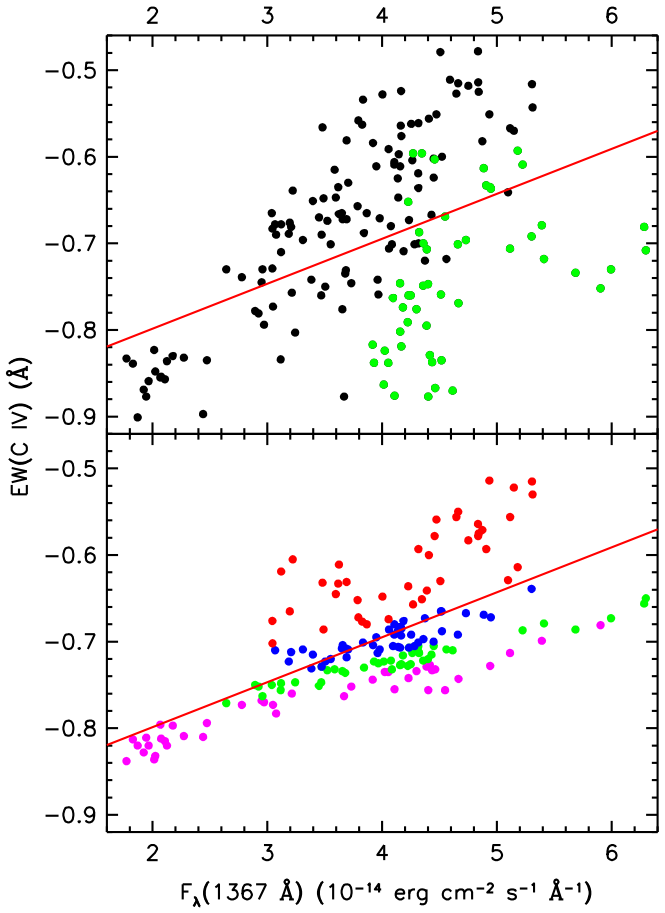

Figure 24. Fits to the correlation of the EW of the absorption line C IV λ1548 associated with the intrinsic narrow absorption component 1 in NGC 5548 with the UV continuum flux at 1367 Å. (Top panel) Black and green points are for the entire STORM campaign. Green points show values for EW(C IV) during the depths of the BLR holiday, for times 56,776 < THJD < 56,827. The red line shows the best-fit linear correlation of EW(C IV) with the UV continuum flux, F_λ(1367 Å). (Bottom panel) Colored points show predicted EWs at a given UV flux for a joint correlation with the *Swift* soft X-ray flux from 0.3 to 0.8 keV, SX. Red points have SX > 0.085, blue points have 0.085 ⩾ SX > 0.058, green points have 0.058 ⩾ SX < 0.043, and magenta points have SX < 0.043.

56,827. This evidence, plus the complete decoupling from the continuum variations in the light curve after THJD ∼ 56,750, appears to be related to the BLR holiday (Goad et al. 2016), which sets in at the same time. The green points in Figure 24 lie in the deepest portion of the BLR holiday. In Paper VII (Mathur et al. 2017), we speculated that the BLR holiday was related to changes in the EUV/soft X-ray continuum shape, and that these changes in the higher-energy range of the SED were not reflected in the visible FUV continuum. The responses of the high-ionization intrinsic absorption lines enable us to directly measure these changes in the SED.

While the responses of the broad emission lines also give insight into the behavior of the continuum, their large-scale spatial distribution and differing views of the continuum source complicate such an analysis. Since the narrow intrinsic absorption lines in NGC 5548 are directly along our line of sight, they are exposed to the same continuum that we see. This allows us to take advantage of their unique point of view and to obtain a direct measure of the continuum strength at a variety of energies. To a good first approximation, the continuum flux at an ion's ionization potential is the ionizing flux driving the population of that ion. To use the strength of the absorption lines as a measure of this flux, however, we must be certain that the absorption-line variations are reflecting changes in column density in response to changes in the ionizing flux, rather than being caused by variations in covering factor, transverse motion, or both.

The best evidence in favor of a dominant photoionization response is the good correlation we see between the strength of the individual absorption lines and either the FUV continuum (for low-ionization lines like C II) or the soft X-ray flux (for high-ionization lines like C IV). Our biggest concern is for C IV, because it was heavily saturated during the *XMM-Newton* campaign. The photoionization models of Arav et al. (2015) show that it has an optical depth of 200 during the observations in 2014. Figure 25 shows that the bottom of the absorption trough in C IV λ1548 component 1 remained relatively constant in 2014, in agreement with heavy saturation. Likewise, Figure 23 shows that during the *XMM-Newton* campaign, the strength of the absorption in C IV λ1548 component 1 is independent of the soft X-ray flux and much stronger than during the AGN STORM campaign. In contrast, Figure 23 shows a strong correlation with the soft X-ray flux during the AGN STORM campaign, indicative of a photoionization response. In Figure 26, we show that the absorption-line profiles change as expected if the column density in C IV component 1 was varying in response to changes in the ionizing flux.

Assuming that the absorption lines in component 1 are indeed tracing a response to change in the ionizing flux, we can use this behavior as a diagnostic of the ionizing continuum. For the first 75 days of the campaign (dates prior to THJD = 56,766), both the absorption lines and the emission lines show a good correlation in their variations with the FUV continuum flux at 1367 Å. We use this proportionality to derive a linear relationship between a line's EW and the continuum flux of

$$\mathrm{EW} = a_0 + a_1 \times F_\lambda(1367). \tag{19}$$

During this early part of the campaign, when everything correlates well, we assume that the continuum shape is that shown in Figure 4 of Mehdipour et al. (2015). We designate points lying on this fiducial SED as $F_0(\lambda)$, where λ may be either the observed wavelength 1367 Å or the wavelength at the ionization potential of the relevant ion, $\lambda_{\rm IP}$. We can then use variations in the EW of a given line to measure changes in the flux at the ionization potential relative to this fiducial SED shape of

$$\frac{F(\lambda_{\rm IP})}{F_0(\lambda_{\rm IP})} = \frac{(\mathrm{EW} - a_0)/a_1}{F_0(1367)}. \tag{20}$$

Following this methodology, we derive relative ionizing continuum light curves for each absorption line representative of the time-varying relative fluxes at their ionization potentials. Figure 27 shows these relative light curves for the blue components of the Si IV, C IV, and N V doublets of the intrinsic absorption line for component 1 in NGC 5548. The figure also compares these relative light curves to the deficiency in the broad C IV emission-line flux during the BLR holiday (Goad et al. 2016), defined as the percentage diminution in the C IV emission-line flux during the holiday compared to the expected flux based on the correlation of C IV emission-line flux with the continuum flux observed during the first 75 days of the AGN STORM campaign. Note that the relative decrease in broad C IV emission-line flux occurs during the same time interval

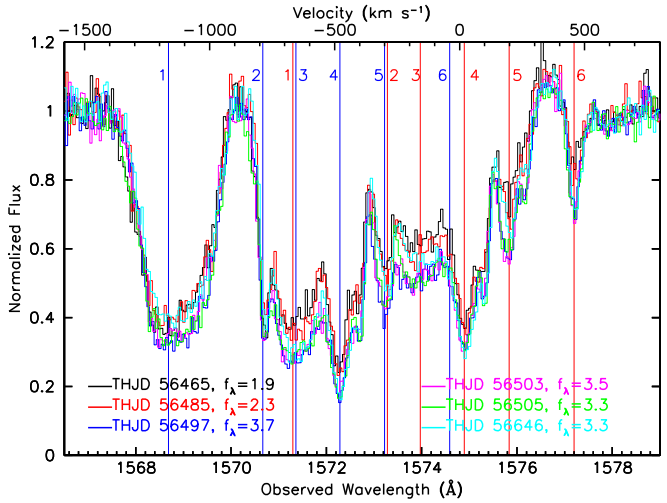

Figure 25. Illustration of variability in the narrow absorption components of C IV in NGC 5548 during the *XMM-Newton* campaign (Kaastra et al. 2014). Normalized relative fluxes are plotted as a function of velocity relative to the systemic redshift of $z = 0.017175$ for C IV λ1548. The colored curves are the spectra for the observation dates given in the key, along with the observed flux at 1367 Å in units of 10^{-14} erg cm^{-2} s^{-1} Å^{-1}. Vertical blue lines indicate the velocities of the blue components of the doublets for the six intrinsic absorbers. Vertical red lines show the locations of the corresponding red components. Component 1 shows little variability during the campaign, indicating high saturation.

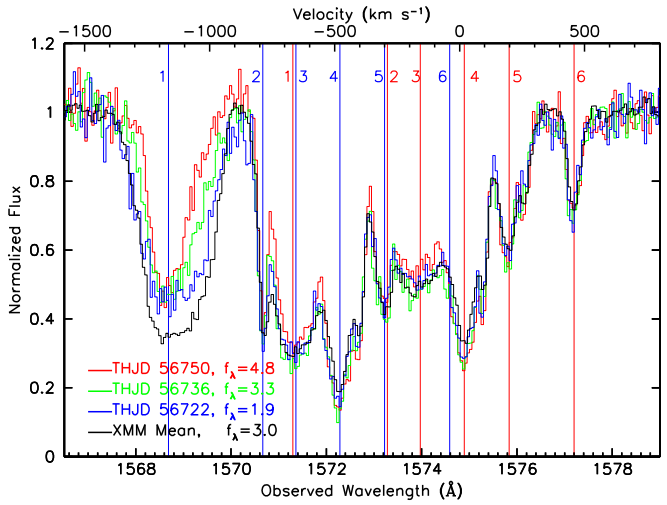

Figure 26. Illustration of variability in the narrow absorption components of C IV in NGC 5548 during the early part of the AGN STORM campaign, when the strength of C IV absorption in component 1 was highly correlated with the FUV continuum flux. Normalized relative fluxes are plotted as a function of velocity relative to the systemic redshift of $z = 0.017175$ for C IV λ1548. The colored curves are the spectra for the observation dates given in the key along with the observed flux at 1367 Å in units of 10^{-14} erg cm^{-2} s^{-1} Å^{-1}. The illustrated spectra show high (red), low (blue), and mean (green) flux levels in comparison to the mean spectrum from the *XMM-Newton* campaign (black). Vertical blue lines indicate the velocities of the blue components of the doublets for the six intrinsic absorbers. Vertical red lines show the locations of the corresponding red components. During AGN STORM, the absorption profile in component 1 varies as expected for gas showing an ionization response.

(56,776 < THJD < 56,827) as the inferred decrease in EUV continuum flux at the ionization potentials of Si IV (45.1 eV), C IV (64.5 eV), and N V (97.9 eV) deduced from the behavior of the intrinsic absorption line. All three inferred continua show

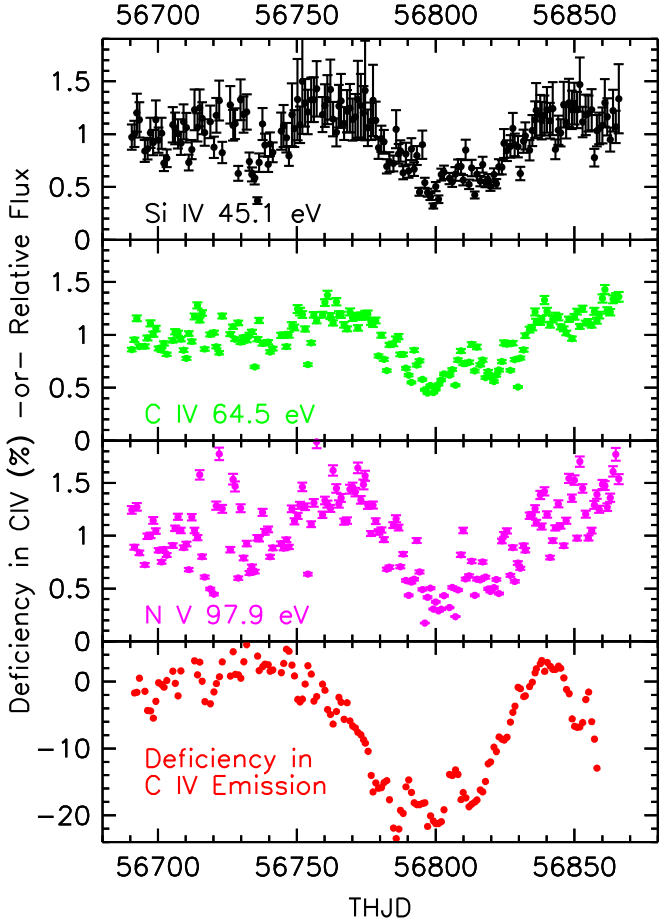

Figure 27. Relative EUV continuum fluxes at the ionization potentials of Si IV (45.1 eV; black points), C IV (64.5 eV; green points), and N V (97.9 eV; magenta points) as deduced from variations in the EW of the absorption lines Si IV λ1393, C IV λ1548, and N V λ1238 associated with the intrinsic narrow absorption component 1 in NGC 5548. Red points show the percentage deficiency in the flux of C IV broad emission during the BLR holiday (Goad et al. 2016).

significant correlations with the deficit in the C IV emission. However, there is a delay between the C IV deficit and the inferred continua. Using ICCF, we find delays and peak correlation coefficients of 11.6 ± 1 days and $r = 0.66$ for Si IV, 10.5 ± 1 days and $r = 0.70$ for C IV, and 12.3 ± 1 days and $r = 0.64$ for N V. These delays are actually with respect to the FUV continuum at 1158 Å, since Goad et al. (2016) shifted the C IV light curve by −5 days to align it with the continuum variations, so the inferred EUV continua variations are delayed by 5–7 days relative to the C IV deficit. These delays are puzzling, since one might expect the C IV deficit to lag the continuum deficits rather than vice versa if they were the direct cause of the BLR holiday. Dehghanian et al. (2019) investigated the complex responses of the intrinsic narrow absorption lines to changes in the ionizing continuum and the intervening obscurer in greater detail, although they also did not explain this puzzling behavior.

4.4. Variability of the Broad Absorption Features

As discussed in Section 5.2, the broad absorption features that appear as extensive blueshifted troughs on all of the

resonant UV lines in the spectrum of NGC 5548 are the UV counterparts to the soft X-ray obscurer discovered by Kaastra et al. (2014). These broad UV absorption features also vary with time. In fact, in the observations from that campaign, there was a significant anticorrelation between the strength of the absorption troughs and the soft X-ray flux as measured by *Swift* (linear correlation coefficient $r = -0.37$). As the soft X-ray intensity increased, the broad UV absorption strength decreased. This is not due to a photoionization response, however. The broad UV absorption lines are saturated, so their strength is also governed more by the covering factor than by the ionization state or column density of the absorbing gas.

The more extensive monitoring of the time variability of the broad absorption features enabled by the STORM campaign reveals an even more complex picture. As shown in Figure 28, the anticorrelation of the EW of the broad absorption is not as clean as it was in the six points available from the *XMM-Newton* campaign.

While there is a rough anticorrelation ($r = -0.41$) early in the campaign (THJD $< 56{,}766$), as with the behavior of the narrow absorption lines, the correlation disappears after THJD $= 56{,}766$ ($r = +0.02$), approximately the time of the onset of the BLR holiday (Goad et al. 2016). Figure 29 shows this even more dramatically. Light curves for the EWs of the broad absorption features are eerily similar to the time variation of the anomalous deficit in the response of the flux of the broad emission lines. The connection between these two behaviors is puzzling. On the one hand, the lack of response in the BLR during the holiday appears to be due to a change in the SED, in which the soft X-ray excess decouples from the visible UV continuum. A decrease in the BLR flux during the holiday implies a decrease in the ionizing UV driving the line emission. On the other hand, a decrease in the broad absorption-line EW implies a decrease in the covering factor of the obscurer, because these broad troughs appear to be saturated (Section 4.2), and we see no dramatic changes in their velocity widths. This is also seen in the *Swift* monitoring of NGC 5548 (Mehdipour et al. 2016b), and it implies that more of the EUV and soft X-ray flux is being transmitted past the obscurer. Plus, since the BLR response represents a global view of the continuum source, and our view of the obscurer is restricted purely to our line of sight, this suggests that our view of the obscurer may not be a special geometrical arrangement, such as a single cloud crossing our line of sight, but rather a more axisymmetric arrangement affecting all sight lines that illuminate the BLR. Dehghanian et al. (2019) presented further photoionization analysis of both the narrow and the broad absorbers that support this interpretation.

An approximate axisymmetric arrangement for the obscurer is even more natural when one considers the timescales covered by our observations. From the beginning of the *XMM-Newton* campaign in 2013 June to the end of the reverberation mapping campaign in 2014 July, the elapsed time was 415 days. For a black hole mass of $5.2 \times 10^7\ M_\odot$ (Bentz & Katz 2015), clouds at a radius of 1 lt-day at the innermost edge of the BLR would have an orbital timescale of 115 days. Thus, the obscurer and the innermost part of the BLR could have completed more than one full revolution over the course of our observing programs.

5. Discussion

Modeling the UV spectra of NGC 5548 from the STORM campaign accomplished our primary goal of obtaining clean,

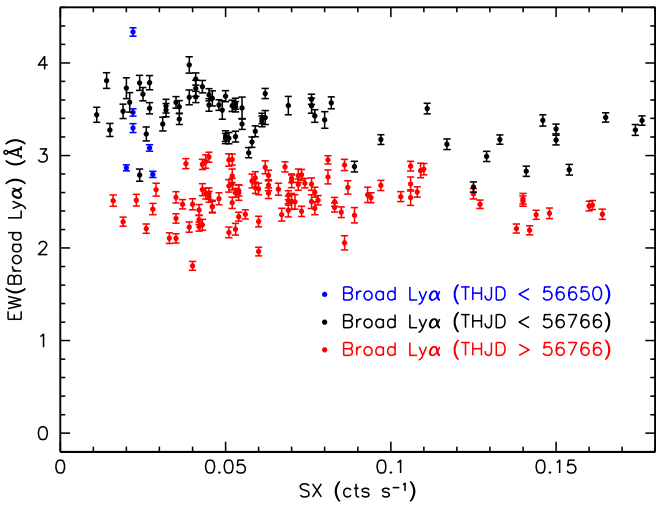

Figure 28. Correlation of the absolute value of the EW of the broad absorption in Lyα in NGC 5548 with the soft X-ray flux from *Swift*. Blue points are for the six observations of the *XMM-Newton* campaign, all prior to THJD = 56,650; black points are for dates in the STORM campaign earlier than THJD = 56,766; and red points are for later times.

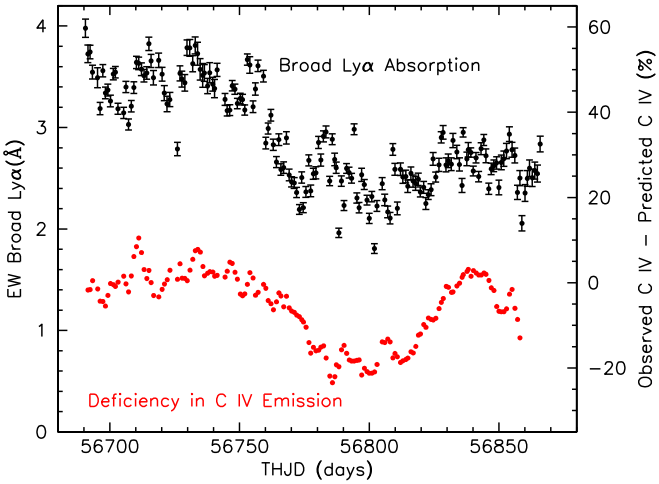

Figure 29. Light curve of the variations in the absolute value of the EW of broad Lyα absorption in NGC 5548 (black points) compared to the percentage deficiency in the flux of C IV broad emission (red points) during the BLR holiday (Goad et al. 2016).

absorption-corrected, deblended emission-line profiles of all of the principal UV emission lines. We are also able to separate the nonvarying contributions of the narrow- and intermediate-line emission to the Lyα and C IV profiles and produce uniform velocity-binned lag measurements across the full profiles of Lyα and C IV. These "clean" line profiles are a key element for future detailed modeling of the BLR to produce two-dimensional velocity-delay maps using both MEMEcho (K. Horne et al. 2019, in preparation) and forward-modeling techniques (A. Pancoast et al. 2019, in preparation). However, simple characteristics of the emission-line profiles and one-dimensional velocity-delay profiles enable us to make some key inferences.

The Lyα velocity-delay profile shows a distinctive "M" shape, with short lags at high velocity, peak lags of ~6–8 days at moderate velocities ($\pm 2500\ \mathrm{km\ s^{-1}}$), and a local minimum near zero velocity. As we will discuss in more detail later, this

is very different from the centrally peaked Hβ profile observed in 2007 by Denney et al. (2009). The C IV velocity-delay profile is similar to Lyα, but it shows only "shoulders" rather than a central dip. This behavior was seen in the original raw data (De Rosa et al. 2015), but we now have a clean, uniform picture across both profiles. This morphology is very similar to that seen in Hβ during the ground-based portion of the STORM campaign (Pei et al. 2017), as well as during the 2015 campaign by Lu et al. (2016) and Xiao et al. (2018).

The short lags at high velocity and longer lags at low velocity are a natural expectation for Keplerian profiles in a disk (Welsh & Horne 1991; Horne et al. 2004). In a simple disk geometry, where the line-emitting portion of the disk is truncated at both an inner and an outer radius, the lag profile across the emission line extends from short lags at high velocities, corresponding to the inner radius of the disk, and rises to peaks at lower velocities, corresponding to the outer radius of the disk (Welsh & Horne 1991). In the region near zero velocity, the near-zero lags from the near side of the disk produce a central dip. The sharp peaks of the lag profile produced by a thin disk in the models of Welsh & Horne (1991) are a direct consequence of their disk model having a monotonic power-law emissivity and sharp edges. This leads to a "cuspy" shape for the transfer function, $\Psi(\tau)$. The sharp peaks can be broadened into smoother bumps if the line-emitting portions of the disk do not have abrupt edges and the disk is thickened, as in Pancoast et al. (2014), for example. In the case of NGC 5548, the transfer function $\Psi(\tau)$ recovered from the data is smooth and bell-shaped (K. Horne et al. 2019, in preparation), which would result in smooth, round peaks in the lag profile.

Notably, the lag profile for C IV for the full campaign shows an upturn to longer lags at high positive velocities ($>$10,000 km s^{-1}). This feature was not evident in the original raw data but may now appear when the contamination of the red wing of C IV by the shorter lag of He II may have been biasing the result to lower values. Longer lags at high positive velocities are indicative of outflowing gas, since redshifted outflowing gas is on the far side of the illuminating source relative to the observer. See the models of Welsh & Horne (1991) for examples. These long lags at high positive velocities are absent when we restrict the data to the first 75 days of the campaign before the BLR holiday.

The C IV lag profile shows additional changes in structure for different time intervals during the campaign, as discussed in Section 4.1. The biggest change is the apparent change from a local minimum in the lag on the red side of the red emission bump in the preholiday period to a local maximum on the blue side of the bump during the holiday period. These changes are in contrast to smoother, more uniform changes for Lyα, which mostly track the evolution to longer lags of the mean profile at all velocities across the profile. Although we cannot unambiguously assign physical explanations to one-dimensional emission-line and lag profiles, the difference in behavior between C IV and Lyα may reflect the differences in radiative transfer through the BLR for these two emission lines. Both lines are generally considered to be optically thick, with preferential emission originating from the illuminated side of the BLR gas (Kwan & Krolik 1979, 1981; Ferland et al. 1992), but the smoother evolution of the lag profile during the course of the campaign may suggest that Lyα emission is less orientation-dependent than that of C IV.

The lag profiles across the emission lines in NGC 5548 have also evolved on longer timescales over the past decade. In the 2007 observations of the Hβ profile by Denney et al. (2009), the lag profile is centrally peaked with no dip, and it extends to velocities of only $\pm$6000 km s^{-1}. For a black hole mass of $M_{\rm BH} = 5.2 \times 10^7\ M_\odot$ (Bentz & Katz 2015) and an inclination of $i = 32°$ (Pancoast et al. 2014), this corresponds to Keplerian velocities at an inner disk radius of 2.3 lt-day. The innermost bins span a range of $\pm$1000 km s^{-1}/sin i, which correspond to Keplerian velocities at an outer disk radius of $\sim$80 lt-day.

The AGN12 campaign (De Rosa et al. 2018) showed that by 2012, NGC 5548 had developed a double-peaked, "M"-shaped lag profile. By the time of the STORM campaign in 2014, this shape was well developed in both Hβ and Lyα. For the STORM data, profiles reaching velocities of $\pm$10,000 km s^{-1} imply an inner disk radius of $\sim$0.8 lt-day. The double peaks at $\pm$2500 km s^{-1} lead to an outer disk radius of 13 lt-day.

These changes in the implied overall structure of the BLR may explain the departure of its measured size from the previously well-established BLR size/luminosity relation (see Figure 13 of Pei et al. 2017) as the luminosity of NGC 5548 has evolved in time over the past two decades. Figure 30 compares the evolution in the optical luminosity (λL_{5100}) of NGC 5548 to the size of the BLR as measured by the reverberation lag of the Hβ emission line. During the 2007 campaign of Denney et al. (2009), NGC 5548 was near a minimum in its luminosity. The integrated Hβ lag was 5 days, and it fit well on the BLR size/luminosity relation. In 2012, NGC 5548 increased to normal brightness levels, but the overall Hβ lag remained low at 4 days (De Rosa et al. 2018). One must be careful in assessing the absolute values of these changes in size, however. Goad & Korista (2014) noted that emission-line lags can be biased low by factors of 2–3 for short continuum variability timescales (as we observed in the STORM campaign) and campaigns of short duration (as were those in the 2000s). During the lengthy STORM campaign in 2014, NGC 5548 remained bright, yet the Hβ lag remained small, at 4 days, factors of 5–6 smaller than historical values in the 1990s. Notably, these changes coincide with the appearance of the X-ray obscurer in 2012 February, as shown in data from *Swift* monitoring (Mehdipour et al. 2016b).

Similar behavior has been seen in NGC 3783. This Seyfert 1 also exhibited an obscuration event in 2016 with heavy soft X-ray and broad UV absorption (Mehdipour et al. 2017). When the obscuration appeared, NGC 3783 was at a luminosity peak following a low-luminosity state from 2011 through 2014 (Kaastra et al. 2018). Despite the high luminosity, its broad lines were significantly diminished in flux, with moderate velocity regions ($\sim$2800 km s^{-1}) of the profile apparently gone (Kriss et al. 2019). Kriss et al. (2019) suggested that the changes in the structure of the BLR and the appearance of the obscuring outflow are related. In the context of disk-driven wind models (Murray & Chiang 1997; Proga et al. 2000; Proga & Kallman 2004; Proga & Waters 2015; Waters & Proga 2016; Czerny et al. 2017; Baskin & Laor 2018), the transition from a normal BLR configuration to an extended low state requires several years for the BLR to dynamically adjust to the reduced radiation pressure from the accretion disk. The BLR at large radii collapses back toward the disk plane, and the peak in the BLR emissivity shifts to smaller radii. When the continuum brightens, the excess material in the inner regions may be blown away as a radiatively driven wind, observable as the

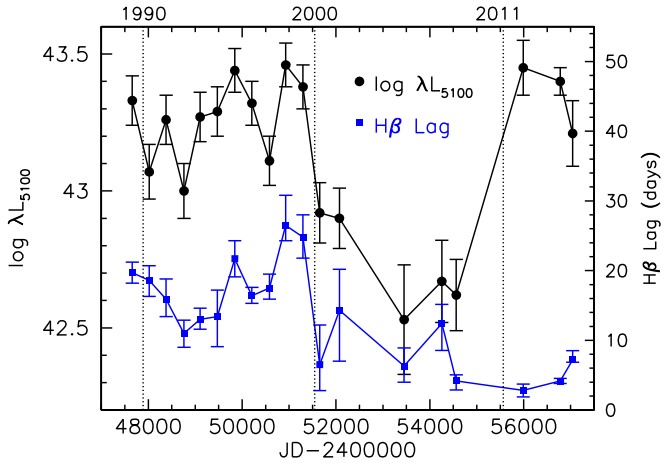

Figure 30. Time series showing the history of the optical luminosity of NGC 5548 (λL_{5100}; black points) and the reverberation lag size for the Hβ emission line (blue points). Vertical dotted lines show the dates 1990 January 1, 2000 January 1, and 2011 January 1. Data prior to 2011 are from Kilerci Eser et al. (2015), which are taken from these original sources: Peterson (1993) and Peterson et al. (2002), Bentz et al. (2007, 2009), Denney et al. (2009). Data in 2012 are from De Rosa et al. (2018). Data in 2014 are from the STORM campaign (Pei et al. 2017). Data in 2015 are from Lu et al. (2016).

obscurer. The BLR reinflates, but this requires years, governed by the freefall timescale for the disk wind, which is 3.4 yr at 10 lt-day in NGC 3783 for a black hole mass of $M_{\rm BH} = 2.3 \times 10^7\ M_\odot$ (Bentz & Katz 2015).

Timescales in NGC 5548 are similar but shorter, given its slightly higher black hole mass. At 10 lt-day in NGC 5548, Keplerian velocities are ~5200 km s^{-1}, and the freefall time, defined as

$$t_{\rm ff} = \left(\frac{2R^3}{GM_{\rm BH}}\right)^{1/2}, \qquad (21)$$

is 2.3 yr. The shrunken size of the BLR during the STORM campaign is also reflected in the lack of stratification in the ionization structure that was evident in past campaigns (Clavel et al. 1991; Korista et al. 1995). Except for He II, all other broad emission lines have indistinguishable lags. After the STORM campaign, in 2015, NGC 5548 appears to be reverting back to the normal size/luminosity relation. Lu et al. (2016) observed an increase in the Hβ lag to 7 days. They suggested that this evolution in size was evidence of radiation pressure affecting the size of the BLR, with a time delay likely due to the dynamical timescale of the BLR, similar to our arguments above.

Although our modeling of the UV spectra from the NGC 5548 STORM campaign has enabled us to better understand the dynamics of the BLR and its potential links to the appearance of X-ray and UV obscuration, we must still work out the details of what produces the short timescale variations in the obscuring gas and how that affects the BLR emission. These processes will be subjects of future papers.

6. Summary

We have modeled the *HST* UV spectra of NGC 5548 obtained during the 2014 STORM campaign. The model uses 97 emission and absorption components to construct an emission model for all 171 spectra of NGC 5548 obtained during the campaign. The model permits us to separate the broad absorption associated with the soft X-ray obscuration discovered by Kaastra et al. (2014) and correct for narrow absorption produced by the intrinsic UV absorption lines of NGC 5548, as well as intervening interstellar features. Using the model, we are able to produce absorption-corrected, deblended emission-line profiles; velocity-binned light curves for Lyα and C IV; and light curves for all narrow and broad absorption components. The modeled emission-line profiles eliminate the nonvarying flux of the narrow- and intermediate-line components of Lyα and C IV, separate the contributions of N V and He II into their profiles, and give a clear view of the emission-line time delay across the full line profile. The principal results of our study are as follows.

1. The time lags of 2–8 days for the integrated emission lines are comparable to or slightly shorter than those in De Rosa et al. (2015), primarily due to the elimination of the nonvarying narrow- and intermediate-line components (Section 4.1).
2. The velocity-binned lag profiles have a distinct "M" shape in Lyα and less prominent local maxima above a central minimum in C IV (Section 4.1). The local minima in the lag profiles are near zero velocity, and the local peaks (Lyα) or shoulders (C IV) are at $\pm$2500 km s^{-1} (Section 4.1). This morphology is indicative of Keplerian motion in a disklike configuration.
3. The narrow absorption lines vary in strength in response to changes in the continuum intensity (Section 4.3). The lowest-ionization absorption lines (Lyα, C II, and Si II) correlate with the continuum through the course of the whole campaign. Their variations show a delayed and smoothed response to continuum variations consistent with recombination of gas with densities of log $n_{\rm e}$ cm^{-3} ~ 5, similar to the density measured by Arav et al. (2015) using density-sensitive absorption lines of C III* and Si III* and similar to the density of the NLR inferred by Kraemer et al. (1998) and Peterson et al. (2013).
4. High-ionization intrinsic narrow absorption lines (Si IV, C IV, and N V) correlate well with the continuum during the first 75 days of the campaign (Section 4.3). Thereafter, they decorrelate, showing signs of the same "holiday" exhibited by the BLR (Goad et al. 2016). During the holiday period, their strengths correlate most closely with the soft X-ray flux as measured by *Swift*, which suggests that the soft X-ray flux is more closely related to the ionizing EUV than the FUV continuum. Using the response of these high-ionization absorption lines, we are able to reconstruct the relative flux of the SED in the EUV. We show that it is diminished in flux relative to the FUV continuum during the period of the holiday.
5. The broad absorption lines associated with the X-ray obscurer also vary during the course of the campaign (Section 4.4). Early in the campaign, they show a rough anticorrelation with the soft X-ray flux, as seen by Kaastra et al. (2014). However, during the holiday period, they decrease in strength, with behavior mimicking the deficiencies in the flux of the broad emission lines. This behavior is not understood.
6. The departure of NGC 5548's BLR from the radius/luminosity relationship of Peterson et al. (2002) during

the AGN12 campaign in 2012 (De Rosa et al. 2018) coincides with the appearance of the X-ray obscurer at about the same time (Mehdipour et al. 2016b). We suggest that the two events are related, and that the obscurer is a manifestation of a disk wind launched by the brightening of NGC 5548 in 2012 after a prolonged low-luminosity state that had led to the collapse of the BLR (Section 5).

Modeling the UV spectra of NGC 5548 from the STORM campaign has yielded crucial insights into the behavior of the emission- and absorption-line gas, as well as properties of the ionizing continuum that were not easily seen in the raw data. These new insights may help us to resolve the structure of the BLR and successfully interpret our measures of its two-dimensional reverberation maps.

We thank R. Plesha for formatting and posting the high-level data products in MAST. Support for *HST* program No. GO-13330 was provided by NASA through a grant from the Space Telescope Science Institute, which is operated by the Association of Universities for Research in Astronomy, Inc., under NASA contract NAS5-26555. M.M.F., G.D.R., B.M.P., C.J.G., and R.W.P. are grateful for the support of the National Science Foundation (NSF) through grant AST-1008882 to The Ohio State University. A.J.B. and L.P. have been supported by NSF grant AST-1412693. E.M.C., E.D.B., L.M., and A.P. acknowledge support from Padua University through grants DOR1699945/16, DOR1715817/17, DOR1885254/18, and BIRD164402/16. M.C.B. gratefully acknowledges support through NSF CAREER grant AST-1253702 to Georgia State University. S.B. was supported by NASA through Chandra award No. AR7-18013X issued by the *Chandra X-ray Observatory* Center, operated by the Smithsonian Astrophysical Observatory for NASA under contract NAS8-03060. S.B. was also partially supported by grant HST-AR-13240.009. M. C.B. acknowledges HHMI for support through an undergraduate science education grant to Southwestern University. K.D.D. is supported by an NSF Fellowship awarded under grant AST-1302093. R.E. gratefully acknowledges support from NASA under awards NNX13AC26G, NNX13AC63G, and NNX13AE99G and ADAP award 80NSSC17K0126. G.J. F. and M.D. thank the NSF (1816537), NASA (ATP 17-0141), and STScI (HST-AR-13914, HST-AR-15018) for their support and the Huffaker scholarship for funding related travel. B.D.M. acknowledges support from Polish National Science Center grant Polonez 2016/21/P/ST9/04025. J.M.G. gratefully acknowledges support from NASA under award NNH13CH61C. P.B.H. is supported by NSERC. K.H. acknowledges support from the UK Science and Technology Facilities Council through grant ST/J001651/1. M.I. acknowledges support from National Research Foundation of Korea (NRF) grant No. 2017R1A3A3001362. M.K. was supported by the National Research Foundation of Korea (NRF) grant funded by the Korean government (MSIT) (No. 2017R1C1B2002879). M.D.J. acknowledges NSF grant AST-0618209. SRON is financially supported by NWO, the Netherlands Organization for Scientific Research. B.C.K. is partially supported by the UC Center for Galaxy Evolution. C. S.K. acknowledges the support of NSF grants AST-1814440 and AST-1515876. D.C.L. acknowledges support from NSF grants AST-1009571 and AST-1210311. P.L. acknowledges support from Fondecyt grant No. 1120328. A.P. acknowledges support from an NSF graduate fellowship and a UCSB Dean's Fellowship. C.S. acknowledges support from NOVA, the Nederlandse Onderzoekschool voor Astronomie. J.S.S. acknowledges CNPq, the National Council for Scientific and Technological Development (Brazil), for partial support and The Ohio State University for warm hospitality. T.T. has been supported by NSF grant AST-1412315. T.T. and B.C.K. acknowledge support from the Packard Foundation in the form of a Packard Research Fellowship to T.T. Support for A.V.F.'s group at UC Berkeley is provided by the TABASGO Foundation, the Christopher R. Redlich Fund, and the Miller Institute for Basic Research in Science (UC Berkeley). M.V. and J.J.J. gratefully acknowledge support from the Danish Council for Independent Research via grant No. DFF 4002-00275. J.-H.W. acknowledges support by the National Research Foundation of Korea (NRF) grant funded by the Korean government (No. 2010-0027910). This research has made use of the NASA/IPAC Extragalactic Database (NED), which is operated by the Jet Propulsion Laboratory, California Institute of Technology, under contract with the National Aeronautics and Space Administration.

ORCID iDs

G. A. Kriss https://orcid.org/0000-0002-2180-8266
G. De Rosa https://orcid.org/0000-0003-3242-7052
J. Ely https://orcid.org/0000-0002-4814-5511
B. M. Peterson https://orcid.org/0000-0001-6481-5397
G. J. Ferland https://orcid.org/0000-0003-4503-6333
M. Dehghanian https://orcid.org/0000-0002-0964-7500
R. Edelson https://orcid.org/0000-0001-8598-1482
K. T. Korista https://orcid.org/0000-0003-0944-1008
A. J. Barth https://orcid.org/0000-0002-3026-0562
M. C. Bentz https://orcid.org/0000-0002-2816-5398
W. N. Brandt https://orcid.org/0000-0002-0167-2453
D. M. Crenshaw https://orcid.org/0000-0002-6465-3639
M. Eracleous https://orcid.org/0000-0002-3719-940X
M. M. Fausnaugh https://orcid.org/0000-0002-9113-7162
M. R. Goad https://orcid.org/0000-0002-2908-7360
C. J. Grier https://orcid.org/0000-0001-9920-6057
Keith Horne https://orcid.org/0000-0003-1728-0304
C. S. Kochanek https://orcid.org/0000-0001-6017-2961
H. Netzer https://orcid.org/0000-0002-6766-0260
A. Pancoast https://orcid.org/0000-0003-1065-5046
R. W. Pogge https://orcid.org/0000-0003-1435-3053
D. Proga https://orcid.org/0000-0002-6336-5125
M. Vestergaard https://orcid.org/0000-0001-9191-9837
T G. Beatty https://orcid.org/0000-0002-9539-4203
V. N. Bennert https://orcid.org/0000-0003-2064-0518
S. Bisogni https://orcid.org/0000-0003-3746-4565
R. Boissay-Malaquin https://orcid.org/0000-0003-2704-599X
A. A. Breeveld https://orcid.org/0000-0002-0001-7270
E. M. Cackett https://orcid.org/0000-0002-8294-9281
C. T. Coker https://orcid.org/0000-0002-9954-7887
E. Costantini https://orcid.org/0000-0001-8470-749X
S. Croft https://orcid.org/0000-0003-4823-129X
K. V. Croxall https://orcid.org/0000-0002-5258-7224
A. J. Deason https://orcid.org/0000-0001-6146-2645
A. V. Filippenko https://orcid.org/0000-0003-3460-0103
D. Grupe https://orcid.org/0000-0002-9961-3661
P. B. Hall https://orcid.org/0000-0002-1763-5825
C. B. Henderson https://orcid.org/0000-0001-8877-9060

E. Holmbeck https://orcid.org/0000-0002-5463-6800
T. W.-S. Holoien https://orcid.org/0000-0001-9206-3460
T. A. Hutchison https://orcid.org/0000-0001-6251-4988
M. Im https://orcid.org/0000-0002-8537-6714
P. L. Kelly https://orcid.org/0000-0003-3142-997X
J. A. Kennea https://orcid.org/0000-0002-6745-4790
Zhiyuan Ma https://orcid.org/0000-0003-3270-6844
M. A. Malkan https://orcid.org/0000-0001-6919-1237
G. Matt https://orcid.org/0000-0002-2152-0916
J. C. Mauerhan https://orcid.org/0000-0002-7555-8741
H.-W. Rix https://orcid.org/0000-0003-4996-9069
B. J. Shappee https://orcid.org/0000-0003-4631-1149
J. Tayar https://orcid.org/0000-0002-4818-7885
D. J. Walton https://orcid.org/0000-0001-5819-3552

References

Arav, N., Chamberlain, C., Kriss, G. A., et al. 2015, A&A, 577, A37
Arav, N., Korista, K. T., & de Kool, M. 2002, ApJ, 566, 699
Baskin, A., & Laor, A. 2018, MNRAS, 474, 1970
Bentz, M. C., Denney, K. D., Cackett, E. M., et al. 2007, ApJ, 662, 205
Bentz, M. C., & Katz, S. 2015, PASP, 127, 67
Bentz, M. C., Walsh, J. L., Barth, A. J., et al. 2009, ApJ, 705, 199
Bentz, M. C., Walsh, J. L., Barth, A. J., et al. 2010, ApJ, 716, 993
Bevington, P. R. 1969, Data Reduction and Error Analysis for the Physical Sciences (New York: McGraw-Hill)
Blandford, R. D., & McKee, C. F. 1982, ApJ, 255, 419
Cappi, M., De Marco, B., Ponti, G., et al. 2016, A&A, 592, A27
Cardelli, J. A., Clayton, G. C., & Mathis, J. S. 1989, ApJ, 345, 245
Clavel, J., Reichert, G. A., Alloin, D., et al. 1991, ApJ, 366, 64
Crenshaw, D. M., Kraemer, S. B., & George, I. M. 2003, ARA&A, 41, 117
Crenshaw, D. M., Kraemer, S. B., Schmitt, H. R., et al. 2009, ApJ, 698, 281
Czerny, B., Li, Y.-R., Hryniewicz, K., et al. 2017, ApJ, 846, 154
Dehghanian, M., Ferland, G. J., Kriss, G. A., et al. 2019, ApJ, 877, 119
Denney, K. D., Peterson, B. M., Pogge, R. W., et al. 2009, ApJL, 704, L80
De Rosa, G., Fausnaugh, M. M., Grier, C. J., et al. 2018, ApJ, 866, 133
De Rosa, G., Peterson, B. M., Ely, J., et al. 2015, ApJ, 806, 128
de Vaucouleurs, G., de Vaucouleurs, A., Corwin, H. G. J., et al. 1991, Third Reference Catalogue of Bright Galaxies (New York: Springer)
Di Gesu, L., Costantini, E., Ebrero, J., et al. 2015, A&A, 579, A42
Ebrero, J., Kaastra, J. S., Kriss, G. A., et al. 2016, A&A, 587, A129
Edelson, R., Gelbord, J. M., Horne, K., et al. 2015, ApJ, 806, 129
Fausnaugh, M. M., Denney, K. D., Barth, A. J., et al. 2016, ApJ, 821, 56
Ferland, G. J., Chatzikos, M., Guzmán, F., et al. 2017, RMxAA, 53, 385
Ferland, G. J., Peterson, B. M., Horne, K., Welsh, W. F., & Nahar, S. N. 1992, ApJ, 387, 95
Goad, M., & Korista, K. 2014, MNRAS, 444, 43
Goad, M. R., Korista, K. T., De Rosa, G., et al. 2016, ApJ, 824, 11
Gravity Collaboration, Sturm, E., Dexter, J., et al. 2018, Natur, 563, 657
Green, J. C., Froning, C. S., Osterman, S., et al. 2012, ApJ, 744, 60
Grier, C. J., Peterson, B. M., Horne, K., et al. 2013, ApJ, 764, 47
Hopkins, P. F., Strauss, M. A., Hall, P. B., et al. 2004, AJ, 128, 1112
Horne, K., Peterson, B. M., Collier, S. J., & Netzer, H. 2004, PASP, 116, 465
Kaastra, J. S., Kriss, G. A., Cappi, M., et al. 2014, Sci, 345, 64
Kaastra, J. S., Mehdipour, M., Behar, E., et al. 2018, A&A, 619, A112
Kaastra, J. S., Steenbrugge, K. C., Raassen, A. J. J., et al. 2002, A&A, 386, 427
Kilerci Eser, E., Vestergaard, M., Peterson, B. M., Denney, K. D., & Bentz, M. C. 2015, ApJ, 801, 8
Korista, K. T., Alloin, D., Barr, P., et al. 1995, ApJS, 97, 285
Kraemer, S. B., Crenshaw, D. M., Filippenko, A. V., & Peterson, B. M. 1998, ApJ, 499, 719
Kriss, G. A., Mehdipour, M., Kaastra, J. S., et al. 2019, A&A, 621, A12
Krolik, J. H., Horne, K., Kallman, T. R., et al. 1991, ApJ, 371, 541
Krolik, J. H., & Kriss, G. A. 1995, ApJ, 447, 512
Krongold, Y., Binette, L., & Hernández-Ibarra, F. 2010, ApJL, 724, L203
Krongold, Y., Nicastro, F., Elvis, M., et al. 2007, ApJ, 659, 1022
Kwan, J., & Krolik, J. H. 1979, ApJL, 233, L91
Kwan, J., & Krolik, J. H. 1981, ApJ, 250, 478
Longinotti, A. L., Kriss, G., Krongold, Y., et al. 2019, ApJ, 875, 150
Lu, K.-X., Du, P., Hu, C., et al. 2016, ApJ, 827, 118
Marshall, H. L., Carone, T. E., Peterson, B. M., et al. 1997, ApJ, 479, 222
Mathur, S., Elvis, M., & Wilkes, B. 1995, ApJ, 452, 230
Mathur, S., Elvis, M., & Wilkes, B. 1999, ApJ, 519, 605
Mathur, S., Gupta, A., Page, K., et al. 2017, ApJ, 846, 55
Mehdipour, M., Kaastra, J. S., & Kallman, T. 2016a, A&A, 596, A65
Mehdipour, M., Kaastra, J. S., Kriss, G. A., et al. 2015, A&A, 575, A22
Mehdipour, M., Kaastra, J. S., Kriss, G. A., et al. 2016b, A&A, 588, A139
Mehdipour, M., Kaastra, J. S., Kriss, G. A., et al. 2017, A&A, 607, A28
Murray, N., & Chiang, J. 1997, ApJ, 474, 91
Murty, K. G. 1983, Linear Programming (New York: Wiley)
Pancoast, A., Brewer, B. J., Treu, T., et al. 2014, MNRAS, 445, 3073
Pei, L., Fausnaugh, M. M., Barth, A. J., et al. 2017, ApJ, 837, 131
Peterson, B. M. 1993, PASP, 105, 247
Peterson, B. M., Berlind, P., Bertram, R., et al. 2002, ApJ, 581, 197
Peterson, B. M., Denney, K. D., De Rosa, G., et al. 2013, ApJ, 779, 109
Peterson, B. M., Ferrarese, L., Gilbert, K. M., et al. 2004, ApJ, 613, 682
Peterson, B. M., & Wandel, A. 1999, ApJL, 521, L95
Proga, D., & Kallman, T. R. 2004, ApJ, 616, 688
Proga, D., Stone, J. M., & Kallman, T. R. 2000, ApJ, 543, 686
Proga, D., & Waters, T. 2015, ApJ, 804, 137
Savage, B. D., & Sembach, K. R. 1991, ApJ, 379, 245
Schlafly, E. F., & Finkbeiner, D. P. 2011, ApJ, 737, 103
Schlegel, D. J., Finkbeiner, D. P., & Davis, M. 1998, ApJ, 500, 525
Starkey, D., Horne, K., Fausnaugh, M. M., et al. 2017, ApJ, 835, 65
Steenbrugge, K. C., Kaastra, J. S., Crenshaw, D. M., et al. 2005, A&A, 434, 569
Vestergaard, M., & Peterson, B. M. 2005, ApJ, 625, 688
Wakker, B. P., Lockman, F. J., & Brown, J. M. 2011, ApJ, 728, 159
Waters, T., & Proga, D. 2016, MNRAS, 460, L79
Welsh, W. F., & Horne, K. 1991, ApJ, 379, 586
Wills, B. J., Netzer, H., & Wills, D. 1985, ApJ, 288, 94
Xiao, M., Du, P., Lu, K.-K., et al. 2018, ApJL, 865, L8